Nonlinearity and Gating in Superconducting Nanowire Single Photon Detectors

by

Mohsen Keshavarz Akhlaghi

A thesis
presented to the University of Waterloo
in fulfillment of the
thesis requirement for the degree of
Doctor of Philosophy
in
Electrical and Computer Engineering

Waterloo, Ontario, Canada, 2011

I hereby declare that I am the sole author of this thesis. This is a true copy of the thesis, including any required final revisions, as accepted by my examiners.

Mohsen K. Akhlaghi

I understand that my thesis may be made electronically available to the public.

Mohsen K. Akhlaghi

Abstract

The quantum properties of electromagnetic radiation at single photon level promise to offer what are classically inaccessible. Single photon sources and detectors are therefore on demand for exploiting these properties in practical applications, including but not limited to quantum information processing and communication. In this thesis, I advance Superconducting Nanowire Single Photon Detectors (SNSPD) both in terms of models describing their operation, and their performance. I report on characterization, semi-empirical modeling, quantum-optical modeling and detector tomography. The results provide more accurate methods and formulations to characterize and mathematically describe the detectors, valuable findings from both application and device points of views. I also introduce the concept of Gated SNSPDs, show how to implement and how to characterize them. Through series of theoretical and experimental investigations, I show performance advantages of Gated SNSPDs in terms of dead time and dark count rate, important figures for many applications like quantum key distribution. The ultimate limitations of gated operation are also explored by physical modeling and simulation steps.

Acknowledgements

The life is an integral over a huge space of possibilities. I like to express my appreciation to all those contributed on turning the possibility of making this thesis into reality.

I thank my father who thought me how to be patient with nature, and my mother for her end-less love and support.

I thank my country and its people, including many teachers, friends, colleagues and the others who all contributed in shaping my personality, knowledge and problem solving skills.

I thank my PhD advisor, professor A. Hamed Majedi, for providing me the opportunity of having an enjoyable time in graduate school, for his very positive encouragements and for his strong supports in all aspects.

I thank my MSc advisor, professor H. Kaatouzian, for guiding me to a grad school and also for his great Photonics courses that was often accompanied with interesting thoughtful discussions.

I thank Dr. Jeff S. Lundeen, with whom I collaborated on detector tomography and modeling of the detectors. Working with him thought me how the Physics looks like in the eyes of a Physicist.

I thank professors D. Ban, S. Saini, T. Jennewein (from University of Waterloo) and Jeff F. Young (from University of British Columbia) for kindly agreeing to be in my committee. I also thank professors R. R. Mansour and F. Wilhelm for attending my comprehensive exam.

I thank Institute for Quantum Computing and all its members for making a scientific and friendly atmosphere. Working in IQC has made my PhD experience rich and pleasant.

I thank Canada and its citizens for supporting my PhD work through scholarships and research grants.

I thank Dr. Z. Yan and Jean-Luc F. Orgiazzi who initially made me familiar with the lab

and showed me how to do experiments at Cryogenic temperatures.

I should thank countless friends in Waterloo, who all supported me to live in this small boring city while keeping a positive attitude. Special thanks to Behnood and his wife, Jeyron, for their very friendly supports and guidance in my first years in Waterloo. Special thanks to Sheva for the good time and nice social discussions we had together.

Finally, I would like to give my deepest appreciation to my wife Fatemeh for her constant love and support. This work would have not been possible without her great understanding and patience especially during my end-less thoughts and during very long and uninterruptable Cryogenic experiments.

To my beloved wife, Fatemeh.

Table of Contents

List of Tables

List of Figures

List of Abbreviations

APD - Avalanche Photodiode

DCP - Dark Count Probability

DCR - Dark Count Rate

DP - Detection Probability

DT - Detector Tomography

FM-SNSPD - Free-running Mode Superconducting Nanowire Single Photon Detector

FM-SPD - Free-running Mode Single Photon Detector

GM-SNSPD - Gated Mode Superconducting Nanowire Single Photon Detector

GM-SPD - Gate Mode Single Photon Detector

GR - Generation Rate

MCP - Micro Channel Plate

NIR - Near Infrared

NPD - N-Photon Detector

PICA - Pico-second Imaging Circuit Analysis

PNR - Photon Number Resolved

PMT - Photomultiplier Tube

POVM - Positive Operator-Valued Measure

QE - Quantum Efficiency

SNSPD - Superconducting Nanowire Single Photon Detector

SPD - Single Photon Detector

SQE - System Quantum Efficiency

SQUID - Superconducting Quantum Interference Device

SSPD - Superconducting Single Photon Detector

STJ - Superconducting Tunnel Junctions

TES - Transition Edge Sensors

Chapter 1

Introduction

Superconducting Nanowire Single Photon Detectors (SNSPDs) are the most practical cryogenic single photon detectors, because they provide outstanding performance in a small, easy to operate cryocooler [1]. When a superconducting nanowire is biased close to its critical current, photo-creation of a resistive hotspot followed by perturbation of the bias current, results in a short macroscopic voltage pulse that signals the detection of a single photon [2]. Quantum efficiencies up to 57% at 1550nm [3] and dark count rates well below 1Hz [4] have been reported. The timing jitter is extremely small [5] due to ultrafast photoresponse of the materials involved [6]. Furthermore, it is possible to resolve the number of photons by spatially multiplexing many nanowires in different configurations [7, 8]. The detectors are usually operated at 4.2K, although for the best performance they are often cooled down to about 2.0K.

This thesis is twofold. First, we develop a semi-empirical model for SNSPDs. The modeling is done based on the intuition that relies both on the present physical models and the experimental results. We show the model can successfully translate the raw characterization results into few parameters. The model is then evolved into a quantum-optical version that gives the form of the Positive Operator-Valued Measure (POVM) of a SNSPD. We show the resulting analytic POVM has a form that can explain the observed nonlinearities of a SNSPD under special operation conditions. The POVM is also tied to the modern concept of detector tomography (DT), both to solidify its correctness and to show

detector tomography performs well for single Photon Detectors (SPD) that significantly deviate from ideally linear response. Provided the generality of the analytic POVM and DT algorithm, the results are expected to be useful not only for the SNSPDs but also for single photon detection in general.

In the second part, we introduce the concept of gated mode SNSPDs (GM-SNSPD) as an approach to increase the maximum count rate without compromising most of the other desirable features of performance, such as quantum efficiency. SNSPDs are conventionally operated in free-running mode in which the detector should self-reset to superconducting state following a photo-detection event. The dynamics of this self-reset process imposes severe limitation on how fast the detector can be efficiently operated [9, 10]. The gated operation can be used to speed up the SNSPDs in all applications that involve pulsed optical sources while preserving the quantum efficiency and reducing the dark count rate achieved with the free-running SNSPDs. We implement the concept and develop the methods needed to characterize GM operation. The ultimate limitations of gated operation are also explored by combination of experiments, physical modeling and numerical simulations.

Before describing the models and performance improvement, it is essential to review SPDs, their performance features, and also the operation of SNSPDs. The reminder of this chapter is devoted to these topics.

1.1 Overview of Single Photon Detectors

Photons are rarely at rest. From deep space to the earth, from the electrons around nuclei to the eyes of animals and from a data center to our laptops, the photons are rapidly moving to carry information. But they still offer more. Single photons are a promising candidate for quantum information communication and processing [11]. These are the technologies that can potentially lead to radical changes in the concepts of secure communication and fast data processing. Although a classical communication channel together with a one-time pad encryption algorithm can provide perfect secrecy, no secured classical communication channel can be made for distributing the pad itself. The solution is the quantum key distribution (QKD) and single photons are naturally the best choice for

carrying the quantum information over large distances. The photons can also be exploited to improve the performance of free space communication systems [12]. Decreasing the carrier wavelength from microwaves to optical domain can lead to the realization of smaller and lighter interplanetary or intersatellite links with increased data rates. The photons carry useful information for debugging ever-changing high speed digital integrated circuits [13, 14] . The MOSFETs of a VLSI chip emit faint optical pulses that are synchronous with their switching events. The Pico-second Imaging Circuit Analysis (PICA) technique uses the time resolved microscopic images of operating VLSI circuits to extract invaluable debugging information. Fluorescence microscopy uses the photons to study the kinetics of luminescence process in various objects ranging from quantum dots to single molecules [15]. These studies can potentially lead to the realization of true single photon and entangled photon sources. A common point between all of the mentioned systems is the presence of a SPD that offers the ultimate limit in detection sensitivity. Therefore, any development in SPD technologies can benefit many fields of research and applications.

1.1.1 Performance Parameters

The performance of an ordinary optical detector is usually expressed in terms of its internal and external quantum efficiencies, responsivity, noise equivalent power and some spectral and speed related parameters. These parameters enable one to calculate the shape of the electric response of the detector by knowing the temporal profile of the optical input to the detector. But as the intensity of the input is set to smaller values, the output signal will fade into the noise sooner or later. The unique character of an SPD is that even at the smallest possible intensity - which is nothing more than the arrival of a quantum of light - it keeps its electric response discriminable from the noise. This quantum counting character makes it necessary to define new set of parameters that are suitable to describe the operation of an SPD. The typical parameters are [1]:

- Quantum Efficiency (QE) which is a wavelength and polarization dependant parameter. It specifies how efficiently the detector converts the incoming single photons to

[1]While the definitions here are rather conventional, they are by no means nor the only definition nor the most accurate one.

discriminated electric pulses. It is often defined as the ratio of the output photon count rate to the input photon rate.

- Dark Count Rate (DCR) is the measure of the noise performance of an SPD. It is the rate of the spontaneous electric pulses that is generated by a SPD in absolute darkness.

- After Pulsing Probability. Some SPDs tend to make fault electric pulses for a short period after a photodetection event. This is called after pulsing and it is described in terms of its probability.

- Maximum Count Rate specifies how small the period between successive single photon detection events can be while the SPD is still keeping the events statistically independent. Sometimes the maximum count rate is indirectly specified by defining a dead time or by using rise and fall times of the electric response of the detector. However, the best criteria would be based on the statistical independence of successive detection events.

- Timing Jitter is the measure of the timing resolution of the detector. It is determined by measuring the full width at half of the maximum (FWHM) of the histogram of delay between a sharp photo-excitation and photo-registration events.

There are also some broad categories that can help labeling SPDs. The simple SPDs can only differentiate between the presence and absence of the photons. Photon number resolved (PNR) SPDs can provide information about the number of photons that excite the detector as well. In the same way, the energy resolved and polarization state resolved SPDs can provide information about the energy and polarization state of the exciting single photons. Free-running mode SPDs (FM-SPD) detect photons irrespective of their arrival time. However, gated mode SPDs (GM-SPD) can only detect photons that arrive with in pre-specified time slots.

In addition to the intrinsic performance of SPDs, there are other criteria that may extremely enhance or deteriorate selection of a SPD for a certain application. The operation temperature is perhaps the most important one. It is ranging from sub Kelvin to room

temperatures for the present SPDs. The size of the active area of the detector, the size and weight of the whole detection system, its power consumption, the complexity of the readout circuits, the capability of being implemented in array form to provide imaging, fragility of the detector and the cost are among the other important considerations.

1.1.2 Different Technologies

Apart from the eyes of animals, photomultiplier tubes (PMTs) have the longest history of single photon detection [16]. They have been industrially produced for half a century and they are now commercially available. H10330 is a thermoelectric cooled near infrared (NIR) module from Hamamatsu [17]. It has quantum efficiency of 2% at $950 - 1700$nm and dark count rate equal to about 200KHz. Its timing jitter is 300ps FWHM and 4ns is the sum of its rise and fall times. Micro channel plates (MCPs) are the other single photon detectors that like PMTs use the photoelectric effect to convert the photons to electric current. They consist of millions of conductive glass capillaries to perform electron multiplication. Depending on the type of the photocathode used, their quantum efficiency can reach 40% in $400-850$nm but like PMTs they lose their efficiency at longer wavelengths [18].

Single photon avalanche photodiodes (APDs) are the semiconductor based SPDs. They are operated in digital or Geiger mode in which application of a bias well above their breakdown voltage makes them sensitive enough to detect single photons. The current in the Geiger mode APD must be limited and the device should be reset after a detection event. Advanced methods to achieve this include using an integrated active quenching and active reset circuit [19]. These functions protect the APD from over current, over illumination and also minimize the after pulsing probability. APDs are commonly fabricated using either silicon or InGaAs/InP. Silicon APDs have their sensitivity restricted by the silicon band gap and as the result are useful for wavelengths from visible to about 1μm. This is while InGaAs/InP APDs can operate up to about 1700nm. Mentioning some independent numerical values as the best figure of merits of present APDs is meaningless. This is because of the tight connection between the APD and its supporting circuits and also the trade-offs that exist. We use two of the commercially available APD modules to provide

some typical numerical values.

id100-20 is an actively quenched, thermoelectric cooled silicon APD module from idQuantique [20]. It operates as a FM-SPD. The diameter of the active area of the detector is equal to 20μm. Its quantum efficiency is 35% at 500nm and 4% at 900nm. The DCR of ultra low noise grade is about 1Hz while the standard grade has a DCR equal to 60Hz. Typical values of timing jitter and dead time are 40ps FWHM and 45ns respectively. This is while for having the motioned timing accuracy and also for avoiding excessive after pulsing the time between successive detection events shouldn't be less than about 1μs. This limits the maximum count rate to about 1MHz although it can be increased to about 20MHz at the expense of more after pulses.

id210 is another product from idQuantique [20]. It is an actively quenched, thermoelectric cooled InGaAs/InP APD module that can both operate as a FM or GM-SPD. For FM operation, quantum efficiency is about 10% at $1200 - 1600$nm while DCR $\approx$ 3KHz and dead time $\approx 50\mu$s. For GM operation with maximum 100MHz gating frequency and 1ns gate width, quantum efficiency is about 20% at $1200 - 1600$nm while DCR $\approx$ 5KHz and dead time $\approx 20\mu$s. The timing jitter of the detector is about 200ps FWHM. The large dead time needed to avoid excessive after pulses limits the maximum count rate to about 1MHz although the electronic circuitry allows 10MHz adjustment.

In addition to commercial products, there are research activities on APDs especially in NIR in which the performance is poorer and telecom applications demand much better SPDs. Germanium APDs have been studied to obtain better NIR performance at higher gate frequencies [21]. Ge-Si APDs use Germanium as NIR photoabsorption region and Silicon as the electron multiplier [22, 23]. NIR sensitivity and low after pulsing effect is expected because of Germanium and Silicon respectively. InGaAs/InP APDs and their supporting system are under research [24, 25, 26, 23]. Integrating Si SAPDs with their supporting circuits using standard CMOS technology toward the goal of low cost SPD arrays is under development [27, 28]. Integrating an optical amplifier with APD can potentially lead to single photon sensitivity while the APD is operating in linear mode [29]. The structure is hoped to provide sub nanosecond response with little after pulsing. HgCdTe and InAlAs/InGaAs APD structures are under study to perhaps provide single photon sensitivity in NIR while operating in analog mode [30]. Gating methods and circuits are

also under investigation [31, 32, 33, 34].

The last available category of single photon detectors exploits superconductors as the photo-detection element. These are called superconducting single photon detectors (SSPDs). They fall into three main types: transition edge sensors (TESs), superconducting tunnel junctions (STJs) and superconducting nanowire single photon detectors (SNSPDs[2]). Kelvin or sub Kelvin operation temperature requirement is their main drawback compared to PMTs and APDs. But their superior performance makes them attractive for specific applications.

A transition edge sensor consists of a micrometer sized superconducting thin film which is voltage biased close to its critical temperature. The absorption event leads to a change in the current of the device by momentarily changing its temperature. The small change in the current can then be sensed by using a chain of SQUID amplifiers. One of the most successful demonstration of TESs is for a device made from 20nm thick Tungsten film placed inside a resonant cavity [35, 36]. Its active area is 25μm$\times 25\mu$m and the operation temperature is 125mK. The quantum efficiency is equal to 85-90% at 1550nm while the DCR is negligibly small (about 1mHz). The device has photon number resolution up to fifteen 0.8eV photons and also provides 0.12eV energy resolution. The main disadvantage of it is its slow rise and fall times (100ns and 15μs respectively) that limit the maximum count rate to about 20KHz. The timing jitter of a similar detector is reported to be 72ns FWHM [37]. Using other materials including Titanium has lead to improved count rate up to about 1MHz [38, 39].

In a typical superconducting tunnel junction the absorption of a photon changes the current in a voltage biased junction by changing the concentration of quasiparticles in the absorbing film. The integral of the current would be proportional to the number and energy of the absorbed photons. STJs are mainly X-ray detectors but they can also be used in visible and infrared range. Nb/Al STJs that operate at 370mK has been shown to have quantum efficiency equal to 50% at $200 - 500$nm [40]. Ta/Al STJ array with operation temperature of 300mK provide QE equal to 50-70% at $330 - 800$nm [41]. The energy resolution of both of these devices is about 0.2eV at 500nm. However their maximum

[2]In some literatures SNSPDs are abbreviated as SSPD.

count rate is not better than 10KHz.

The photodetection element of a superconducting nanowire single photon detector consists of a meandering superconducting nanowire carrying a constant bias current close to its critical current. A single photon deposits enough heat to create a hotspot that is not superconducting. With the help of the bias current this can initiate a resistive bridge across the nanowire with some probability. The resulting voltage spike signals the detection of a single photon. At operation temperature of 2.0K and for the devices that have $10\mu\text{m}\times10\mu\text{m}$, the quantum efficiency can be 25% at 1550nm while DCR is kept below 1Hz [3, 42]. The maximum count rate of the same devices is usually reported to be some hundreds of MHz, but the numbers highly depend on the definition used. Maximum count rate is also known to deteriorate with increasing active area. The timing jitter of SNSPDs has been shown to be 29ps FWHM [5]. In spite of the attempts to show photon number resolution and energy resolution of these detectors [43, 44], no significant accomplishment has yet been reported for single element devices.

Although it is generally incorrect to write down some independent numbers to compare the performance of different SPDs, but tables that can be found in literature help doing a non-accurate but fast comparison [45, 46, 47]. It is usually true to say: nothing other than necessity can weaken the preference of using an SPD with higher operation temperature. The typical operation temperature of SNSPDs is $1-2$ orders of magnitude higher than TES and STJ detectors and $1-2$ orders of magnitude less than PMT, MCP and APD ones. Considering all of the mentioned points about the different SPDs; higher maximum count rate, lower timing jitter, lower dark count rate and higher quantum efficiency at NRI are among the points that can force selecting SNSPDs instead of higher temperature alternatives. This is while preferring TESs to SNSPDs can be due to their intrinsic photon number resolution, energy resolution and higher quantum efficiency at NIR. Except slightly higher operation temperature, STJs don't provide any advantage over TESs and SNSPDs, so their application as a visible or infrared single photon detector doesn't seem to be so probable.

1.2 Superconducting Nanowire Single Photon Detectors (SNSPDs)

Fig. 1.1 (a) shows an image of a typical SNSPD. The ultrathin superconducting film is patterned to form narrow strips. Many strips are serially connected to cover a larger active area. The device is cooled down to temperatures well below the critical temperature of the superconducting film and a bias current close to the critical current is applied to the device. The absorption of the photons by the superconductor may lead to a voltage pulse on the device terminal. The pulse after 40dB of amplification by a room temperature amplifier is shown on Fig. 1.1 (b). In this section we try to use the results of the previous research activities to construct a systematic view of SNSPDs. This perspective will be the basis of our work in the next chapter.

In this view, a three step sequential process is responsible for generating the response pulse. The first is the mechanism that governs the absorption of the single photons by the superconducting strips. The absorbed photons can lead to a photoregistration event (rising edge of the response pulse) by initiating a photodetection mechanism. A rest mechanism is also responsible for the disappearance of the generated pulse (falling edge of the response pulse).

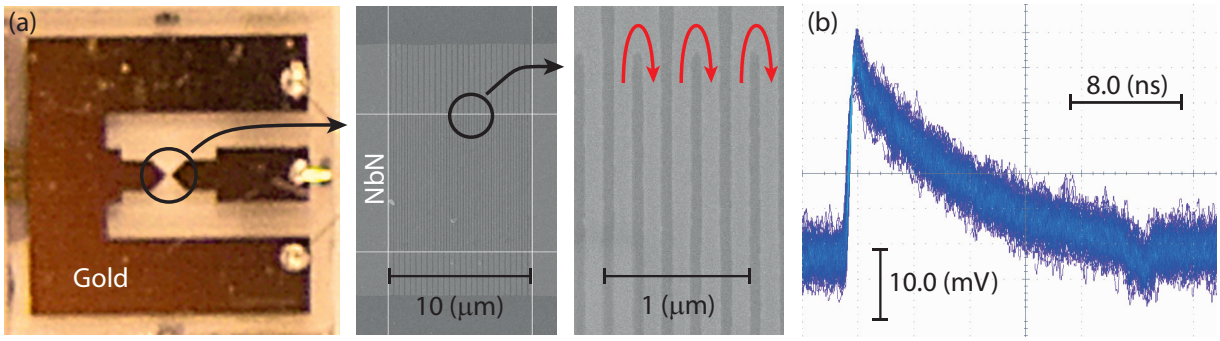

Figure 1.1: (a) Image of a typical SNSPD chip. 4nm of NbN is deposited on Sapphire and then patterned in a meander line form to make a 10μm$\times 10\mu$m active area. (b) Measured transient response of an SNSPD after 40dB amplification by a room temperature amplifier.

1.2.1 Photoabsorption Mechanism

The absorption mechanism is important because the photons can be reflected or transmitted instead of being absorbed by the superconducting strips. This limits the ultimate quantum efficiency of the detector. The absorption efficiency can be calculated based on electromagnetic simulations. Yan et al. [48] and Semenov et al. [44] have used HFSS and FEKO respectively to calculate the absorption efficiency. The goal was justification of the measured reduction in quantum efficiency at higher wavelengths. Anant et al. [49] have conducted a more rigorous research. Doing the electromagnetic based simulations with COMSOL and directly measuring the reflected and transmitted optical powers by the superconducting strips in some different configurations, they were able to directly compare the results of simulations with the results of measurements. They confirmed the correctness of the simulations at a single wavelength equal to 1550nm. The present good agreement between the theory and practice suggests a complete understanding of the photoabsorption mechanism has been achieved. This understanding has been exploited to design SNSPDs integrated with cavities [3], optical antennas [50] and waveguides [51]. These detectors can potentially have higher quantum efficiency, lower dark count rate, higher speed and even spectral resolution [52].

1.2.2 Photodetection Mechanism

The photodetection element of a SNSPD is made from a superconducting material which has the remarkable property of having absolutely zero resistivity below a critical temperature (T_C). This happens because below T_C the current is carried by pairs of electrons called Cooper pairs. The Cooper pairs which are formed because of the presence of a phonon mediated attractive force between the pairs of electrons, are able to conserve their kinetic energy. This justifies the presence of persistent current in superconductors and also explains why current carrying superconducting wires can store energy not only in the magnetic form, but also in the form of the kinetic energy of their current carriers (the latter is electrically modeled by defining a kinetic inductance). Compared to a normal metal, the other feature that the Cooper pairs bring to a superconductor, is the presence of a non zero minimum energy that is required to excite a Cooper pair and break it into two non-coupled

electrons, so called normal electrons or quasiparticles. This means that there is an energy gap for exciting carriers of current to quasiparticles. The gap which happens to be so small (on the order on some meV) makes the superconductors a reasonable material choice for making sensitive infrared detectors.

Fig. 1.2 illustrates the photodetection mechanism of SNSPDs. The absorption of a single photon makes an energetic quasiparticle by breaking a Cooper pair. The generated quasiparticle is considered energetic, because the energy of a visible to infrared photon is on the order of eV, while the pairing energy of the Coopers pairs is on the order of meV. This energetic quasiparticle can itself break further Cooper pairs and thus increase the local concentration of quasiparticles. The increased local concentration leads to the diffusion of the excess quasiparticles to the outer areas. The excess quasiparticles can also lose their energy by the cold substrate. Putting all of these together, the equation to describe the temporal and spatial concentration of quasiparticles would be [6, 53]:

$$\frac{\partial C(r,t)}{\partial t} = D\nabla^2 C(r,t) - \frac{C(r,t) - C_0}{\tau} + \frac{1}{M(t)}\frac{\partial M(t)}{\partial t} C(r,t) \tag{1.1}$$

where $C(r,t)$ is the concentration of quasiparticles, D is the diffusivity of the normal electrons, τ is the quasiparticle to substrate relaxation time, C_0 is the quasiparticle concentration for non-excited superconducting film at a temperature equal to the substrate temperature and $M(t)$ is a multiplication factor that describes the Cooper pair breaking by energetic quasiparticles. Solving the equation for a 2D film and assuming superconducting film is a normal metal wherever $C(r,t)$ is equal to C_0 at the critical temperature, the diameter of a normal circle (so called hotspot) can be calculated. The hotspot has an initial growth and a later annihilation. Because the current prefers to pass through the superconducting parts, the presence of the hotspot increases the current density on the sidewalks, see Fig. 1.2 (b). Assuming the current is uniformly and instantly redistributed in the superconducting areas around a hotspot, it is easy to calculate the current density in the sidewalks. If at any moment this current density become greater than the critical current density of the superconducting film at temperature equal to the substrate temperature, a resistive barrier will be formed across the superconducting strip. This can lead to a voltage pulse and justifies the photodetection mechanism of the SNSPDs.

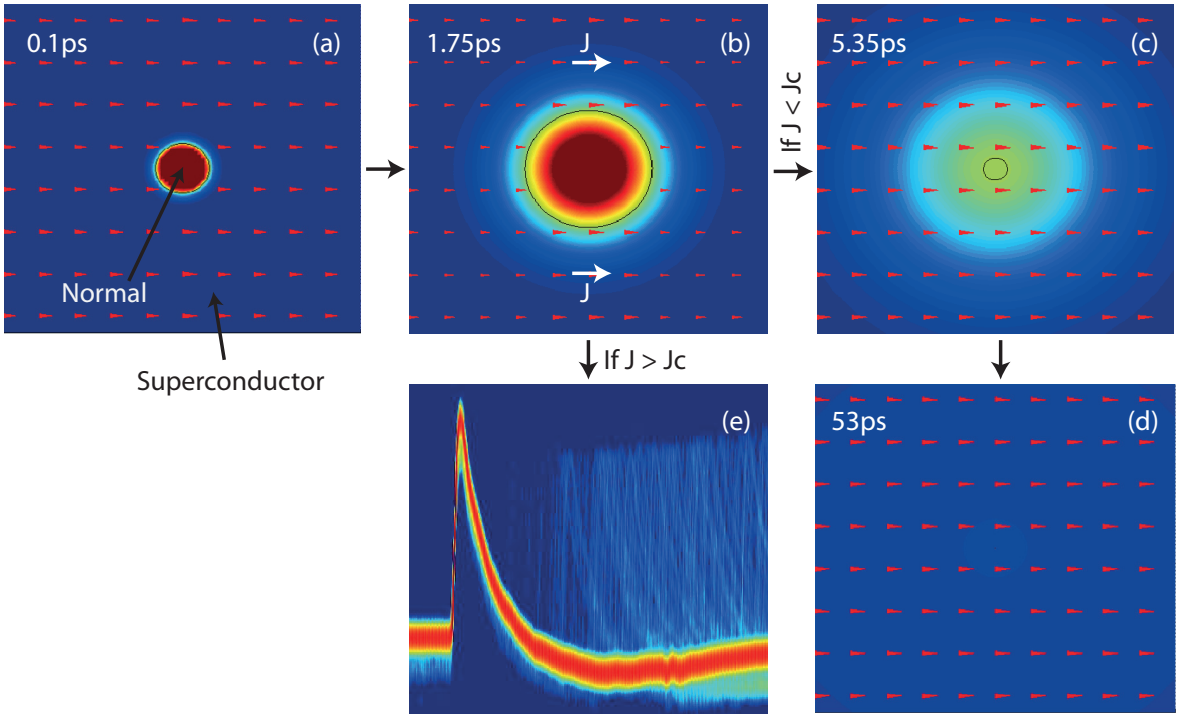

Figure 1.2: Simulation of creation, growth and annihilation of a hotspot based on Eq. (1.1). All the material parameters are from [6]. The arrows show the density of super current. The times are measured from the photon absorption.

The photodetection mechanism as described above was first formulated by Semenov et al. [6] in 2001 to predict the possibility of using superconducting nanowires to make single photon detectors. It was right after that when the first SNSPD was experimentally demonstrated by the same group [54]. However the later characterization results often lead to contradictory results.

At a fixed wavelength and temperature, the calculations suggest 100% of photodetection probability for the bias currents above a threshold value and no chance of photodetection for biases less than the threshold. Fig. 1.3 shows a typical measurement of quantum efficiency versus bias current. The similarity between the prediction and measurement is

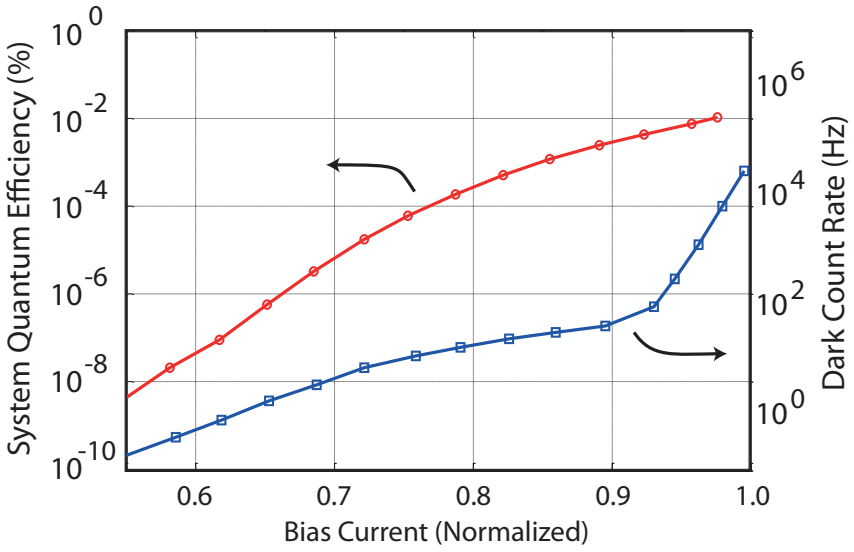

Figure 1.3: Measured quantum efficiency and dark count rate versus bias current normalized to the critical current [55]. The detector is made from 4nm NbN film deposited on sapphire and patterned in the form of 120nm wide strips. The system quantum efficiency is defined later in Eq. (2.21).

not perfect. At a fixed bias current and temperature, the calculations suggest 100% of photodetection probability for the wavelengths less than a threshold value and no chance of photodetection for wavelengths higher than the threshold. This is because the maximum hotspot diameter decreases with the wavelength. However, typical measurements (see [42] for example) show this is not the case.

Fig. 1.4 shows the calculation of the diameter of hotspot versus time at different temperatures for a 1eV incident photon. It predicts a reduction in the maximum diameter of hotspots as the temperature goes down. This suggests the quantum efficiency should be higher at a higher temperature. But the measurement results [42] show the dependency of quantum efficiency on the temperature is exactly the reverse of this. Referring to Fig. 1.4, the maximum hotspot diameter for a 1eV photon is about 11nm at 2K. This means a detector made from 120nm wide strips shouldn't have any sensitivity to the 1eV photons for

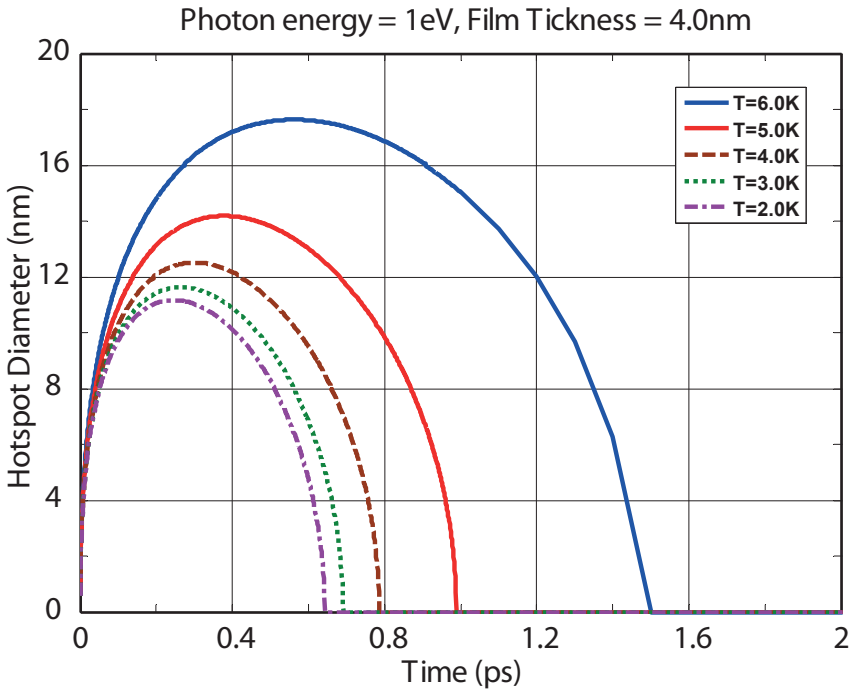

Figure 1.4: Calculation of the hotspot diameter versus time for different substrate temperatures based on Eq. (1.1). All the material parameters are from [6] which is for NbN on Sapphire. The thickness of superconducting film was assumed to be 4.0nm and the energy of the photon was 1eV.

bias currents less than $(120 - 11)/120 = 91\%$. This is while the measurements of Fig. 1.3 show significant response for biases less than 91%. In the same way one can conclude the detector shouldn't be sensitive to 5μm photons. This clearly contradicts the measurements of [56].

An alternative photoresponse description also exists and is regarded as a refinement of the hotspot picture [57]. Equation (1.1) is assumed to be valid. The number of quasiparticles in a slab with the length equal to the coherence length is calculated with the knowledge of spatial and temporal distribution of quasiparticles. Having the number of quasiparticles in the slab, the number of Cooper pairs in the same volume is determined. With the knowledge of applied current and the number of Cooper pairs the average veloc-

ity of Cooper pairs can be calculated. If this velocity exceeds the critical velocity at the substrate temperature then the superconducting slab will switch to the normal state and a voltage pulse will appear on the device terminal. However, this refined hotspot model can also only provide some qualitative agreements with the results of experiments [57].

In spite of the contradictions, the mentioned qualitative descriptions of the photoresponse mechanism has remained the most common way to explain the operation principle of SNSPDs since 2001 [58, 59, 4, 60, 61, 62, 42, 45]. This is while the presence of contradictions is well understood and accepted. "At present there is no comprehensive model describing the resistive response of the thin and narrow superconducting strip to the absorbed photon although in our previous papers we already discussed a simple model describing SSPD Photoresponse." Golt'sman wrote in 2005 [60].

The presented models and contradictions clarifies that in contrast to the photoabsorption mechanism a good understanding of the photodetection mechanism of SNSPDs has not yet been achieved. This is while photodetection is the most important feature of any photodetector and its understanding should be regarded as a fundamental requirement for making engineered SNSPDs. This has been our initial motivation of our semi-empirical modeling work in chapter 2.

1.2.3 Reset Mechanism

Since the initial proposal of SNSPDs till 2006, it was believed that the maximum count rate of SNSPDs is at least on the order of some GHz. This was because the timing values in the hotspot model are all on the order of tens of picoseconds (see the times in Fig. 1.2). There were also some supporting experiments [63]. But Kerman et al. have rigorously proved in 2006 that because of the presence of a reset mechanism the typical maximum count rate of SNSPDs is much lower [64]. Using two faint optical pulses with a variable delay between them, they measured the probability of detecting both of the pulses versus pulse separation. The results confirmed for keeping the quantum efficiency constant, depending on the total length of the superconducting strips, the typical count rate shouldn't be higher than a few hundreds of MHz. They also modeled a SNSPD as an inductor with kinetic origin placed in series with the parallel connection of a switch

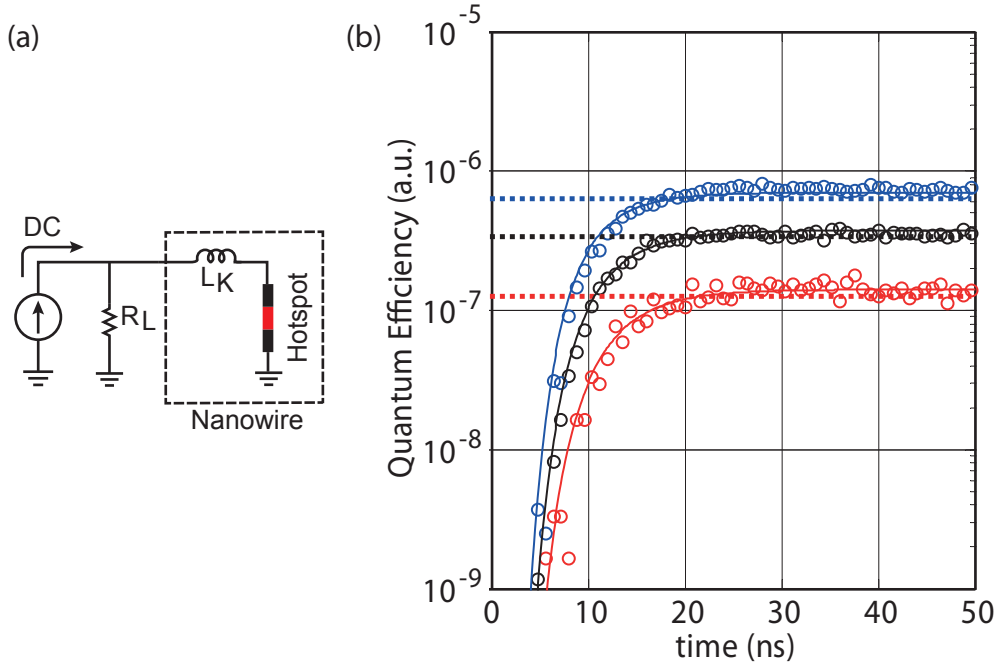

Figure 1.5: (a) Electrical model of a SNSPD as described in [64]. (b) Momentary reduction in quantum efficiency following a photodetection event. The circles are measured points at different bias currents (from top to bottom 13.28, 14.25 and 15.23μA) and the curves are calculations based on the model. (We have used autocorrelation methods as will be discussed for Fig. 4.3 (a), to measure this.)

(hotspot) and a normal state resistor (see Fig. 1.5). The photodetection event would be equivalent to a temporary opening of the switch. When the switch is open the current through the SNSPD is decreased and at the same time the voltage on the load resistor is increased with a time constant of $\tau_r = L_k/(R_n + 50)$ (Assuming the load resistance is a standard microwave load of 50Ω). The closure of the switch reverses the direction of the change of the mentioned current and voltage, and the new time constant would be $\tau_r = L_k/(50)$. This simple model is very successful in predicting the pulse shape of the detector (Fig. 1.1 (b)). It justifies why the fall time is much longer than the rise time. Also it explains the variation of count rate versus optical pulse separation as the result of variation of current through the superconducting strips at the moment of second optical

pulse arrival (see Fig. 1.5 (b)).

The fall time of voltage pulse from the detector or equivalently the rise time of the current through SNSPD can be decreased to increase the maximum count rate by increasing the 50Ω microwave load resistor. However, Yang et al. in 2007 proposed a thermo-electrical model to conclude the maximum count rate cannot be increased a lot by increasing the termination resistor [65]. The electrical model is something similar to the one in Fig. 1.5 (a), and the thermal part is a typical 1D heat transfer model. After a photodetection event a resistive barrier is created across the superconducting strip. The current that passes through the strip dissipates electrical energy in the resistive section. This expands the length of the resistive section. At the same time the current through the strip drops. The combined action of the increased size of resistive section and decreased current may lead to a return to the superconducting state or a latching in the resistive state. The simulation shows the latching occurs for larger termination resistors. So the maximum count rate cannot be increased a lot in this way because the device will latch. This has also been experimentally confirmed [65]. Also later investigations provided more insight into this phenomena [9, 10].

Although more accurate models can also be developed, the limitation on the maximum count rate seems to be generally accepted. Improving this limitation has been our motivation for proposing and experimentally demonstrating gated mode operation of SNSPDs. We'll show in gated mode the maximum count rate can be higher by more than one order of magnitude compared to free-running operation. This will be described in more detail in chapter 4.

Chapter 2

Semi-empirical modeling of SNSPDs

Different models for justification of the characters of SNSPDs were mentioned in the previous chapter. Coming from different underlying physics and also justifying the operation of the device at different moments after the arrival of photons, there is naturally little interrelationship between these models. But can the photodetection mechanisms be studied separately from the other ones? The fact is all of these physical phenomena have a collaborative effect in occurrence of the measurable response of the device. For instance, dark count, photoresponse and the kinetic inductance have very different physical origins. But the photoresponse at time t is dependent on a dark count event at time $t - \Delta t$ and the degree of dependence is determined by the speed of the device which itself is a function of kinetic inductance. So for correctly interpreting the results of measurements, a unified model for the operation of SNSPDs is required.

Here we present the results of our mathematical approach to model a SNSPD as a unique entity with photons as its input and the electrical pulses as its output. The chapter starts with developing the model and derivation of different useful relations. It will continue to an explanation of the supporting experiments and discussions. Much of this work has been published in [66, 55, 67].

2.1 Model Development

Modeling the photodetection mechanism is the first step to construct our mathematical structure. The photons that are absorbed by the strips of superconductor make a perturbation that can lead to formation of a resistive barrier. The exact physics of the perturbation is still unknown. It may be in the form of a hotspot as explained in the hotspot model [6]. This is while the large jitter and average time delay between photon absorption and electric pulse generation [68] suggest the process of conversion of an absorbed photon to an electric pulse should be viewed as a random process. A method to describe such a process is to assume the absorbed photon initiates a resistive barrier generation rate function $GR(t)$. Thus $GR(t)\Delta t$ would be the probability of a resistive barrier generation in the time interval Δt and the integral of $GR(t)\Delta t$ over the total operational time would be the intrinsic quantum efficiency of the detector. Working with $GR(t)$ through all of the modeling steps seems to be tedious. So we do an approximation by defining an average perturbation life time τ_h and a constant resistive barrier generation rate GR such that $GR\ \tau_h$ would be equal to the integral of $GR(t)\Delta t$ over the total detection time interval. We call τ_h the average hotspot life time to be consistent with the previous models. But it is generally describing the life time of the perturbation that can potentially lead to an electric pulse on the terminals of the device.

Being equipped with the concepts of τ_h and GR, we can now start adding other experimentally observed features of the SNSPDs to the model. When the device is in absolute darkness, no photo-induced perturbation exists on the superconducting strips. In this case the rate of electric pulse generation can be modeled by defining a rate G_0 which describes the Dark Count Rate of the device. When exactly one photo-induced perturbation exists somewhere on the superconducting strip, the total rate of electric pulse generation by the device will be enhanced to a value more than G_0. This enhancement in the total GR can be included in the model by defining G_1 such that $G_0 + G_1$ will be the total GR of the device in such a condition. Adding another perturbation on the strip should enhance the total GR to a value at least equal to $G_0 + 2G_1$. But the experiments suggest the enhancement can be even more because of the nonlinearities of SNSPDs [58]. This can also be modeled by defining G_2 such that $G_0 + 2G_1 + G_2$ will be the new total GR. Continuing the same

line of reasoning it is possible to write

$$GR(n_h) = \sum_{m=0}^{n_h} \binom{n_h}{m} G_m \tag{2.1}$$

where $GR(n_h)$ is the GR of a device with exactly n_h photo-induced perturbations on its superconducting strips, G_0 is the GR when no photo-induced perturbation exists and other G_m values describe the enhancement in total GR when the number of simultaneously present perturbations increases from $m-1$ to m. Because for large values of m there is negligible difference between $m-1$ and m, it can also be safely assumed

$$G_m = 0 \quad : m \geq M \tag{2.2}$$

where M is the number of G_m values that have significant effect on determining the total GR.

The number of photo-induced perturbations can be determined by assuming the optical source is a laser that generates photons with Poisson distribution and also by considering all of the losses between the source and absorbed photons as stationary ergodic random processes that are independent of the past times. Under these conditions the n_h at time t can be described by a Poisson distribution with a mean equal to

$$\overline{n_h(t)} = 10^{\frac{(\alpha_1+\alpha_2+\alpha_3)}{10}} \int_{t-\tau_h}^{t} \frac{P_S(t-\tau_d)}{h\upsilon} dt \tag{2.3}$$

where α_1 is the loss[1] that is added manually for characterization purposes, α_2 is the coupling loss between the input of the detector system and the small active area of the SNSPD, α_3 is the loss due to limited absorption of the photons by the superconducting strips, P_S is the power emitted by the source, τ_d is the average time delay between the emission of photons by the source and their absorption by the strips and τ_h as defined previously is the hotspot life time. Here it is implicitly assumed that the life time of different processes that are described by different G_m values are all the same. The total resistive barrier generation rate at time t can now be written as

$$GR_t(t) = \sum_{n_h=0}^{\infty} GR(n_h) \frac{[\overline{n_h(t)}]^{n_h} \times e^{-\overline{n_h(t)}}}{n_h!} \tag{2.4}$$

[1]The losses in this chapter are specified in dB.

Combining Eq. (2.1), Eq. (2.2) and Eq. (2.4) one can find:

$$GR_t(t) = \sum_{n_h=0}^{\infty} \sum_{m=0}^{n_h} \binom{n_h}{m} G_m \frac{[\overline{n_h(t)}]^{n_h} \times e^{-\overline{n_h(t)}}}{n_h!} = \sum_{m=0}^{M-1} G_m \frac{[\overline{n_h(t)}]^m}{m!} \tag{2.5}$$

Equation (2.5) gives the total generation rate of the detector at time t but this is not the value that can be measured directly from the device terminal. The SNSPDs like any other kind of SPD has a dead time during which the device after a detection event has smaller probability of detecting another incoming photon. For the present detectors this has been shown to be due to the kinetic inductance of the nanostrips [64]. We model this effect by defining an average dead time τ_{dt} during which the detector has no probability of detecting another photon. So the total measurable count rate of the device would be

$$CR_t(t) = GR_t(t) \left(1 - \int_{t-\tau_{dt}}^{t} CR_t(t)dt\right) \tag{2.6}$$

The equations (2.3), (2.5) and (2.6) can be used to calculate the measurable count rate of SNSPDs for any arbitrary input laser power.

2.1.1 Simplified Equations for CW Laser

The equations of the model can be solved easily when the light source is a CW laser. Under this condition the following equations will relate the measured count rate to the power of the laser.

$$\overline{n_h} = \frac{P_S \tau_h}{h\upsilon} 10^{\frac{(\alpha_1+\alpha_2+\alpha_3)}{10}} \tag{2.7}$$

$$GR_t = \sum_{m=0}^{M-1} G_m \frac{[\overline{n_h}]^m}{m!} \tag{2.8}$$

$$CR_t = \frac{GR_t}{1 + GR_t \tau_{dt}} \tag{2.9}$$

At very high attenuations where the average of n_h and as a result $GR_t\ \tau_{dt}$ is so small, CR_t will be independent of τ_{dt} and equal to GR_t. This is reasonable because when the

device is excited at very low rates, the actual speed of it shouldn't effect its measurable count rate. Under the same condition and depending on the values of the different summation terms in Eq. (2.8), any of the G_m mechanisms can be the dominant photodetection mechanism. That means simply setting P_S to very small values doesn't guarantee the measured counts be the result of single photon detection. At very high optical intensities where $GR_t\ \tau_{dt}$ becomes much greater than one, the measured count rate of the device will be equal to $1/\tau_{dt}$ and independent of the intensity of the light source. This shows the dead time limited operation of the detector. We also note that in the intermediate optical intensities the limited speed of the detector affects the measured count rate. Do the nonlinear changes of the count rate with optical intensity mean the efficiency of converting photons to electric pulses is changing? No, the change is just because of the speed limitation of the detector or maybe because of the presence of G_2, G_3 and etc. These points clarify how the model which converts the results of independent measurements to a single set of parameters can be important for correct interpretation of the results of experiments.

2.1.2 Simplified Equations for Wide Laser Pulses

We also tried to approximate the equations of the model for the pulsed excitation. Depending on the relative magnitudes of laser pulse duration and the hotspot life time, two distinct cases as shown in Fig. 2.1 are considered. For the wide laser pulse case the duration of the laser pulse is much greater than the hotspot life time. So the time of optically enhanced resistive barrier generation rate would be equal to the duration of laser pulse itself. For the narrow laser pulse case this time would reduce to the minimum possible value which is equal to hotspot life time. In this section equations for the wide pulses are developed and the next section covers the narrow case.

When the light source is a pulsed laser with repetition rate F_S and duration t_S that satisfies the following conditions, the equations of the model can be further simplified.

$$\begin{cases} \tau_h << t_S << \tau_{dt} \\ F_S << \frac{1}{\tau_{dt}} \end{cases} \tag{2.10}$$

Approximating the laser pulse by a rectangular intensity profile with duration t_S and

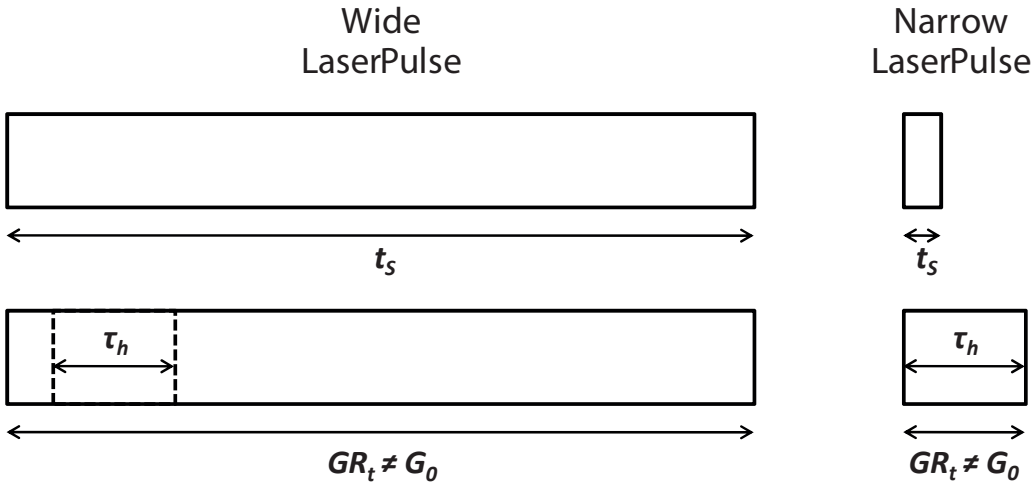

Figure 2.1: For the wide laser pulse case the duration of the laser pulse is much greater than the hotspot life time. So the time of optically enhanced resistive barrier generation rate would be equal to t_S. For the narrow laser pulse case this time would reduce to the minimum possible value which is equal to hotspot life time.

neglecting τ_d which is not important for our present calculations, the Eq. (2.3) can be approximated as:

$$\overline{n_h(t)} \cong \begin{cases} n_{hp} = N_{sp} \ \frac{\tau_h}{t_S} \ 10^{\frac{(\alpha_1+\alpha_2+\alpha_3)}{10}} & 0 \leq t \leq t_S \\ 0 \quad Otherwise \end{cases} \tag{2.11}$$

where n_{hp} is the average number of simultaneously active perturbations or hotspots during the laser pulse and N_{SP} is the average number of photons emitted by the laser per pulse. Equations (2.11) and (2.5) can now be combined to yield

$$GR_t(t) \cong \begin{cases} GR_{tp} = \sum_{m=0}^{M-1} G_m \frac{[n_{hp}]^m}{m!} & 0 \leq t \leq t_S \\ G_0 \quad Otherwise \end{cases} \tag{2.12}$$

where GR_{tp} is the rate of resistive barrier generation during the times when the superconducting strips are excited by the laser pulses. Equation (2.6) can be solved for the recent

GR_t under the conditions that are written in Eq. (2.10). The result will be

$$CR_t(t) \cong \begin{cases} CR_{tp} = GR_{tp}\ exp(-GR_{tp}\ t) & 0 \le t \le t_S \\ \frac{G_0}{1+G_0\tau_{dt}} & Otherwise \end{cases} \tag{2.13}$$

where CR_{tp} is the count rate of the device during the times when it is excited by the laser pulses. The average of $CR_t(t)$ as written in Eq. (2.13) is equal to

$$CR_t \cong \frac{G_0}{1+G_0\tau_{dt}} + F_s\left[1 - \exp\left(-GR_{tp}t_S\right)\right] \tag{2.14}$$

Equations (2.11), (2.12) and (2.14) can predict the outcome of an experiment under the assumed conditions. High intensity of the source with proper G_m values can make $GR_{tp}t_S$ much higher than one which according to the Eq. (2.14) leads to a total average count rate that is saturated to the repetition rate of the laser. Faint laser pulses can make $GR_{tp}t_S$ much less than one which leads to a linear relation between GR_{tp} and CR_t. The rather complicated relation between N_{SP} and CR_t again shows why a model like the one developed here is needed to acurately extract performance parameters of the device from the measurements.

2.1.3 Simplified Equations for Narrow Laser Pulses

The general model can also be simplified for a light source that generates narrow laser pulses (see Fig. 2.1) with the following conditions.

$$\begin{cases} t_S << \tau_h << \tau_{dt} \\ F_S << \frac{1}{\tau_{dt}} \end{cases} \tag{2.15}$$

In this case the laser pulses can be viewed as impulses that include N_{SP} photons on average. Neglecting t_d the Eq.(2.3) is approximated as

$$\overline{n_h(t)} \cong \begin{cases} n_{hp} = N_{sp}\ 10^{\frac{(\alpha_1+\alpha_2+\alpha_3)}{10}} & 0 \le t \le \tau_h \\ 0 \quad Otherwise \end{cases} \tag{2.16}$$

where n_{hp} is the average number of simultaneously generated perturbations per laser. In exactly the same way that we derived Eq. (2.13) for the case of wide laser pulses, it is possible to find:

$$GR_t(t) \cong \begin{cases} GR_{tp} = \sum_{m=0}^{M-1} G_m \frac{[n_{hp}]^m}{m!} & 0 \leq t \leq \tau_h \\ G_0 \quad Otherwise \end{cases} \tag{2.17}$$

$$CR_t(t) \cong \begin{cases} CR_{tp} = GR_{tp}\ exp(-GR_{tp}\ t) & 0 \leq t \leq \tau_h \\ \frac{G_0}{1+G_0\tau_{dt}} \quad Otherwise \end{cases} \tag{2.18}$$

where GR_{tp} is the rate of resistive barrier generation during the time equal to t_h after the laser excitation and CR_{tp} is the corresponding total count rate. Finally the average total count rate is found to be

$$CR_t \cong \frac{G_0}{1 + G_0\ \tau_{dt}} + F_s\left[1 - \exp\left(-GR_{tp}\tau_h\right)\right] \tag{2.19}$$

Equations (2.16), (2.17) and (2.19) can be used to calculate the result of an experiment for the assumed conditions. Comparing Eq. (2.11) with Eq. (2.16) , it is possible to see an enhancement in n_{hp} equal to t_h/t_S for the narrow laser pulse case. This can lead to higher CR_t which is reasonable because of the nonlinear behavior[2] of the detector. We also pay attention that both of the Eq. (2.14) and Eq. (2.19) approach the same value of CR_t for faint laser pulses and under the assumption that G_1 is the dominant photodetection mechanism. This is again rational because when just a single photon is present in the system, the exact time that it excites the detector shouldn't affect the total count rate.

2.1.4 Equation for Dark Count Rate

The dark count rate (DCR) is determined by measuring the total count rate of the device when the intensity of the light source is set to zero. Under this condition, Eq. (2.4) gives a fixed total resistive barrier generation rate equal to G_0 and then Eq. (2.6) is used to find

$$DCR = \frac{G_0}{1 + G_0\ \tau_{dt}} \tag{2.20}$$

[2]Such nonlinear effects are absent in the standard description of an ideally linear single photon detector. However our model formulates these effects and discussions highlight the importance of considering them. This would be discussed in more detail in the next chapter.

The equations of CW laser case can also be used to calculate DCR. This gives a value exactly the same as Eq. (2.20). If instead, equations of either of the pulsed laser cases be used to calculate the DCR, the result would be the Eq. (2.20) plus an additional term. These additional terms are all negligibly small. This is because a detector for being named as a detector should have $G_0\ \tau_{dt}$ less than one. This fact together with Eq. (2.10) or Eq. (2.15) ensures $G_0\ t_S << 1$ and $G_0\ \tau_h << 1$. This means the second term of Eq. (2.14) and Eq. (2.19) can be approximated as $F_S\ G_0\ t_S$ and $F_S\ G_0\ \tau_h$ respectively, and both of these expressions are much less than DCR. It is also worth mentioning that the value of DCR is less than G_0. This is simply because during the measurement there are some dead times when the detector cannot make more electric pulses.

2.1.5 Equations for Quantum Efficiency

A widely accepted definition of quantum efficiency (QE) and system quantum efficiency (SQE) of a SNSPD is based on the measurement of total count rate of the device on a long period of time while the average optical power is kept constant. It is also common to do the measurements under low intensity optical illumination. We therefore define QE and SQE as

$$QE \equiv \frac{SQE}{10^{\left(\frac{\alpha_2}{10}\right)}} \equiv \frac{CR_t - DCR}{10^{\left(\frac{\alpha_1+\alpha_2}{10}\right)} \int_{t-1}^{t} \frac{P_s(t)}{h\upsilon} dt} \tag{2.21}$$

For CW laser and under low intensity condition where the $GR_t\ t_{dt}$ is much less than one, the equations (2.7)), (2.8), (2.9) and (2.21) can be used to find

$$QE = 10^{\frac{\alpha_3}{10}} \sum_{m=1}^{M-1} \frac{G_m \tau_h}{m!} \left[\frac{P_S\ \tau_h}{h\upsilon} 10^{\left(\frac{\alpha_1+\alpha_2+\alpha_3}{10}\right)} \right]^{m-1} \tag{2.22}$$

For wide laser pulses and under low intensity condition where the $GR_{tp}\ t_S$ is much less than one, the equations (2.11), (2.12), (2.14) and (2.21) are used to get

$$QE = 10^{\frac{\alpha_3}{10}} \sum_{m=1}^{M-1} \frac{G_m \tau_h}{m!} \left[N_{sp} \frac{\tau_h}{t_S} 10^{\left(\frac{\alpha_1+\alpha_2+\alpha_3}{10}\right)} \right]^{m-1} \tag{2.23}$$

For narrow laser pulses and under low intensity condition where the $GR_{tp}\ t_h$ is much less than one, the equations (2.16), (2.17), (2.19) and (2.21) are combined to yield

$$QE = 10^{\frac{\alpha_3}{10}} \sum_{m=1}^{M-1} \frac{G_m \tau_h}{m!} \left[N_{sp}\ 10^{\left(\frac{\alpha_1+\alpha_2+\alpha_3}{10}\right)} \right]^{m-1} \tag{2.24}$$

There is a nice repeated pattern in equations (2.22) to (2.24). In all of them the expression inside the bracket is equal to the average number of simultaneously active perturbations or so called hotspots during a time interval equal to the perturbation life time. We also note that only the first term in the summation is always independent of the intensity of the light source and this term may or may not be the dominant factor that determines the QE as defined by Eq. (2.21).

QE is a useful parameter only if it is independent of the optical excitation. Equations (2.22) to (2.24) show for nonlinear detectors QE is not sufficient and a new set of parameters are needed to describe their operation. This is addressed in our work in next chapter.

2.1.6 Modeling the Intrinsic Timing Jitter

A very narrow laser pulse that excites the SNSPD at $t = 0$, can potentially lead to the formation of a resistive barrier on the superconducting strip during a limited time after its absorption. The probability distribution function of the times when the resistive barriers are generated determines the intrinsic jitter profile of the detector.

The narrow laser pulse means equations (2.16) to (2.18) should be used in this case. Equation (2.18) can be interpreted as the measurable jitter profile of the detector. Assuming negligible DCR and faint laser pulses for which $GR_{tp}\ \tau_h$ is much less than one, Eq. (2.18) predicts a rectangular measurable jitter with duration equal to τ_h. This is while the measurements show a Gaussian jitter shape. The source of this error is in the approximation that we did in the beginning of the modeling where $GR(t)\Delta t$ was approximated by $GR\ \tau_h$. For the present case this simplifying approximation can be relaxed without losing compatibility with the previous equations. Equation (2.17) is our starting point to apply

the timing parameters to the model. It gives a rectangular total generation rate versus time. We replace this equation by the following function.

$$GR_t(t) \cong \begin{cases} GR_{tp}(t) = G_0 + \frac{\tau_h (GR_{tp} - G_0)}{\tau_\sigma \sqrt{2\pi}} \ \exp\left[-\frac{\left(t - \frac{\tau_h}{2}\right)^2}{2\tau_\sigma^2} \right] & 0 \leq t \leq \tau_h \\ G_0 \quad Otherwise \end{cases} \tag{2.25}$$

The choice of Gaussian function is because of the results of jitter measurements of this type of detectors. It will be also shown that the measurements suggest τ_σ is much smaller than τ_h. Exploiting this fact, we have chosen the normalizing factors such that the integral of Eq (2.25) from zero to τ_h be equal to the same integral of Eq. (2.17). That means, as physically expected, by replacing Eq. (2.17) with Eq. (2.25) the total probability of a resistive barrier generation will not change. Equation (2.25) should now be inserted back into Eq. (2.6) to find the $CR_t(t)$. The result is

$$CR_t(t) \cong \begin{cases} CR_{tp}(t) = GR_{tp}(t) \ \exp\left[-\int_0^t GR_{tp}(t) dt \right] & 0 \leq t \leq \tau_h \\ \frac{G_0}{1 + G_0 \tau_{dt}} \quad Otherwise \end{cases} \tag{2.26}$$

The integral of Eq. (2.26) from zero to τ_h gives the probability of generation of a resistive barrier after a laser excitation. Carrying out the algebraic work, one obtains a value that is equal to the coefficient of F_S in Eq. (2.19). This ensures the previous equations for narrow laser pulse are still valid and can be viewed as simplified but accurate replicas of the present equations.

Equation. (2.26) is now the measurable jitter profile of the SNSPD. When $GR_{tp}\ \tau_h$ is much less than one, Eq. (2.26) predicts a perfectly Gaussian measurable timing jitter. As $GR_{tp}\ \tau_h$ is increased the measurable jitter profile will be squeezed from the right side and the mean point will be shifted from $\tau_h/2$ toward smaller values. Finally for very intense lasers that $GR_{tp}\ \tau_h$ is very large, the measurable jitter profile will approach an impulse near t equal to zero. This is physically reasonable because the intense laser can start very large number of random processes immediately after getting absorbed by the superconducting strips. So the total chance of generating a resistive barrier during initial steps after the photoexcitation increases which itself means lower jitter and lower average delay. We note that the measurable timing jitter as can be seen from Eq. (2.26) is different from the

intrinsic photodetection timing jitter of the detector as characterized by τ_σ in Eq. (2.25). It is also worth mentioning that the measurable timing jitter as calculated here should be regarded as the ultimate timing jitter that can be measured in an ideal setup. In a practical setup other sources of jitter, specially the one that is associated with the noise and limited rise time of the amplifiers, should also be considered for interpreting the measured results.

2.1.7 Calculation of the Average Time Delay

According to Eq. (2.25), the intrinsic average delay for generating a resistive barrier is equal to $\tau_h/2$. However the detector does not have a zero dead time and this fact affects the average delay that can be measured from the device terminal. Noting $CR_{tp}(t).dt$ is the probability of a click between t and $t+dt$, the measurable average delay can be calculated as

$$\overline{\tau_{dealy}} = \frac{\int_0^{\tau_h} CR_{tp}(t)tdt}{\int_0^{\tau_h} CR_{tp}(t)dt} = \frac{\int_0^{\tau_h} CR_{tp}(t)tdt}{1-\exp\left(-GR_{tp}\tau_h\right)} \tag{2.27}$$

where CR_{tp} is given by Eq. (2.26) and GR_{tp} is given by Eq. (2.17). For $GR_{tp}\ \tau_h$ much less than one, Eq. (2.27) will reduce to $\tau_h/2$ as expected. For $GR_{tp}\ t_h$ much higher than one, paying attention to the explanations following Eq. (2.26), it can be concluded that the measurable average delay will approach to zero.

We have shown in the previous section that the Eq. (2.18) should not be trusted for timing calculations. But here we want to use it to calculate the measurable average time delay. This result that will be used just for comparison would be

$$\overline{\tau_{delay}} \approx \tau_h \frac{\frac{1}{GR_{tp}\tau_h} - \left(1+\frac{1}{GR_{tp}\tau_h}\right)\exp\left(-GR_{tp}\tau_h\right)}{1-\exp\left(-GR_{tp}\tau_h\right)} \tag{2.28}$$

Figure 2.2 shows a plot of this equation. We pay attention that the behavior of the curve is the same as what is explained above for Eq. (2.27). $GR_{tp}\ \tau_h$ is in fact the average number of resistive barriers that are expected to be generated along the nano strips of the detector as the result of a laser pulse excitation. When this number is much less than one, either one or zero random processes (resistive barrier generation) will be initiated by a laser pulse. So the average delay would be equal to $\tau_h/2$. But simultaneous initialization

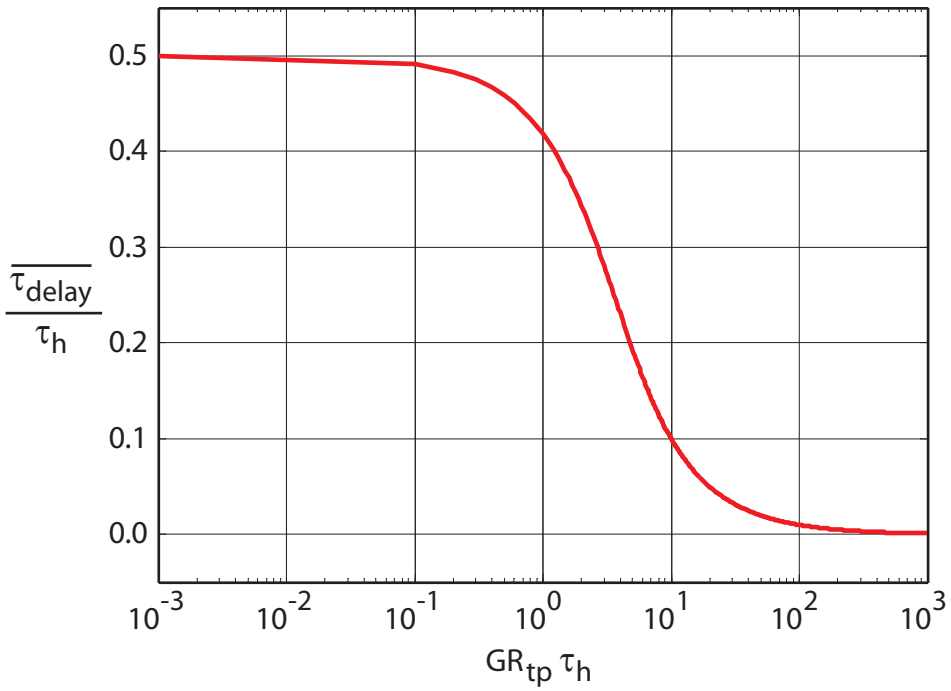

Figure 2.2: The average time delay normalized to the hotspot life time versus $GR_{tp}\ \tau_h$ calculated using Eq. (2.28).

of more random processes at higher $GR_{tp}\ \tau_h$ leads to a reduction of the average delay. The experimental confirmation of this mathematical conclusion can be used to verify the correctness of the initial assumptions that the model was made on. This would be the subject of the subsection 2.4.4 of this chapter.

2.2 Experimental Setup

Figure 2.3 illustrates the block diagram of the setup we used to perform experimental characterization of the SNSPD [66]. The active area of the SNSPDs used in this work is made from 4nm thick NbN superconductor film patterned in meander line shape with a 120nm line width and a filling factor of 60%. The total active area is 10μm$\times 10\mu$m and the substrate is Sapphire. The device which is fabricated by Scontel Co., Moscow, Russia is shown in Fig. 1.1 (a). The SNSPD is installed in a fiber coupled cryogenic package as shown in Fig. 2.4. A hole exists at the center of the base of the package, right below the active area of the device. A microscope objective lens together with a CCD camera captures a magnified image of the active area through the hole. An infrared LED is initially used to find the right position of the center of the active area. Then the fiber is installed on the cover of the package. Shining the fiber with a laser and by using the hole and imaging system to observe the location of bright spot on the SNSPD, the position of the spot is adjusted. The optical alignment is done when the bright spot overlaps with the active area as far as possible.

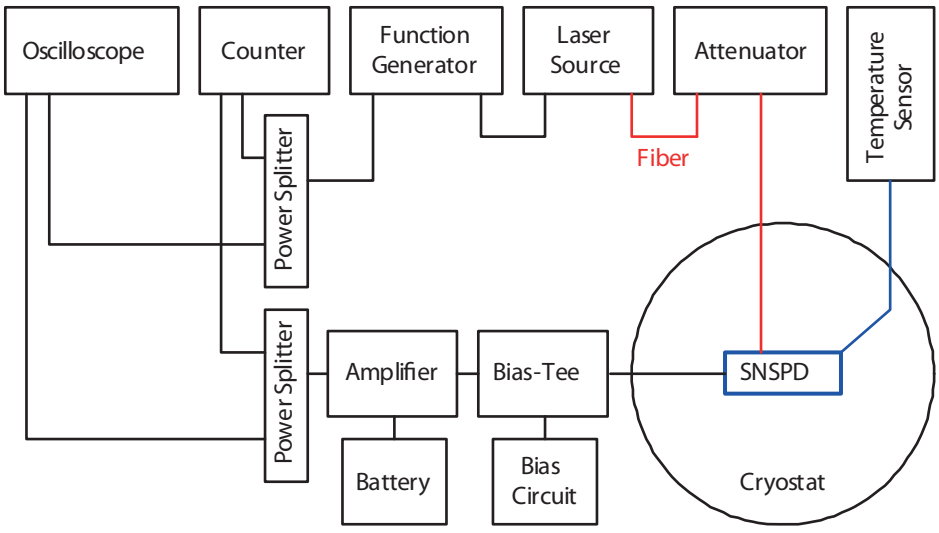

Figure 2.3: Schematics of the experimental characterization setup.

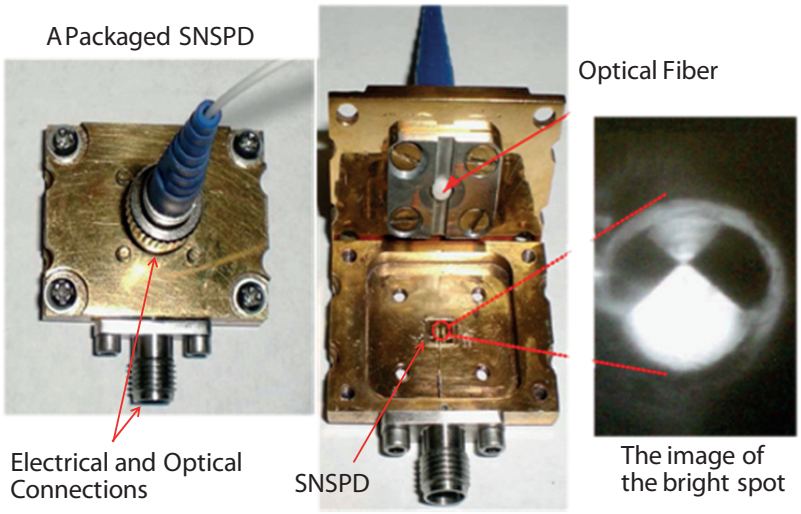

Figure 2.4: A packaged SNSPD, the internal structure of it and the bright spot seen under a microscope for doing optical alignments [66].

After doing the electrical connections and precise optical alignments, the finalized package is mounted inside a cryostat (Janis ST-500) as shown in Fig. 2.5. The bias is applied to the device using a 10MHz to 6GHz room temperature bias-Tee and a custom-made battery operated variable voltage source with about 4KΩ output resistance. The weak RF signal from the bias-Tee is amplified using a 40dB fast pulse 10KHz to 1.5GHz battery powered preamplifier. For monitoring purposes and doing timing measurements we used a 50G sample per second with 16GHz analog bandwidth digital oscilloscope. Statistical measurements of the output pulses form the SNSPD are done using a digitally adjustable counter with a DC to 300MHz analogue input bandwidth. The light source is a fiber coupled 1310nm distributed feedback laser diode with a 300ps pulse duration and 10MHz pulse repetition rate. For attenuating the laser pulses to the desired levels we exploited a digitally variable calibrated attenuator with maximum attenuation of 100dB. The single mode fibers used in the setup were spatially fixed to avoid unwanted polarization changes during measurements. During the experiment, the temperature of the package of SNSPD was monitored to be about 4K. By careful selection of a set of shielding, filtering and grounding techniques the whole setup was optimized to meet the required electromagnetic

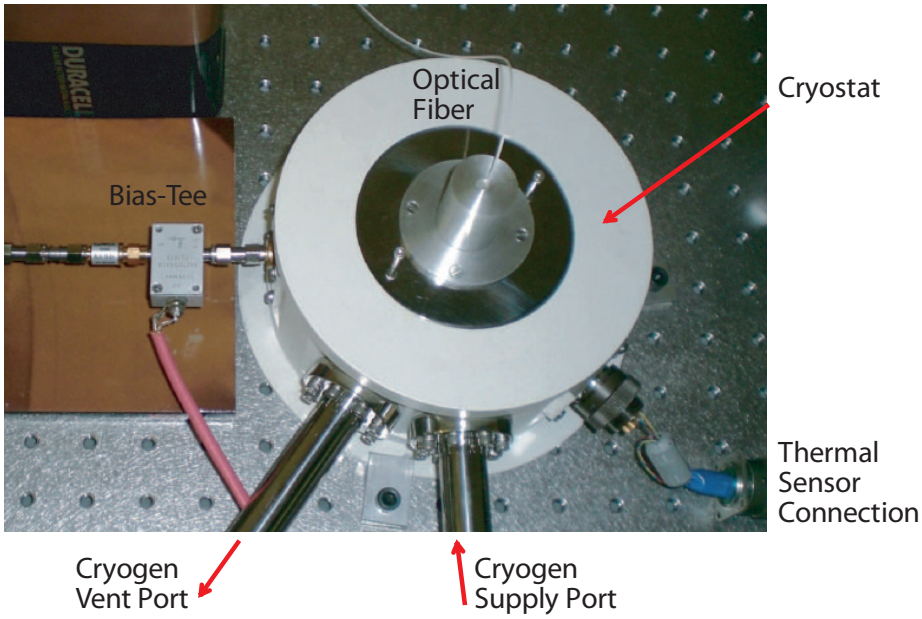

Figure 2.5: The cryostat installed on an optical table with its cryogen, optical and electrical connections.

compatibility performance. Fig. 2.6 shows the picture of the total setup.

2.3 Measuring the Parameters

We start determining the parameters of the model from different optical losses. The range of α_1 which is the manually added optical loss is known from the specifications of the variable optical attenuator to be between -1dB to -100dB. The coupling loss α_2 for the present setup can be experimentally determined. The value would be equal to -19dB as reported in [66] for this setup. The loss due to limited absorption of superconducting strips is known from electromagnetic simulations to be about -5dB at our wavelength of interest [48]. The specifications of the laser can be used to calculate N_{SP} equal to about 2×10^6 photons per pulse and t_S equal to 300ps. We will always use a repetition rate equal to 10MHz in the measurements. As a crude approximation of the dead time, we take the

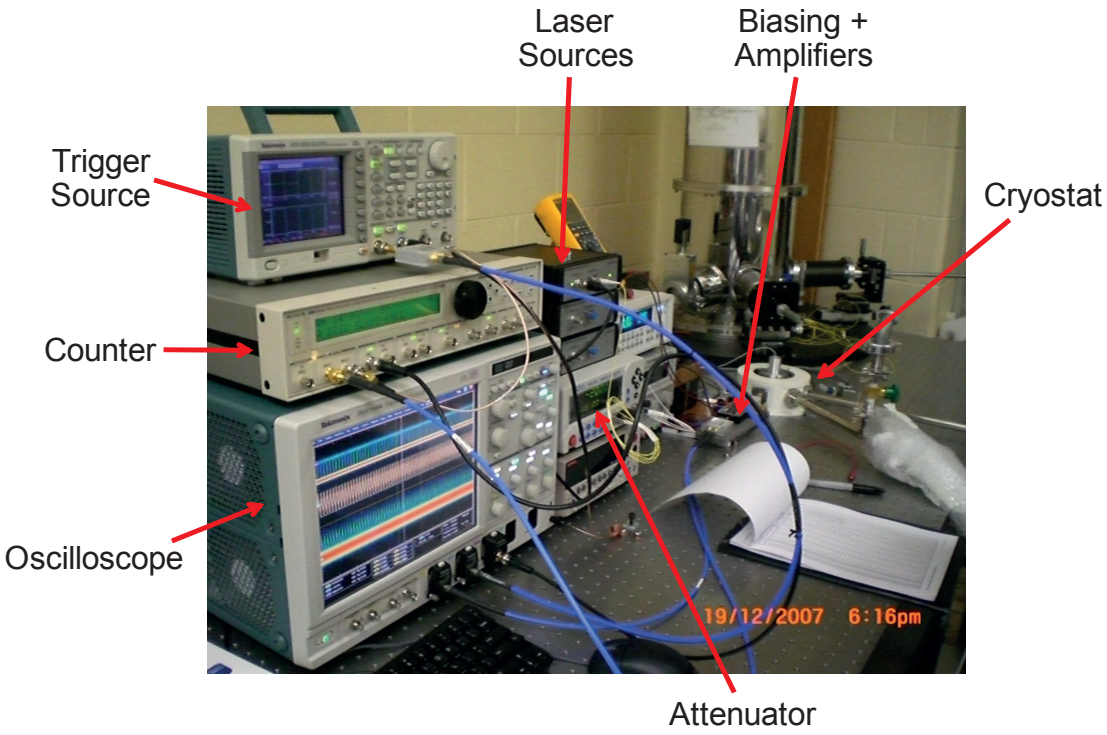

Figure 2.6: The picture of the total experimental setup.

sum of rise and fall time of the detector. The detector response that is similar to what is illustrated in Fig. 1.1 (b), gives this value equal to 13ns for our setup. To determine the perturbation or hotspot lifetime τ_h, we refer to the experiment done by Zhang et al. [68]. The experiment in this work shows 65ps measured average delay between the absorption of photons by the superconducting strips and the generation of electric pulses. Paying attention to the discussion following Eq. (2.25), we conclude τ_h should be approximately equal to twice of this value. Table 2.1 summarizes all of these parameters.

We determine the resistive barrier generation rates by using our experimental setup. A set of average total count rates versus the attenuation of the variable attenuator at different bias current ratios are measured. Having the measured points and also the model parameters listed in table 2.1, we use a fitting algorithm to extract the unknown G_m values from the measured points. The equations of the wide laser pulse were used in current

Parameter	Description	Value
α_1	Variable attenuation	-100dB to -1dB
α_2	Coupling loss	-19dB
α_3	Absorption loss	-5dB
τ_h	Hotspot life time	130ps
τ_{dt}	Detector dead time	13ns
F_S	Laser frequency	10MHz
t_S	Laser pulse width	300ps
N_{SP}	Number of photons per laser pulse	2×10^6

Table 2.1: The previously known parameters of the model. dB values are calculated as $10\log(\alpha_i)$.

calculations. Fig. 2.7 illustrates both of the measured points and the curves that are the outcomes of the model. We pay attention that at higher bias currents and at high enough optical intensities, there is a region where the slope of the curves are equal to one, i.e. a linear relation between the average number of photons per laser pulse and the count rate exists. This is reasonable because the average number of photons that excite the device changes linearly with the attenuation and the detector as a SPD is sensitive to each of these excitations. So the total count rate should also change linearly. This observation proves the detector is truly a single photon detector. Table 2.2 is the list of extracted G_m values. The last column shows the Root Mean Square Error (RMSE) of the fitting result. The empty cells that are marked by a dash represent those G_m values that are at least 50dB less than the corresponding G_{m-1} value. The values of these cells cannot be determined accurately because of their negligibly small effect on the total count rate of the device. Paying attention to the reasoning that led to Eq. 2.2, the reduction in the effect of G_m is expected and we can safely neglect the presence of these G_m values in the calculation of the total count rate of the device.

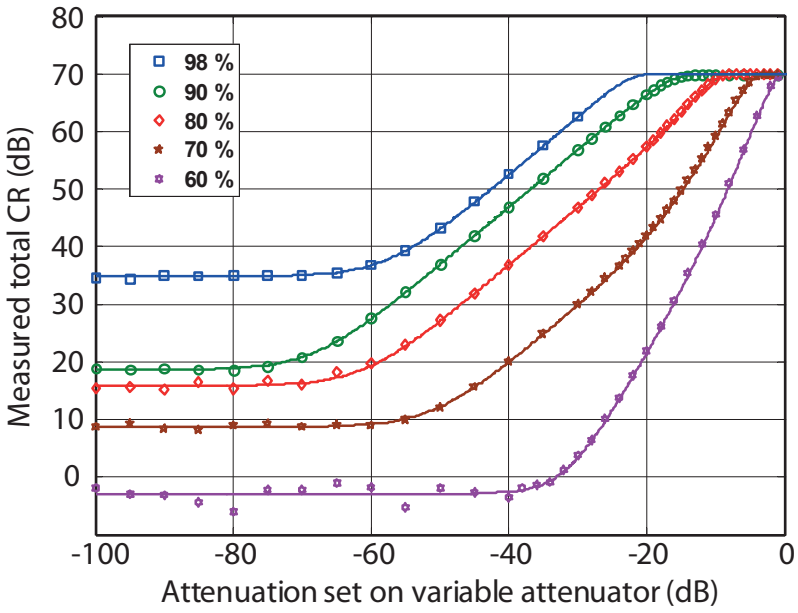

Figure 2.7: The points are the measured CR_t values versus attenuation of the variable attenuator at different bias current ratios. The curves are the results obtained with the equations of the wide pulsed laser approximation of our model.

$I_B/I_C(\%)$	G_0(dB)	G_1(dB)	G_2(dB)	G_3(dB)	G_4(dB)	G_5(dB)	RMSE
98	34.8	82.2	71.2	-	-	-	0.18
90	18.6	76.7	56.6	-	-	-	0.1
80	15.8	66.6	46.2	23.6	-	-	0.27
70	8.7	49.4	34.9	8.3	-19.1	-	0.17
60	-3.0	16.2	18.2	-0.5	-29.3	-	0.9

Table 2.2: The parameters of the model that were extracted from the measured points. dB values are calculated as $10\log(G_m)$.

2.4 Discussions

2.4.1 The Concept of G_m Set

G_0 values are equal to the corresponding measured count rates at very high attenuations which are essentially the values of dark count rates. This can be seen by comparing the G_0 values from table 2.2 with the count rates at -100dB that are illustrated in Fig. 2.7. Paying attention to Eq. (2.20), we note that this is true in all of the present cases because $G_0\tau_{dt}$ values are always much less than one.

To further discuss about the concept of G_1 we do a manual calculation on CR_t for our setup when α_1 is set to -39dB and bias current ratio is set to 90%. The average number of perturbations or hotspots generated per laser pulse can be calculated to be $2 \times 10^6 \times 10^{(-3.9-1.9-0.5)} = 1$. This shows each laser pulse makes one hotspot on the meander line in average. Because each hotspot lasts for 130ps and the laser makes 10^7 pulses per second, we can calculate $130 \times 10^{-12} \times 10^7 = 1.3$ms for the total time of one hotspot presence on the meander line per second. Referring to table 2.2, we can conclude in each one second period, for 1.3ms the SNSPD is generating pulses with a rate equal to $10^{7.67}$ and for the rest of the time it is generating pulses with a rate equal to $10^{1.86}$. The total count rate can thus be calculated to be $1.3 \times 10^{-3} \times 10^{7.67} = 47.8$dB which is exactly the value that can be read form Fig. 2.7. We note that the same numerical result can be obtained by using equations (2.11), (2.12) and (2.14). Here we intentionally did the calculations without using the developed formulas to emphasize on the physical concepts of the parameters of the model.

Similar manual calculations can be done for all of the points of the CR_t curves where just one dominant detection mechanism exist. This is true even for the points where the detector is in its nonlinear operation mode. For example at $\alpha_1 = -10$dB and when bias current ratio is set to 60%, the slope of CR_t versus attenuation curve suggests a dominant triple photon detection mechanism. Under these conditions and using Eq. (2.11), the average number of simultaneously active hotspots per laser pulse would be equal to 345. There are 6784540 possible ways for selecting 3 hotspots out of 345 hotspots and according to table 2.2, each selection has a resistive barrier generation rate equal to $10^{-0.05}$. On

the other hand the total time that the superconducting strips are excited by the laser pulses per second is 300ps× 10MHz= 3ms. By multiplying all of these factors we get $CR_t = 6784540 \times 10^{-0.05} \times 3 \times 10^{-3} = 43$dB which is again the measured value shown in Fig. 2.7. The presented examples clarify how each of the G_m values characterizes a certain photodetection mechanism of the superconducting strips.

2.4.2 Calculation of Quantum Efficiency

Equation (2.23) should be used to calculate the quantum efficiency. It gives a QE equal to 0.68% for 98% of bias current ratio and at a high attenuation of −60dB. For the present case it is also possible to calculate QE by directly using the measured points of Fig. 2.7 and exploiting the definition of QE that is written in Eq. (2.21). It is also possible to do this direct calculation for the highly nonlinear cases like when the bias current ratio is set to 60%. But the result would be some value that is certainly not describing the linear quantum efficiency of a single photon detector. By using the first term of the either of the equations (2.22), (2.23) or (2.24), we can define the linear quantum efficiency of the SNSPD as

$$QE_{Linear} \simeq 10^{\frac{\alpha_3}{10}} G_1 \tau_h \tag{2.29}$$

Equation (2.29) truly describes the single photon detection efficiency of the detector even when most of the measurable counts are due to the other nonlinear processes. So the G_1 column of table 2.2 together with the knowledge of α_3 and τ_h instantly gives the linear quantum efficiency of the detector for all of the bias current ratios.

It is possible to increase the quantum efficiency by exploiting optical structures that enhance the photoabsorption of the superconducting strips. In the same time, changing the parameters like the superconducting material, the film thickness, the material of the substrate and the operation temperature can potentially lead to a change in linear quantum efficiency by changing G_1 and τ_h.

2.4.3 Photon Number Resolution

Because all of the G_m values are essentially different rates with the same unit, they can be directly compared to each other. Fig. 2.8 is a plot of the measured G_m set versus bias current ratios that provides immediate information of the relative performance of each detection mechanism at different bias current ratios. When two simultaneous perturbations or hotspots are present on the superconducting strips two different mechanisms of G_1 and G_2 can generate resistive barriers. At high bias current where G_1 is dominant, photon number resolution can probably be achieved by the study of other parameters like pulse amplitudes. On the other hand, at lower bias currents where G_2 has the dominant effect, the detector has little response to two spatially separated hotspots. Under this condition, each pulse from the detector can be due to the presence of two spatially and temporally close photons. We believe by operating properly designed detectors in suitable conditions, this type of spatially resolved photon number counting can be achieved over a wider range of photon numbers.

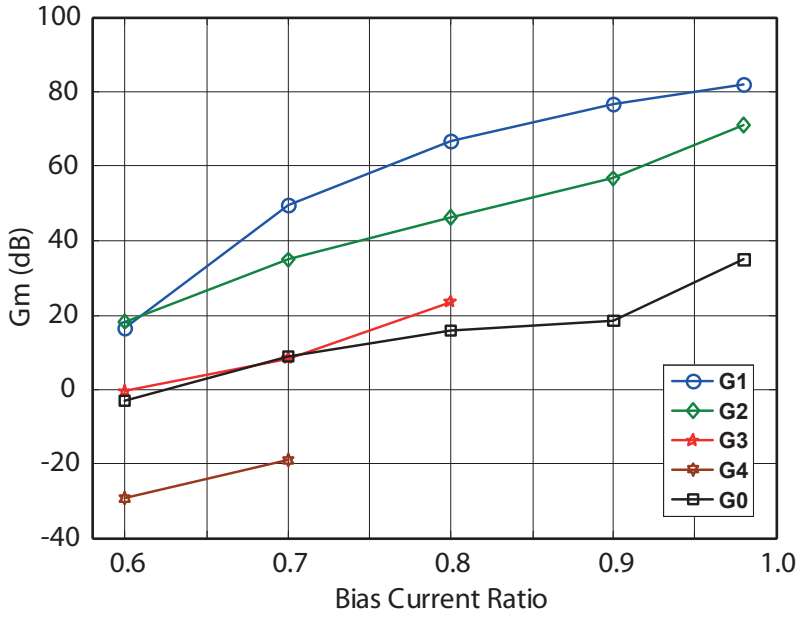

Figure 2.8: The measured resistive barrier generation rates versus bias current ratios.

2.4.4 Timing of the Detector

We use Eq. (2.28) to calculate the average delay of resistive barrier generation. The solid and fine dashed lines in Fig. 2.9 show the results of calculation with the G_m set from table 2.2 for 90% and 60% of bias current ratios. The measurement points reported in [68] are also depicted on the same figure. As can be seen, for 90% bias current ratio the agreement between the calculations and the measurements is good but this is not the case for 60%. Referring to the CR_t versus attenuation measurements reported for the same device in [68], we noted that there is no significant effect of G_3 and G_4 for that device. In an attempt to make G_m set of our SNSPD more similar to the one used in [68], we set G_3 and G_4 to be zero. The result is the coarse dashed line in Fig. 2.9 which is in better agreement with the measured points.

A systematic error between the model results and measured points can be seen at higher number of incident photons per pulse per device area. Equation (2.27) can also be used to do the same calculation with the recent G_m set. The result is the solid lines that

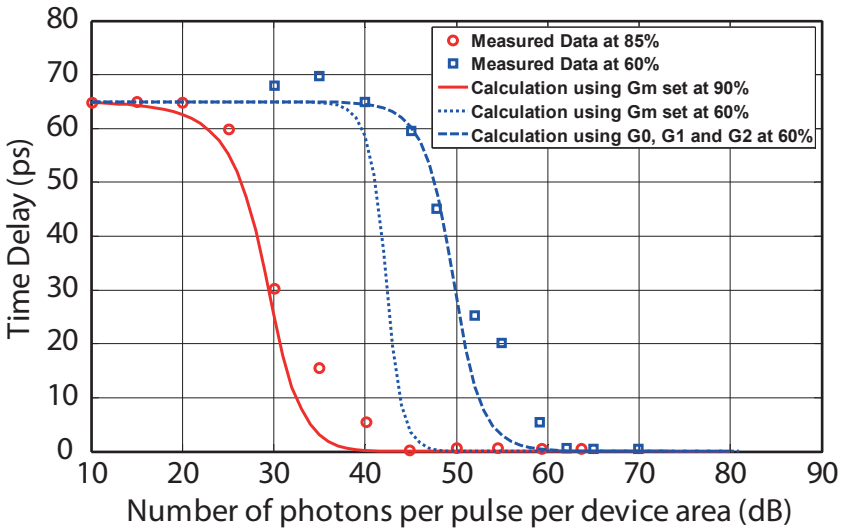

Figure 2.9: The delay time between absorption of photons by meander line and electric pulse generation. The points are the measurements reported in [68] and curves are the calculations based on Eq. (2.28).

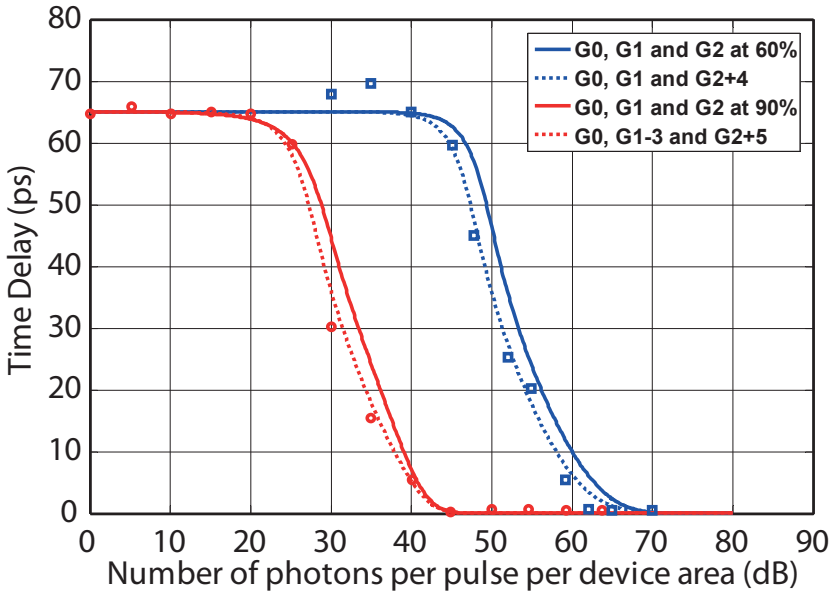

Figure 2.10: The delay time between absorption of photons by meander line and electric pulse generation. The points are the measurements reported in [68] and curves are the calculations based on Eq. (2.27).

are illustrated in Fig. 2.10. We used τ_σ (τ_σ^2 is the variance of the jitter profile as defined in Eq. (2.25)) equal to 19ps for making the similarity between the measurements and the calculations as close as possible. The resulting curves are so sensitive to the selected τ_σ and even slight changes in it can change the general shape of the curves. Fig. 2.10 shows good agreement between the measurements and calculations. To check whether mathematical structure of Eq. (2.27) allows better fit with the measured points or not, we slightly changed the used G_m set. The changes are written in the legend of Fig. 2.10 and the resulting curves are the dashed lines on the same figure. A final conclusion requires more experimental data over wider operating conditions. But we believe the results of Fig. 2.10 which shows the capability of the model to justify a rather complicated mathematical curve, proves the correctness of our modeling approach and its associated concepts.

2.5 Conclusions

In summary, a model for superconducting nanowire single photon detectors has been proposed. The model was developed and investigated by experiments, and a good agreement with the measurements was found. With parameters that describe the statistical operation of SNSPDs independent of the statistics of the light source, the model is able to quantify both the linear and nonlinear operation of these devices. Furthermore, the model introduces the concept of resistive barrier generation rates and provides a way to quantitatively study the effect of the presence of perturbations or hotspots on the meander line and their interactions. We also tried to justify the statistical photodetection concepts of the model by comparing the measurements of the average time delay of resistive barrier generation with the outcome of the model.

Chapter 3

Nonlinearity in Single Photon Detection and Detector Tomography

The semi-empirical model as presented in previous chapter was developed in the early stages of this PhD work. It translates the results of experiments into some useful parameters. The parameters are especially useful for quantifying nonlinearity in single photon detection. The work could be continued from two different perspectives.

First, the connection of some of the parameters with physical parameters of the device are unknown. Looking at the list of parameters and also paying attention to the materials of the introductory section 1.2, we conclude all physical connections are at present known except Generation Rates and timing parameters that are defined in Eq. (2.25). These are all the parameters used to model photodetection mechanism and dark counts. Having such connection would ideally be useful for designing SNSPDs with superior performance. This is a complex and nice problem of physics. But we believe the final results wouldn't be of much importance from a practical point of view. That is because: the timing parameters (τ_σ and τ_h) are already small enough for most of the applications; dark counts are small and also function of details of fabrication and cryogenic operation; the most important generation rate, i.e. G_1, in the end translates to intrinsic efficiency of the detector and from experiments it is known this efficiency is nearly at 100% for a high quality detector operated appropriately [56]. Alternatively, the parameters can also be determined and

optimized experimentally which is good because it will include all details of fabrication and operation as well. These points suggest there is little practical motivation to work out such hard problem.

Second, our semi-empirical model should have a connection to a quantum optical model, i.e. something similar to what is shown on Fig. 3.1. This is a broadly used model to describe linear single photon detectors. It models the quantum efficiency of a typical SPD as losses of a fictitious beam splitter. The power of such model lies in its simplicity and generality. It is simple because its only parameter, P_1 can experimentally be determined by readily available optical excitations like some coherent state probes from a laser. It is general because it applies to all SPDs. Also, it is general because it gives the Positive Operator-Valued Measure (POVM[1]) of the detector from which the response of the detector to an arbitrary optical input state can be calculated. In fact, Fig. 3.1 sets a mathematical standard the outcome of all the experiments should be compared with. These features help such model to serve as an interface between both "theory and experiment" and also between "SPD development and SPD applications". However, we couldn't find a quantum optical model that incorporates the possibility of having nonlinearity in single photon detection, a feature that was included in our semi-empirical model.

In this chapter, we improve our previous model that was only valid for coherent state at the input to a quantum optical version. A more comprehensive quantum optical model like the one described above for linear SPDs come out of the results. We find the POVM that this model describes and explore its correctness by comparing it with what is found from a completely different approach, i.e. detector tomography. The most important results of this work have been published in [69, 70]. This work has been done by collaboration with Dr. Jeff Lundeen from National Research Council of Canada (NRC).

[1] An state can be represented by a density matrix ρ and a measurement by a set of operators (POVMs) $\{\Pi_i\}$ in quantum physics. A measurement on state ρ would result in the j_{th} output with the probability $Tr(\rho\Pi_{i=j})$.

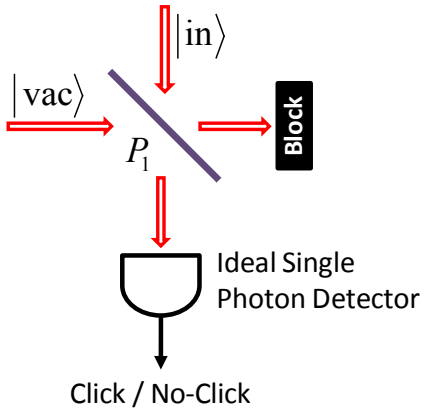

Figure 3.1: A broadly used quantum optical model for single photon detectors. The quantum efficiency is modeled as losses of a fictitious beam splitter.

3.1 Quantum Optical version of the Semi-empirical model - Narrow Pulses

Assume the optical input to our SNSPD is in a general state $|\Psi_{in}\rangle$ expressed in number basis as

$$|\Psi_{in}\rangle = \sum_{n=1}^{\infty} \Psi_{in}(n) \, |n\rangle_{in} \, . \tag{3.1}$$

Also assume the photons are generated by a pulsed source and are such confined in time that our conditions for narrow laser pulses, i.e Eq. (2.15) holds. The SNSPD that is installed in a setup like what is shown in Fig. 2.3 can make a click upon this excitaion. The question is what would be the click probability, $P_{click}(|\Psi_{in}\rangle)$ in a time interval equal to τ_h after the optical excitation.

We can treat all the optical losses between incoming photons and the hotspots that are generated on superconducting nanowires as η. This has the following relation with our previous loss parameters defined in Eq. (2.3).

$$\eta = 10^{\left(\frac{\alpha_2 + \alpha_3}{10}\right)} \tag{3.2}$$

We model η by a fictitious beam splitter as done in the standard model depicted in Fig. (3.1) [71]. Writing down the math, the probability of having exactly n_h hotspots generated on the nanowires will be

$$P(n_h) = \sum_{p=0}^{\infty} |\Psi_{in}(n_h + p)|^2 \binom{n_h + p}{p} \eta^{n_h} (1-\eta)^p. \tag{3.3}$$

Therefore, with a probability equal to $P(n_h)$, the resistive barrier generation rate during a time interval equal to τ_h after photoabsorption will be $GR(n_h)$ as given by Eq. (2.1). This generation rate is converted to a count rate according to Eq. (2.6) or its narrow pulse equivalent Eq. (2.18), repeated here for convenience. [2]

$$CR_t(t, n_h) = \begin{cases} GR(n_h)\ \exp\left(-GR(n_h)\ t\right) & 0 \le t \le \tau_h \\ \dfrac{G_0}{1 + G_0 \tau_{dt}} & Otherwise \end{cases} \tag{3.4}$$

The integral of this function over τ_h is the click probability if the number of hotspots is equal to n_h. This is in fact the coefficient of F_S in Eq. (2.19).

$$P_{click}(n_h) = 1 - \exp\left(-GR(n_h)\tau_h\right) \tag{3.5}$$

[2] We have found a mathematical issue in our semi-empirical formalism when trying to write down its POVM. This is with in Eq. (2.5) in which we average all nonlinearities into a total generation rate function and then the average undergoes another nonlinear transformation by Eq. (2.6). This is while the reverse is correct, i.e. each generation rate that might happen with a certain probability should pass through the nonlinearity of Eq. (2.6) and then the result should be averaged to yield a total count rate. The error is only significant when the integral in Eq. (2.6) becomes significant compared to 1, or equivalently only when the count rate is close to its saturation at high input photon intensities. Assuming we need to be $10dB$ apart from the saturation level for keeping the absolute validity of the semi-empirical model, and also looking at the results of figures. 2.7 and 2.9; we conclude the results of previous chapter are still valid for most of range of the curves. However, having the problem discovered, in this section we present the corrected equations. This is why in contrast with Eq. (2.18), here $CR_t(t)$ is replaced by $CR_t(t, n_h)$.

Equation (3.5) is an important relation that when combined with Eq. (2.1) gives:

$$P_{click}(n_h) = 1 - \exp\left(-\sum_{m=0}^{M-1} \binom{n_h}{m} G_m \tau_h\right) = 1 - \prod_{m=0}^{M-1} (1 - P_m)^{\binom{n_h}{m}}, \tag{3.6}$$

where P_m is defined by

$$P_m \equiv 1 - \exp\left(-G_m \tau_h\right)\cdot \tag{3.7}$$

Having $P_{click}(n_h)$ determined, we can write down the total click probability as

$$P_{click}(|\Psi_{in}\rangle) = \sum_{n_h=0}^{\infty} P(n_h) P_{click}(n_h) = 1 - \sum_{n_h=0}^{\infty} P(n_h) \prod_{m=0}^{M-1} (1 - P_m)^{\binom{n_h}{m}}. \tag{3.8}$$

Finally, combining Eq. (3.8) and Eq. (3.3) yields

$$\begin{cases} P_{click}(|\Psi_{in}\rangle) = 1 - \displaystyle\sum_{n_h=0}^{\infty} \sum_{p=0}^{\infty} |\Psi_{in}(n_h + p)|^2 \binom{n_h + p}{p} \eta^{n_h} (1 - \eta)^p \prod_{m=0}^{M-1} (1 - P_m)^{\binom{n_h}{m}} \\ P_{no\ click}(|\Psi_{in}\rangle) = 1 - P_{click}(|\Psi_{in}\rangle) \end{cases} \tag{3.9}$$

This completes the mathematics for finding the click probability of our semi-empirical model for a general state at the detector input. However we further develop the result for two important quantum states at the input.

First, for the number state $|\Psi_{in}\rangle = |N\rangle$. In this case plugging $|\Psi_{in}| = \delta_{n,N}$ into Eq. (3.9) and doing the math, we get

$$\begin{cases} P_{click}(|N\rangle) = 1 - \displaystyle\sum_{n_h=0}^{N} \binom{N}{n_h} \eta^{n_h} (1 - \eta)^{N - n_h} \prod_{m=0}^{M-1} (1 - P_m)^{\binom{n_h}{m}} \\ P_{no\ click}(|N\rangle) = 1 - P_{click}(|N\rangle) \end{cases} \tag{3.10}$$

Second, for coherent state $|\Psi_{in}\rangle = |\alpha\rangle$, i.e. when the input is in coherent state with the mean number of photons $\langle n\rangle = |\alpha|^2$. In this case plugging the Poissonian distribution into Eq. (3.9) and doing the math, we get

$$\begin{cases} P_{click}(|\alpha\rangle) = 1 - \sum_{n_h=0}^{\infty} \exp\left(-\eta|\alpha|^2\right) \frac{\left(\eta\,|\alpha|\right)^{2n_h}}{n_h!} \prod_{m=0}^{M-1} (1 - P_m)^{\binom{n_h}{m}} \\ P_{no\ click}(|\alpha\rangle) = 1 - P_{click}(|\alpha\rangle) \end{cases} \tag{3.11}$$

Although Eq. (3.7) determines the connection of P_m to our generation rates for the special case of narrow pulses, the P_m set has a strong physical significance by itself. This would be more clear in the next section.

3.2 Model for Nonlinear Single Photon Detectors

Single photon detectors (SPD) are binary detectors ('Click', or 'No Click'), and thus any non-zero number of detected photons will result in the same response: a Click. This behaviour, first directly tested in Ref. [72], is now contained within the standard model for the SPDs as shown in Fig. 3.1. This is a perfectly linear model and the positive operator-valued measure (POVM) described by it is

$$\begin{cases} No\ Click:\ \pi_0^{SPD} = \sum_{n=0}^{\infty} (1 - P_1)^n\, |n\rangle\, \langle n| \\ Click:\ \pi_1^{SPD} = 1 - \pi_0^{SPD} \end{cases} \tag{3.12}$$

where P_1 is the quantum efficiency, $|n\rangle$ is an n-photon state. This simple model neglects the optical or electrical nonlinearities that likely exist, to some degree, in all SPDs. Indeed, the form of the click probability suggested by Eq. (3.9) confirms for SNSPDs the POVM of Eq. (3.12) is not generally applicable.

In this section, we try to find a form of POVM that is compatible with our findings in previous section. The new POVM can replace that of Eq. (3.12) for SNSPDs and possibly for other SPDs that include nonlinearities.

Consider a binary detector that is only sensitive to n number of photons; any less and the detector responds with No Click, any more and it still only outputs one Click. This is the n-photon generalization of the SPD and, hence, we call it an n-photon detector (NPD). If $m > n$ photons impinge on the detector, there are m choose n ways for those m photons to trigger the NPD. Consequently the generalization of Eq. (3.12) is:

$$\begin{cases} No\ Click: \ \pi_0^{NPD} = \sum_{m=0}^{\infty} (1 - P_n)^{\binom{m}{n}} |m\rangle \langle m| \\ Click: \ \pi_1^{NPD} = 1 - \pi_0^{NPD} \end{cases} \tag{3.13}$$

where π_0^{NPD} is the No Click operator, P_n is the n-photon detection efficiency and $\binom{m}{n}$ is the binomial coefficient ($= 0$ for $n > m$, $= 1$ for $n = 0$). This generalization works even for a zero photon detector. We can identify P_0 as what is commonly called the 'dark count probability'.

A nonlinear SPD can be modeled as concurrent NPDs. As shown in Fig. 3.2, the model consists of a logical OR between M NPDs, where M represents the maximum number of mechanisms that should be present in order to describe the response of the detector before it saturates at high intensities. The associated POVM operators are:

$$\begin{cases} No\ Click: \ \pi_0^{NL} = \sum_{m=0}^{\infty} \prod_{n=0}^{M-1} (1 - P_n)^{\binom{m}{n}} |m\rangle \langle m| \\ Click: \ \pi_1^{NL} = 1 - \pi_0^{NL} \end{cases} \tag{3.14}$$

This is basically the same as one suggested by Eq. (3.9), but with η set to one.

The loss parameter η as defined by Eq. (3.2) has a well defined physical origin. It can be added to the model described by Eq. (3.14) by adding a beam splitter in front of the nonlinear SPD. However, the other option is keeping η embedded in the nonlinear SPD that we are trying to describe. This changes the physical interpretation of the set of parameters $\{P_n\}$, but it keeps the simplicity and generality of Eq. (3.14). We'll experimentally investigate the effect of adding a loss η on the set $\{P_n\}$ later in this chapter.

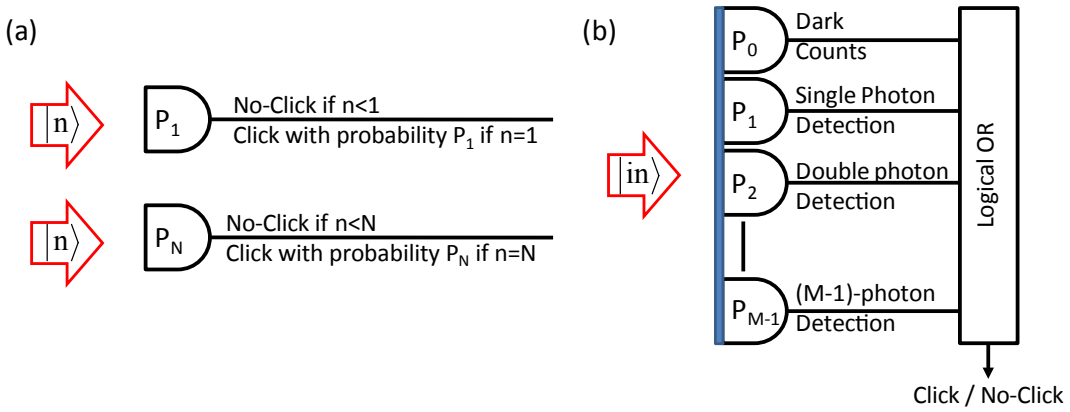

Figure 3.2: The Nonlinear Single Photon Detector model. Each element represents an n-Photon Detector. A broadly applicable model is created by logically ORing these elements.

Therefore, we now have Eq. (3.14) for the POVM of a nonlinear SPD. It is derived with minimum assumptions about the working of the detector, so we expect it to be quite general. However, there are two aspects that should be worked out.

First, we note that the only parameter of the standard SPD model, i.e. P_1 can be experimentally determined by measuring click probability of the detector to a highly attenuated laser pulse. But this is not straight forward for nonlinear model that incorporates many parameters. So a procedure for experimentally determining the model parameters $\{P_n\}$ should be developed. Second, the nonlinear model was both supported by the semi-empirical model and by its minimal underlying assumptions. But the proof of its correctness wouldn't be complete without comparing its POVM with the actual POVM that can be measured. We address both of these issues in the next two sections.

3.3 How to Measure the Parameters

Most of the characterization of SPDs are still done with coherent state probes due to widely available lasers with different specifications. We also seek to determine the parameters of or nonlinear model in Eq. (3.14) using some coherent state excitations.

For the standard SPD that is described by Eq. (3.12) and excited with coherent states $|\Psi_{in}\rangle = |\alpha\rangle$, the click probability would be $Tr(|\alpha\rangle\langle\alpha|\,\pi_1^{SPD})$, or equivalently the Q-function of the click POVM operator, π_1^{SPD}. Doing the math, this will have the following form,

$$Q^{SPD}(\alpha) = 1 - \exp\left(-P_1|\alpha|^2\right), \tag{3.15}$$

which approximates to $P_1|\alpha|^2$ for highly attenuated lasers. So, one can measure the P_1 with a single click probability measurement using a highly attenuated laser. However, following the same procedure for our generalized POVM of nonlinear SPDs in Eq. (3.14) we get the following from for the click probability in response to $|\alpha\rangle$

$$Q^{NL}(\alpha) = 1 - \sum_{m=0}^{\infty} \mathrm{e}^{-|\alpha|^2} \frac{|\alpha|^{2m}}{m!} \prod_{n=0}^{M-1} (1 - P_n)^{\binom{m}{n}}. \tag{3.16}$$

This incorporates many parameters, and thus contrary to the previous case, the parameters can not be easily determined with a single point measurement.

To find $\{P_n\}$, we use coherent states with different amplitudes, α. We sequentially send R_T copies of this state into the SNSPD system and record the number of detector Clicks, R_1. This is repeated for a set of D states $\{|\,\alpha_i\rangle\}$, increasing α from $\alpha_0 = 0$ until the detector response is unchanging at α_D. i.e. $\partial R_1/\partial\alpha = 0$. The estimated Click probability, R_1/R_T, is equal to the Q-function of the Click POVM operator, $Q\,(\alpha)$. The measured $Q(\alpha)$ is set equal to the theoretical one $Q^{NL}(\alpha)$, from which $\{P_n\}$ should be determined.

To work out this mathematical problem, we rewire the Eq. (3.16) in matrix form as:

$$C = F\Pi = F\,(E - \exp\,(GH))\,, \tag{3.17}$$

where C (with dimensions $D \times 1$), includes the D measured statistics, R_1/R_T; Π $(N \times 1)$ includes the diagonal elements of π_1^{NL}; F contains the D coherent state probes, $F_{i,j} = |\alpha_i|^{2j}\exp\left(-|\alpha_i|^2\right)/j!$; E is a matrix of ones; G is a matrix of binomial coefficients such that $G_{i,j} = \binom{j-1}{i-1}$; and H $(M \times 1)$ is an unknown matrix which includes the unknown set $\{P_n\}$, $H_{i,1} = \ln(1 - P_{n=i-1})$. Note, since our detector lacks phase sensitivity, the off-diagonal

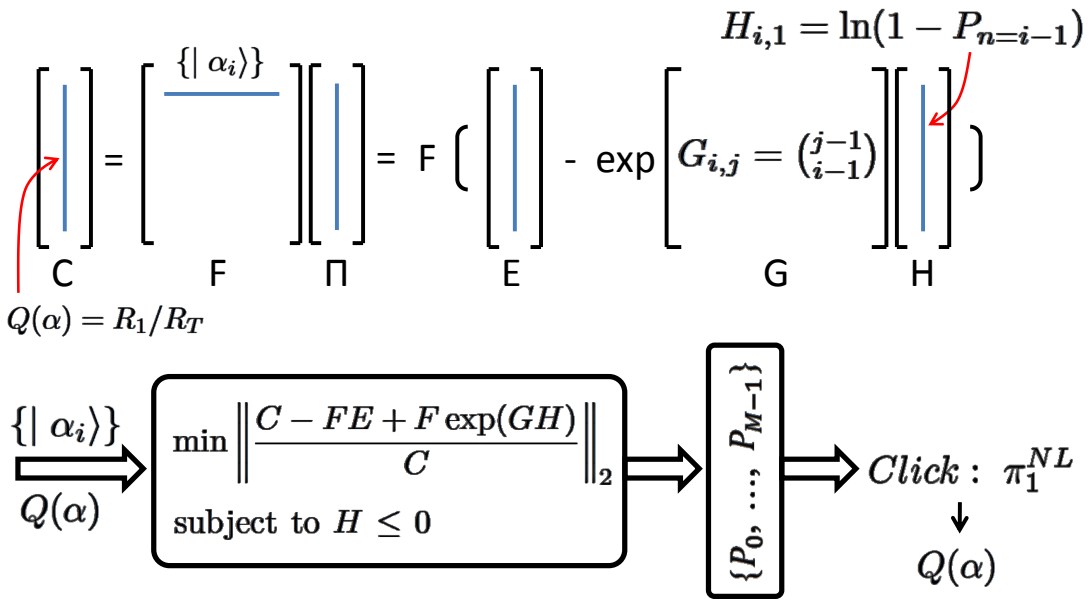

Figure 3.3: An schematics of the procedure for experimental determination of the set $\{P_n\}$. The measured Q-function, $Q(\alpha)$, is the input to the problem and the optimization results in the unknown set of parameters $\{P_n\}$, from which the POVMs can be determined.

elements of the click operator are zero. We thus have represented it as a vector Π which is truncated at a number state $N-1$ that is sufficiently high that $\Pi(N) \approx 1$. Figure 3.3 is an illustration of the different matrixes.

We estimate the matrix of unknowns, H by solving the following constrained nonlinear multivariable optimization problem:

$$\begin{aligned} &\min \left\| \frac{C - FE + F\exp(GH)}{C} \right\|_2 \\ &\textit{subject to } H \leq 0 \end{aligned} \tag{3.18}$$

The second norm of a matrix is defined as $\|A\|_2 = \left(\sum_{i,j} |A_{i,j}|^2\right)^{1/2}$. Each element of the expression is normalized to C to give equal weighting to all the points. The constraint of

the problem ensures the optimization leads to a physical result for the set $\{P_n\}$. We note the function $\exp(\alpha x)$ is convex on $\mathbb{R}$ for any $\alpha \in \mathbb{R}$ [73]. So our optimization problem is also convex as it tries to minimize a linearly transformed convex function over a convex subset of $\mathbb{R}$. Therefore finding a local minimum is enough to conclude it is also the unique global minimum.

We note one of the unknowns of in Eq. (3.18) is the number of unknown parameters, M itself. This is equivalent to say the number of mechanisms needed to make the detector POVMs is unknown. To solve this problem, we set M to an arbitrary but large value and solve Eq. (3.18). From the estimated $\{P_n\}$ we only keep those elements that change the minimum of Eq. (3.18) by more than 1%.

3.4 Detector Tomography

We developed our model in Eq. (3.14) and established the methods needed for determining its parameters in the previous two sections. Although we tried to do the modeling with minimal assumptions, it is desirable to compare its POVM with the one determined from a different method, i.e Detector Tomography, to further check its validity.

From the other perspective, Detector Tomography [74, 75] is an agnostic procedure to determine the POVM of a detector. The detector is treated as a Black Box in that we do not need to know its mechanism or make ancillary assumptions about it. Just recently demonstrated in principle, Detector Tomography itself has yet to be applied to a detector without an accepted model for its POVM. The SNSPD with its nonlinear behaviors at lower bias currents seems to be a good candidate.

To perform tomography, we follow the same experiment that led to Eq. (3.17). The detector is excited with many copies of a set of coherent state probes, $\{|\ \alpha_i\rangle\}$ with properly chosen amplitudes to measure the Q-function of the Click POVM operator, $Q(\alpha)$. The results are put in matrix form $C = F\Pi$, exactly like Eq. (3.17). However, contrary to Eq. (3.17) where we used our model to write down the form of Π, Π is directly solved in detector tomography. Figure 3.4 is an illustration of this. Using the mentioned matrix form, one can write down the following convex quadratic optimization problem:

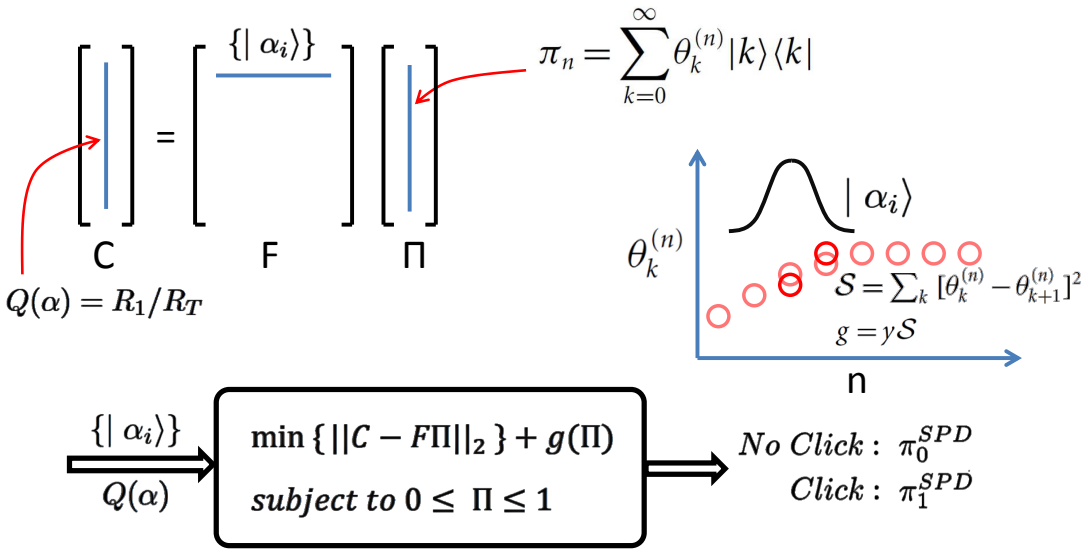

Figure 3.4: An schematics of the procedure for detector tomography. The measured Q-function, $Q(\alpha)$, is the input to the problem and the optimization directly results in the unknown POVMs. As depicted because the used coherent state probes are spread over many elements of a POVM, $\min \| C - F\Pi \|_2$ by itself is an ill-conditioned problem. So $g(\Pi)$ is added to the problem to ensure smoothness of the resulting POVMs. Details of this is well described in [76, 74].

$$\begin{aligned} &\min \| C - F\Pi \|_2 + g(\Pi) \\ &subject\ to\ 0 \leq \Pi \leq 1 \end{aligned} \tag{3.19}$$

where $g(\Pi)$ is a regulating function details of which was described in [76]. Of course the POVMs obtained using our model and the ones calculated by tomography should be in close agreement.

We note, the lack of ancillary assumptions and models in Detector Tomography make it general and objective. At the same time, it provides a surplus of information (i.e. $O(N)$ parameters) that can be difficult to interpret. Tomography can hardly replace the natural ease and intuition that is associated with a model, like our nonlinear SPD model.

We are now in a position to experimentally study the SNSPD in light of our model and also tomography. The next section is devoted to this.

3.5 Experiments and Discussions

The setup and SNSPD chip use used in this section is in general similar to the one already used section 2.2 for experimental study of our semi-empirical model. However there are some differences. Instead of using a continues flow cryostat as shown in Fig. 2.5, we installed the fiber packaged SNSPD in a cryogenic dipstick probe to cool the the device to 4.2K by immersing the probe in liquid helium. The advantages include much less cryogen consumption and more stable operation point. The mechanical details of this is reported in [77]. Also, we exploited a computer both to control generation of the set of coherent states $\{\alpha_i\}$, and record the number of detector clicks R_1 automatically. Finally, we used a 20ns counting gate, triggered by the laser, to reduce the dark count contribution from the times between input pulses. Figure 3.5 shows an schematic of the setup.

We set the number of copies per coherent state, R_T, equal to 10^5, and measure Q-function by the procedure described before Eq. (3.17). This is done at three bias currents, 25, 20 and 16μA. In Fig. 3.6, we plot the measured response for each of these (blue circles). We expect a standard linear SPD response at 25μA since this is the normal operation mode. Using Eq. (3.15) for ideally linear SPDs, we estimate P_1 using a single data point at $Q(\alpha) = R_1/R_T = 0.1$. Indeed, using this P_1, the resulting predicted response (red line) agrees well with the measured response. Repeating this analysis for 20 and 16μA, we find that the estimated P_1s, and thus, quantum efficiencies decrease as the bias current decreases. More significantly, the disagreement between the shape of the predicted and measured Click Probability distributions is substantial. Evidently, a SNSPD quickly becomes nonlinear as the bias current is lowered.

We now solve Eq. (3.19) to find Π. However, our particular SNSPD setup have low system quantum efficiency (0.2% or less at 1310nm at a maximum bias current of 25μA) and thus the maximum photon number, $N-1$, required to span its response was large. This is different from the previous detector tomography reports on APDs in which the

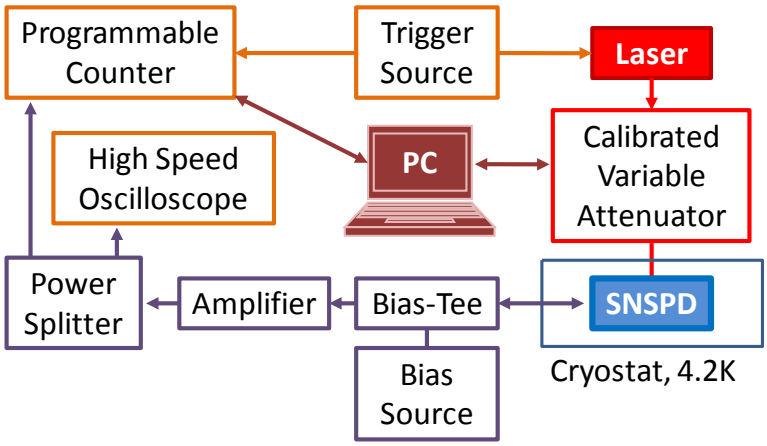

Figure 3.5: Schematics of the experimental setup. The set $\{\alpha_i\}$ is generated by exploiting a computer controlled variable optical attenuator and the click probabilities are measured using a programmable counter controlled by the same computer. The laser is 1310nm and produces 200ps pulses at 100KHz. The critical current of the SNSPD chip used in this setup was measured to be $26.0 \pm 0.5\mu$A at 4.2K.

higher system quantum efficiency made N small [76]. Large N means the fitting algorithm needs to find large number of unknowns ($\sim 10^5$ for 16μA) which is tedious. Instead of using large matrices in the fitting, we scaled the inputs $\{|\ \alpha_i\rangle\}$ by a factor $k \ll 1$. For each bias current, k is chosen so that the Click Probability is 95% at an average photon number $\langle n\rangle = 30$. This scaled data is shown in Fig. 3.7(a) (black circles). We plot Π determined from it (i.e. the diagonal elements of the scaled Click POVM operator) in Fig. 3.7(b) (blue circles). Using this Π, in Fig. 3.7(a) (blue line) we plot the predicted detector response to coherent input states. This fits the scaled data well, confirming the fitting procedure.

If scaled by too large a factor the POVM will, at the very least, be unrepresentative of the detector and, at worst, be physically impossible. Thus we test the estimated POVM for validity by adding k loss back into the POVM (i.e. $\Pi_{unscaled} = L^{-1}\Pi_{scaled}$, where L is the binomial distribution matrix described in [76]) and predicting the detector response to the original unscaled inputs, $\{|\ \alpha_i\rangle\}$. For all the bias currents, the difference between the predicted click probability and the raw data (i.e. $|R_1/R_T - \mathrm{Tr}[|\alpha_i\rangle\langle\alpha_i|\,\Pi_{unscaled}]|$) is

less than 0.15% on average and has a maximum of 1.4%. This indicates that we have accurately estimated the SNSPD POVM using the scaling technique.

We now turn our attention to our nonlinear SPD model and solve Eq. (3.18) for scaled input states. From the estimated $\{P_n\}$ we only keep those elements that change the minimum of Eq. (3.18) by more than 1% (25μA: $\{P_0,\ P_1\}$; 20μA: $\{P_0,\ \ldots\ ,\ P_4\}$; 16μA: $\{P_1,\ \ldots\ ,\ P_4\}$). These parameters classify the operation of the scaled SNSPD, from a standard SPD at 25μA to a composite of one, two, three, and four photon detectors at 16μA. From these $\{P_n\}$ we calculate the nonlinear SPD Click POVM operator for the three bias currents in Fig. 3.7(b) (black dotted line). They agree with the tomography POVMs to within 1% for most of the elements of Π. For 25μA and 20μA the maximum difference is

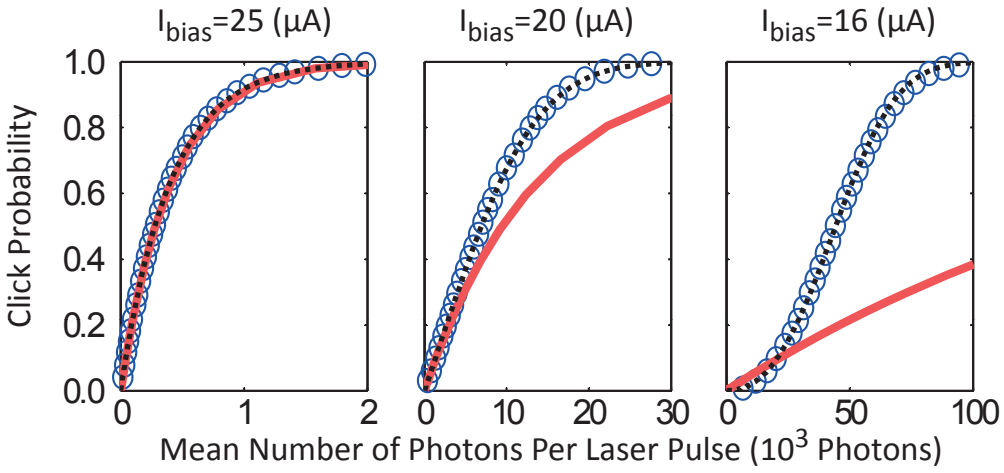

Figure 3.6: Click Probability at different bias currents. The critical current was measured to be $26.0 \pm 0.5\mu$A. The blue circles are measured Click probabilities (not all points are shown). The red lines are calculated using the linear model in Eq. (3.15) by calculating the efficiency parameter P_1 when the click probability is equal to 0.1. P_1 equals 2.44e-3, 7.3e-5, 4.87e-6 for 25, 20, and 16μA, respectively. The black dotted lines are from the nonlinear SPD Model in Eq. (3.16). $\{P_n\}$ equals {7.30e-4, 2.49e-3}, {9.72e-6, 7.15e-5, 8.14e-9}, {0, 7.33e-8, 2.87e-10, 2.81e-14} for 25, 20, and 16μA, respectively. Zero values indicate they change the minimum of Eq. (3.18) by less than 1%.

3% at $\Pi(n=1)$ and 6% at $\Pi(n=3)$ for 16μA. This excludes the large error at $\Pi(n=0)$, which we attribute to insufficient measured statistics at extremely small mean photon numbers. The Quantum Fidelity (see [76] for a definition) of the model and tomography operators are above 99.8% for all three bias currents. Thus, the model successfully gives the POVM of the SNSPDs including their nonlinearity, but with a dramatic reduction in the number of parameters compared to tomography.

Contrary to tomography, the number of unknowns in the optimization problem of Eq. (3.18) doesn't increase for a detector with low quantum efficiency. Consequently, we can directly solve the problem for the unscaled detector as well. In Fig. 3.6, we plot the model's predicted response to the coherent state inputs, with parameters from the unscaled data (black dotted line). The difference with the measured statistics is less than 0.34% on average (i.e the minimum found in Eq. (3.18) divided by the number of points).

We can attribute the SNSPD nonlinearity to the fact that at lower bias currents the absorption of multiple photons in close proximity and within a short period of time can inject enough energy to switch the wire to normal state more efficiently than independent absorptions. This is indeed compatible with the early observations on SNSPDs [2]. Moreover, the capability of our nonlinear SPD model to reproduce the non-linearity of measured curves in Fig. 3.6 with few parameters (only P_2 at 20μA and P_2, P_3 at 16μA) reconfirms the detector includes some NPDs as its basic detection elements. This rules out the other possible justifications of the observed nonlinearities including heating effects at higher input photon flux.

Unlike the standard SPD, where $P_1 \rightarrow \eta P_1$ under a preceding optical loss of η, there is no analytic formulae for how $\{P_n\}$ transform under loss. By inspection of the scaled and non-scaled model fits (see Fig. 3.8), however, each element of $\{P_n\}$ that is significant approximately satisfies $\log(P_n(\frac{1}{k})) - \log(P_n(\frac{1}{k}=1)) = n\log(\frac{1}{k})$. Thus significant elements of $\{P_n\}$ scale as η^n. Consequently, removing any linear optical inefficiency from a nonlinear photon counter makes it more nonlinear. We also note that, as expected, P_0 of the scaled detector is almost the same as the one for non-scaled detector. This is expected as the dark count probability should is not dependent on the optical input as expected.

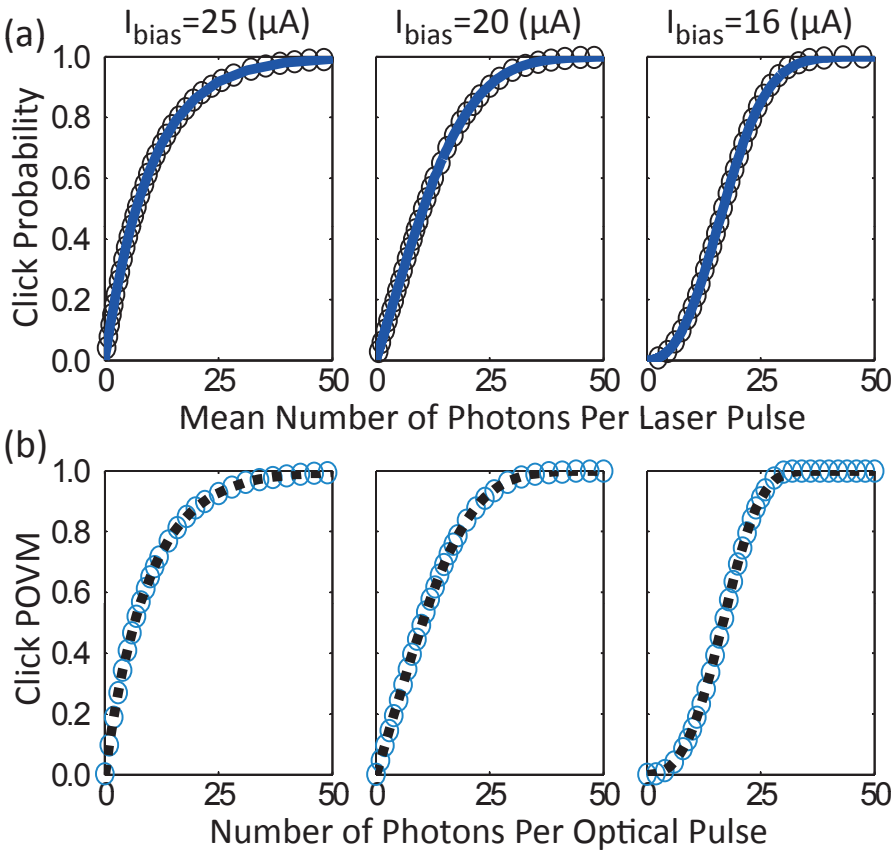

Figure 3.7: (a) The Q-function (i.e. click probability for coherent state inputs) of the scaled detector at different bias currents. The scaling factor (k) equals 0.025, 0.0015, 0.00037 for 25, 20, and 16μA, respectively. The raw scaled data (black circles) agrees well with the tomographic POVM (blue line). (b) The corresponding Click POVM operator. The operator found from tomography (blue circles) agrees with that from the nonlinear SPD Model (black dotted line). In the latter, $\{P_n\}$ equals {7.29e-4, 9.95e-2}, {1.08e-5, 4.76e-2, 3.74e-3, 1.13e-4}, {0, 1.97e-4, 2.01e-3, 4.87e-4, 5.07e-5} for 25, 20, and 16μA, respectively. Zero values indicate they change the minimum of Eq. (3.18) by less than 1%.

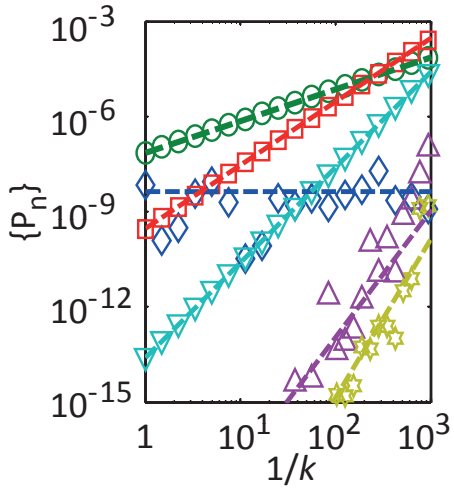

Figure 3.8: $\{P_n\}$ at 16μA found under different scaling factors, k. $\diamondsuit$, $\bigcirc$, $\square$, $\bigtriangledown$, $\bigtriangleup$, and $\star$ represent $P_{n=0}$ to $P_{n=5}$ respectively. The corresponding dashed lines have slopes equal to n on a log-log plot. The plot shows a linear optical loss of η scales $P_n \rightarrow \eta^n P_n$.

3.6 Conclusions

The almost identical outcome of Detector Tomography and the nonlinear SPD model confirms both of them are reliable. This is a good example of how Detector Tomography is particularly useful for characterizing detectors outside their normal operating regime, where there is no model for their operation. Even though only classical optical pulses were used as input states for the tomography, the resulting POVM allows one to predict the detector response to any input, including non-classical states such as Fock states. We expect the nonlinear SNSPD model to be useful for other nonlinear binary detectors such as two-photon absorbing Avalanche Photodiodes and Electron Multiplying CCDs (thresholded). It will also be useful for characterizing conventional SPDs and putting limits on their nonlinearity.

Chapter 4

Gated Mode Superconducting Nanowire Single Photon Detectors

We have described our semi-empirical model, nonlinear SPD model and all related experiments in the last two chapters. We now turn our attention to the second fold of this thesis, i.e. gated mode SNSPDs (GM-SNSPD).

There are two timing modes of operation for single photon detectors in general. Free-running mode (FM), refers to the detectors that can detect photons continuously, while gated-mode (GM) describes detectors that are only single photon sensitive during discrete time slots. Figure 4.1 is an illustration of this. FM-SPDs are more useful in applications like measuring spontaneous emission life time of quantum dot emitters [78] in which the exact arrival time of the photons are unknown or itself is under study. GM-SPDs can be advantageous in applications like quantum key distribution [79] in which useful photons arrive in pre-defined time slots, and thus can be efficiently detected by synchronizing the photon source with the open time slots of the detector.

GM-SPDs can have better noise performance because they naturally reduce the effect of the unsynchronized photons that hit the detector, i.e. the unwanted photons that might originate from the environment, not from the source. The price would be more complex electronics to synchronize and gate the detector. We also note that in applications that GM-SPDs are more useful, there is a demand for having a higher count rate. This can

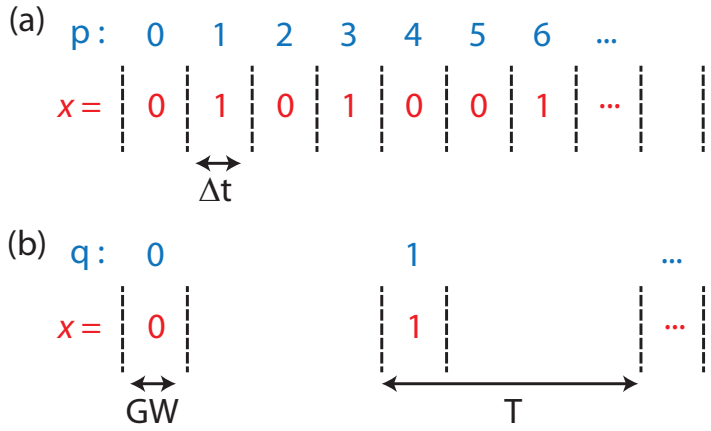

Figure 4.1: (a) Illustration of a free-running SPD. Incoming photons are continually detected and the result which is a random process, is put into time bins (with width Δt) labeled by p. (b) Illustration of a gated-mode SPD. Only the photons incident during the gate width (GW) are detected. The gates are labeled by q. We are assuming both Δt and GW are smaller than the detector dead time to ensure the output is a binary random process, $x \in \{0, 1\}$, where 0 and 1 show No-Detection and Detection events.

translate itself into faster communication links or more accurate experimental results with less acquisition time, significant advantages for different fields.

As implicitly mentioned in all experiments of this thesis till now, SNSPDs are conventionally operated in free-running mode, i.e. biased by a constant current. Although they provide high quantum efficiency, low dark counts and small jitter time [80], a prohibitive *latching* effect severely limits the maximum count rate [9, 10]. Here we report the first operation of SNSPDs in a gated mode (GM) that exploits *single photon triggered latching* itself to detect photons. We show operation of a large active area single element GM-SNSPD at 625MHz, more than one order of magnitude faster than its FM counterpart.

The chapter starts with an introduction to the concept of GM-SNSPD and its implementation. The necessary experiments are then explained to characterize both GM and FM operations and to compare the performances. We also present series of modeling and simulation steps, to show what limits the ultimate count rate of a GM-SNSPD and how it

can be improved. An e-print of a journal article written on this work is available in [81].

4.1 The Concept and Implementation of GM-SNSPD

To date SNSPDs have been operated in free-running mode, for which an equivalent circuit model is shown in Fig. 4.2 (a) [64]. In absence of photons, the superconducting wire shunts current away from the load, leaving zero voltage across it. The absorption of a single photon triggers an unstable resistive hotspot on the nanowire that momentarily pushes the current out to the load resistance, R_L, hence making a rising voltage. The hotspot then cools down with a sub-nanosecond time constant τ_{th} for all the materials the SNSPDs have been made from thus far [82]. Meanwhile, suppressed current of the nanowire rises again to its initial value with an electrical time constant that is set by the kinetic inductance of the superconductor, L_K, and the load resistor, $\tau_e = L_k/R_L$. The SNSPD cannot efficiently detect the next photon before the end of these transients [64]. That is because the quantum efficiency of a SNSPD strongly depends on the current through it (see G_1 in Fig. 2.8 for instance). The large kinnetic inductance of a single long meandering nanowire that fills the active area of a typical SNSPD, together with the standard microwave cable with characteristic impedance equal to 50Ω, can make τ_e orders of magnitude larger than τ_{th}. This severely limits the count rate of such FM-SNSPD to sub-tenth of GHz range [56, 83].

There have been different approaches to reduce τ_e. Kinetic inductance which is a material dependant parameter, can be reduced by exploiting superconducting materials with smaller London penetration depth [84, 85, 82]. It can also be reduced by changing the geometry of the device from a single long nanowire to some shorter wires that are either connected in parallel [86, 87, 88], operating as independent smaller pixels [7] or placed under a nano-antennae [50]. Alternatively, R_L can be increased by putting a resistor in series with the nanowires [9].

However there is another limitation that doesn't let τ_e to be pushed to much smaller values without a compromise on quantum efficiency: following a photo-detection the nanowire would latch to a resistive state for ever if τ_e be too small for a fixed bias current. The reason which has been well studied in [9, 10] recently, is in the dynamics of the self-rest

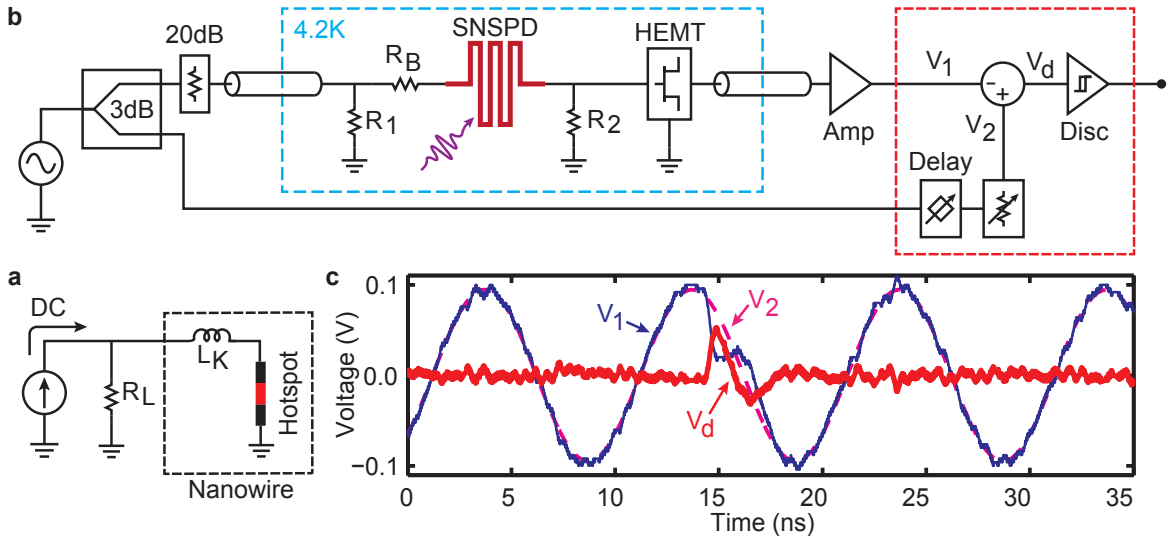

Figure 4.2: Gated mode operation of SNSPDs. (a), Equivalent circuit model for a FM-SNSPD. L_K is the nanowire kinetic inductance and R_L is the load seen by the nanowire. (b), Schematic of the circuit showing the major elements. R_1 is a 50Ω load resistor and R_2 is a 50Ω current sense resistor. We used a high electron mobility transistor (HEMT) to both amplify the weak signal and to further isolate the Nanowire from reflected signals. (c), A typical set of waveforms showing the detector latches at the current maxima, returns to superconducting state at a smaller current and the difference signal jumps up as a result.

process when the current is derived back to a hot nanowire. In the following, we show for the first time that in GM-SNSPDs this condition on τ_e can be relaxed. Thus GM-SNSPDs can operate mush faster, at a count rate that is purely limited by τ_{th}.

To speed up the device in gated mode, we increase R_L to decrease τ_e even bellow the limit set by the reset dynamics. Such detector would obviously never self-reset after a photo-detection or a dark count. However, it can periodically detect photons if an alternating current with a positive DC offset be applied to the nanowire. At the peak of the current, the SNSPD latches upon a photo-detection or a dark count. The latched nanowire will then be forced to reset to superconducting state by the next minima of the current. So in contrast to free running mode for which latching to resistive state is a

forbidding effect, here we exploit single photon triggered latching itself to count photons.

Assuming the peak of biasing current in GM-SNSPD is equal to the DC biassing current of the same chip but operating as a FM-SNSPD, we expect both of the detectors show the same quantum efficiency to the photons arriving at the current peak. However, because in GM-SNSPD current does not always run through the chip, we expect a smaller dark count rate for it compared to FM-SNSPD.

We use the circuit shown in Fig. 4.2 (b) to implement a GM-SNSPD. A signal source with adjustable DC level is made exploiting a bias-Tee, an RF sinusoidal source and an adjustable DC voltage source (the figure just shows the resulting signal source). The voltage from a signal source is split into two paths using a 3dB power splitter. One path undergoes heavy attenuation and and then transmitted to cryogenic temperature by using a coaxial cable and a termination resistor, $R_1 = 50\Omega$. This creates an alternating bias current with a DC offset in the SNSPD by using a biasing resistor, R_B. This current is sensed by current sense resistor, $R_2 = 50\Omega$ together with two amplifiers. The first amplifier is a high electron mobility transistor (HEMT). Being placed just beside the SNSPD chip, it amplifies the sensed signal on R_2 and also isolates the SNSPD from unwanted reflected signals, hence making the current through the SNSPD more predictable. The HEMT is powered by a room temperature bias-Tee (not shown in the figure) placed before the second amplifier which is an RF amplifier (Miteq, AFS3-00100200-10-CR-4) with 38dB of gain. This generates the signal V_1 which has information about detected photons embedded inside. The other path only undergoes an adjustable delay and attenuation and serves as a reference signal, V_2.

The difference of the two signals, $V_d = V_2 - V_1$ would be small in absence of incoming photons for an appropriately adjusted circuit. However, as illustrated in Fig. 4.2 (c), V_d will jump up whenever the detector latches. We use discriminated V_d to count photons in gated mode.

One difference with our setups in previous chapters (see Fig. 3.5 for instance) is higher frequency of the signals such that our counter couldn't be useful any more. Also, contrary to FM mode, for GM-SNSPDs it was not known in the beginning how the resulting signal, V_1 should be post processed to yield detection events. So we managed to implement the

processing part in a highly flexible way to allow trials for finding an appropriate read out scheme. All the parts shown in the right dashed box in Fig. 4.2 (b) are digitally implemented. The two signal pathes described above are connected to two channels of a high speed oscilloscope (Tektronix DSA70000 series) that makes a digital representation of the incoming analogue signals. This is transferred to Matlab installed on a remote PC using a GPIB interface. The Matlab then mimics the schematic shown in the right dashed box. It can also serve as a counter, as an autocorrelator and basically as all post-processing tools we need to study GM-SNSPDs.

The study of GM-SNSPDs wouldn't be complete without comparing them with FM-SNSPDs. To make FM equivalent with minimal changes, we used DC signal source in the same circuit of Fig. 4.2 (b) but R_1 replaced with a large 100nF capacitor. Such circuit delivers a DC voltage to $R_1 \rightarrow 100$nF and thus makes a DC current in the superconducting nanowires. Writing the Norton equivalent of the circuit composed of 100nF capacitor, R_B, R_2 and SNSPD at high frequency, one gets the same circuit of Fig. 4.2 (a) with $R_L = R_B + R_2$. So the changes make an FM-SNSPD in which the generated signal can be read from the same chain of amplifiers and the same post processing hardware. However, we used a different Matlab code to interpret the resulting signal as the output of an FM-SPD (see Fig. 4.1 (a)) rather than a GM one (see Fig. 4.1 (b)).

Similar to Fig. 3.5, the cryogenic setup consists of the dipstick probe details of which reported in [77]. Also similar to the setup of section 2.2, the photons are delivered to the active area of the SNSPD using a fiber. However, we installed the fiber far away from the SNSPD to make a large spot on the device. This degrades the system quantum efficiency but it is good for our studies because it ensures the optical coupling doesn't change a lot by successive cooling down cycles. Finally, we have used similar SNSPD chips as the previous chapters: 500μm long, 4nm thick, 120nm wide Niobium Nitride on Sapphire with an active area of 10μm$\times$10μm.

The highly flexible setup we implemented, allowed us to do variety of different analysis on both FM and GM-SNSPDs. These are discussed in the next section.

4.2 Experimental Characterization

In this section, we only present the main results that are important for characterization of a typical GM-SPD, rather independent of its internal workings. The quantitative understanding of the details of operation of our GM-SNSPD would not be possible without the aid of smaller experimental and modeling activities. These details will be explained in the *methods* section later in this chapter.

4.2.1 Performance in Time: Maximum Count Rate, Gate Shape and After Pulsing

To measure speed, we excite both FM and GM detectors using an attenuated 1310nm CW laser at a level that makes measured count rate linearly proportional to the laser intensity, thus ensuring both single photon sensitivity [69], and being away from the saturation level (see Eq. (2.9)). The recorded detection events gives a series of zeros and ones, and makes a random process, x (see Fig. 4.1). We use Matlab to calculate unbiased autocorrelation function on the x from both types of operations, a function that will be useful for maximum count rate characterization.

For FM-SNSPD, x equals $x(p\Delta t)$, where p is an integer and Δt is a fine sampling interval set on the analog to digital converters (see Fig. 4.1 (a)). The unbiased autocorrelation function gives the joint probability of two click events during time intervals Δt, separated in time by $n\Delta t$

$$\Gamma(n\Delta t) = P(p\Delta t, \Delta t; (p+n)\Delta t, \Delta t), \tag{4.1}$$

where n is an integer. This reduces to

$$\Gamma(n\Delta t) = \begin{cases} R\Delta t\ SQE & n = 0 \\ R\Delta t\ SQE \times R\Delta t\ SQE(n\Delta t) & n \neq 0 \end{cases} \tag{4.2}$$

where R is the rate of incident photons, SQE denotes the average system quantum efficiency and $SQE(n\Delta t)$ denotes the system quantum efficiency for a time slot that is $n\Delta t$ after a detection event. Therefore

$$\frac{\Gamma(n\Delta t)}{\Gamma^2(0)} = \frac{SQE(n\Delta t)}{SQE} \qquad n \neq 0. \tag{4.3}$$

This should ideally be a flat line for $n \neq 0$ unless the limited speed of the detector makes the click events at $(p+n)\Delta t$ and $p\Delta t$, non-independent.

For GM-SNSPD, x equals $x(qT)$, where q is an integer that labels successive gates and T is the gating period (see Fig. 4.1 (b)). The unbiased autocorrelation function gives the joint probability of two click events during two gates separated in time by nT

$$\Gamma(nT) = P(qT; (q+n)T). \tag{4.4}$$

This reduces to

$$\Gamma(nT) = \begin{cases} DP & n = 0 \\ DP \times DP(nT) & n \neq 0 \end{cases} \tag{4.5}$$

where DP denotes the average click probability per gate and $DP(nT)$ denotes the click probability in a gate that is nT after a detection gate. Therefore

$$\frac{\Gamma(nT)}{\Gamma^2(0)} = \frac{DP(nT)}{DP} \qquad n \neq 0. \tag{4.6}$$

This should ideally be a flat line for $n \neq 0$ unless the limited speed of the detector makes the click events at gates $(q+n)$ and q, non-independent.

Comparing Eq. (4.3) and Eq. (4.6), we note the same quantity, $\Gamma(n)$ normalized to $\Gamma^2(0)$, can be used for speed characterization of both FM and GM SNSPDs. Also for large n values, we expect $SQE(n\Delta t) \to SQE$ and $DP(nT) \to DP$, and thus according to Eq. (4.2) and Eq. (4.5), $\Gamma^2(0)$ is equal to $\Gamma(\infty)$. Therefore, we will use $\Gamma(\tau)/\Gamma(\infty)$ to measure the speed in both operation regimes, where $\tau = n\Delta t$ in FM and $\tau = nT$ in GM.

Figure 4.3 (a) shows the measured normalized autocorrelations. For GM: R_B is 650Ω, the bias is 625MHz sinusoidal (see methods section 4.4.4 for detailed explanation of these selections) with minima and maxima equal to -2μA and 90% of critical current respectively (see methods sections 4.4.5 for details of the procedure used to experimentally set these currents). For FM: we tried to choose R_L for operation at maximum speed while avoiding latching, we set R_L equal to 100Ω (equivalent to $R_B = 50\Omega$, see methods section 4.4.3 for details of how we conclude this would result in the maximum operation speed), the DC bias is 90% of critical current. The result shows for having $\Gamma(\tau)$ changed by less than ±10%, τ should be greater than about 22ns in FM and 1.6ns in GM, i.e. more than one order of magnitude speed up in GM.

Exciting the GM-SNSPD with a faint CW laser and making a time histogram of the detection events within a gate period, provides direct information on how the quantum efficiency changes with in a gate period. Figure 4.3 (b) shows the measurement result on the 625MHz GM-SNSPD described above. It shows the quantum efficiency changes less than 5% for a time window equal to 57ps (equivalent to about 1/30th of the gating period, T). The curve shown on the same figure is obtained using

$$\frac{SQE(I_{DC} + I_{AC}sin(\frac{2\pi t}{T}))}{SQE(I_{DC} + I_{AC})}, \tag{4.7}$$

where SQE represents system quantum efficiency whose functionality with biassing current is known using SQE versus bias current measurement for FM-SNSPD as shown in Fig. 4.4 and will be discussed in the next subsection. The agreement between the curve and the points confirm nothing unknown is taking place here and variation of SQE in a gating period is only due to variation of the bias current. 57ps is already wide enough for detection of picosecond wide optical pulses, however we note 1/30th of T would naturally increase if we could use latest generation of high quality SNSPDs. That's because for our poor SNSPD chip, the curve of SQE is always ascending with bias current (see Fig. 4.4), while for a high quality SNSPD the curve saturates at a high bias current (see quantum efficiency versus bias current in [89] for instance). Therefore without any change in the gating methods we used, we expect gates with wider width and flatter response at the peak for higher quality SNSPD chips.

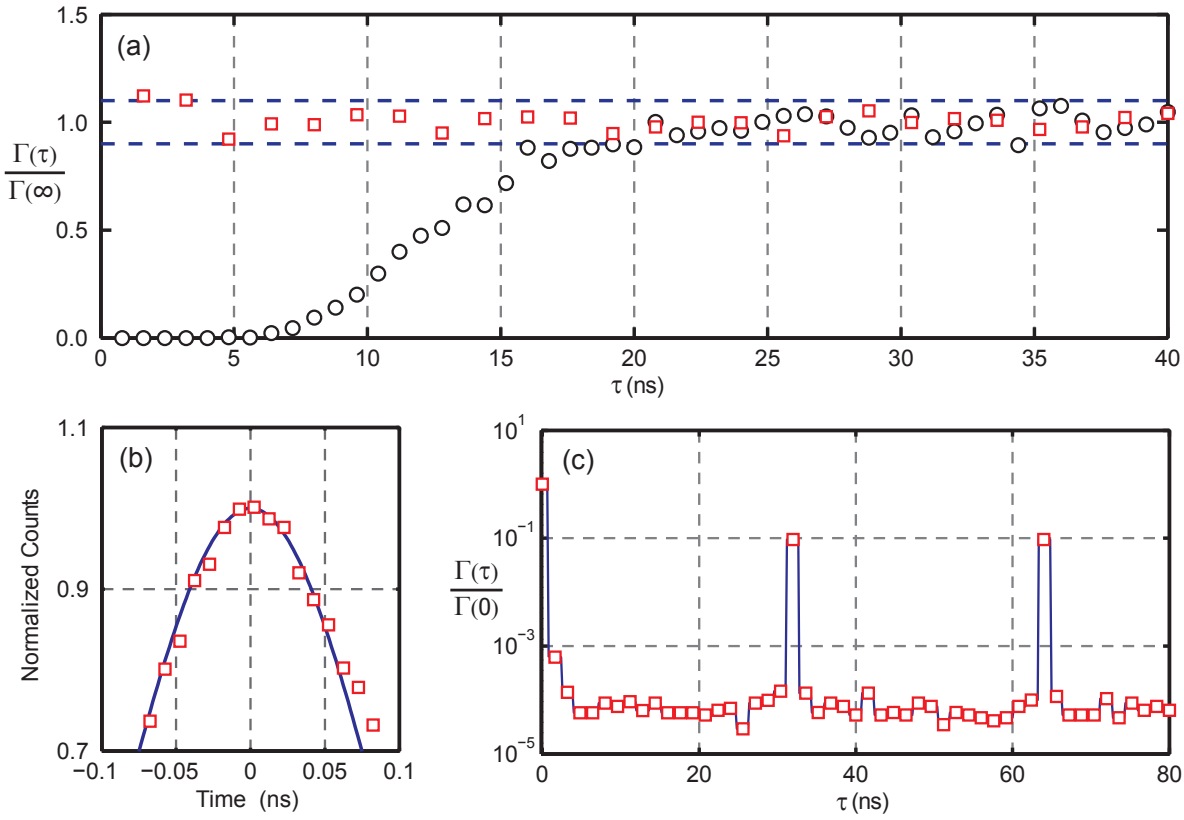

Figure 4.3: Autocorrelation and gate shape measurements. (a), Normalized autocorrelation for FM-SNSPD with R_L equal to 100Ω (black circles) and our 625MHz GM-SNSPD (red squares), both under CW laser illumination. Non-flat autocorrelations show dependency of two detector clicks separated in time by τ. As can be seen GM-SNSPD operates more than one order of magnetite faster than FM-SNSPD . (b), Normalized time histogram of detection events within a gate period of our 625MHz GM-SNSPD under a CW laser. The figure illustrates the gate shape of a GM-SNSPD. (c), Normalized autocorrelation for 625MHz GM-SNSPD excited with a pulsed laser at 31.25MHz. It demonstrates the GM-SNSPD does not suffer from large after pulsing effects.

Convectional gated SPDs like IR-APDs tend to generate after pulses, i.e spontaneous fake clicks in the gates following a gate with a real detection event. Consequently, commercial IR-APDs (like the ones mentioned in chapter 1) come with adjustable dead-time to avoid excessive after pulses. It is natural to study the same effect in GM-SNSPDs as well. To this end, we keep the biasing of the above GM-SNSPD unchanged but excite it with a $625/20 = 31.25$MHz, 1310nm pulsed laser. Following Eq. (4.4), the autocorrelation function in this case would ideally (i.e. in absence of after pulses) be

$$\Gamma(nT) = \begin{cases} \dfrac{DP + 19DCP}{20} & n = 0 \\ \dfrac{2DP \cdot DCP + 18DCP^2}{20} & n \neq 0 \; and \; n \neq 20N \\ \dfrac{DP^2 + 19DCP^2}{20} & n = 20N \end{cases} \tag{4.8}$$

where N is an integer, DP is detection probability per gate and DCP is the dark count probability per gate. Assuming the GM-SNSPS is excited by laser pulses with sufficient intensity that makes $DP \gg DCP$, Eq. 4.8 approximates to

$$\Gamma(nT) \approx \begin{cases} 0.05 \; DP & n = 0 \\ 0.1 \; DP \cdot DCP & n \neq 0 \; and \; n \neq 20N \\ 0.05 \; DP^2 & n = 20N \end{cases} \tag{4.9}$$

Therefore,

$$\frac{\Gamma(\tau = nT)}{\Gamma(0)} \approx \begin{cases} 2DCP & n \neq 0 \; and \; n \neq 20N \\ DP & n = 20N \end{cases} \tag{4.10}$$

This normalized autocorrelation is shown in Fig. 4.3 (c). As expected from Eq. (4.10), it shows clear jumps each 20 gating periods and remains on a flat level determined by dark count probability per gate. More interestingly, $2DCP$ as can be read from the flat level is compatible with our dark count measurements as will be discussed in Fig. 4.4. This is except for n=1 where DCP is enhanced by an after pulsing probability about 0.03%. We attribute this to either unwanted oscillatory behavior in the biasing current following

a photo-detection or temperature rise in the corresponding gate. While both of these possibilities will be seen in the simulations of the next section, the final conclusion on the physical origin of this needs more experimental investigations.

4.2.2 Quantum Efficiency and Dark Count Rate

We have shown in the previous subsection that the maximum count rate of GM-SNSPD is more than one order of magnitude higher than its FM counterpart. However, the improvement in speed should not be at the cost of degradation in Quantum Efficiency (QE) or Dark Count Rate (DCR). In this subsection we explore QE and DCR of our GM-SNSPD compared to the FM one.

QE and DCR of both of the operation modes are compared in Fig. 4.4. For GM we apply 100MHz bias and lock a 200ps pulsed laser to the bias maxima. For FM we used an attenuated CW laser with the same wavelength. Quantum efficiency for GM and FM shows good agreement, proofing the GM operation doesn't degrade the efficiency of the detector. However, as the GM-SNSPD is not always on, its dark count rate is smaller than that of FM-SNSPD by about one order of magnitude.

To quantitatively work out the reduction in GM-DCR, we note the experimental FM-DCR in Fig. 4.4 has an exponential dependance with the bias current. So it can be expressed as

$$DCR_{FM} = exp\Big(\alpha(I_B - I_0)\Big) \tag{4.11}$$

where I_B is the DC bias current, and α and I_0 are two fitting parameters. We follow a similar reasoning that lead to Eq. 2.6 of our semi-empirical model: DCR_{GM} at time t in a gate period equals DCR_{FM} provided the detector has not been perversely latched. Therefore

$$DCR_{GM}(t) = DCR_{FM}\Big(I_{DC} - I_{AC}\ cos(\frac{2\pi t}{T})\Big)\left[1 - \int_0^t DCR_{GM}(t)\ dt\right], \tag{4.12}$$

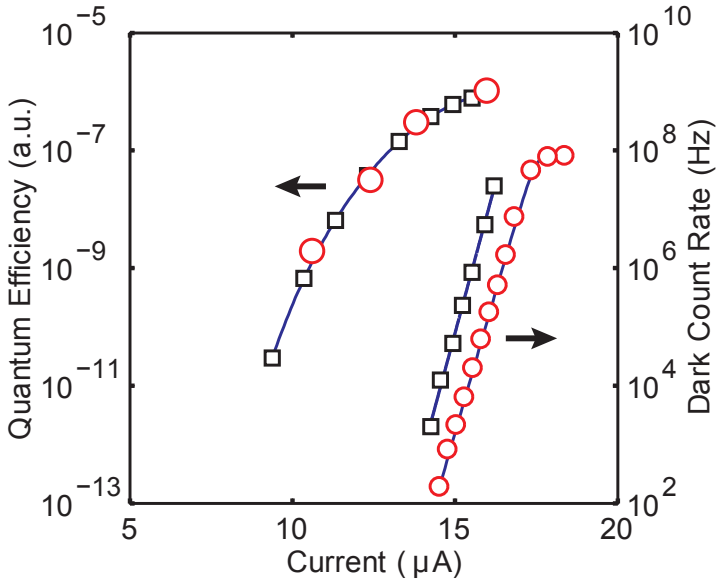

Figure 4.4: Quantum Efficiency and Dark Count measurements. Black squares are for FM-SNSPD and red circles are for 100MHz GM-SNSPD. The current shown is the DC biasing current or the peak of current for FM and GM respectively. For GM efficiency measurement, a 200ps pulsed laser was locked to the peaks of the current through the SNSPD. Note for GM-SNSPD dark count rate saturates at the gating frequency at higher currents.

from which we get

$$DCP = \int_0^T DCR_{GM}(t)\, dt = 1 - exp\left(- \int_0^T DCR_{FM}\Big(I_{DC} - I_{AC}\ cos(\frac{2\pi t}{T})\Big)\ dt \right), \quad (4.13)$$

where DCP is the dark count probability per gate in GM operation. The average dark count rate in GM mode can thus be calculated by DCP/T. In Fig. 4.4 the solid line under measured DCR_{GM} is calculated from DCR_{FM} by this method. The good agreement suggests nothing but a sinusoidally shaped current is making DCR in gated mode less than free-running mode. A significant feature of Eq. (4.13) becomes clear when trying to

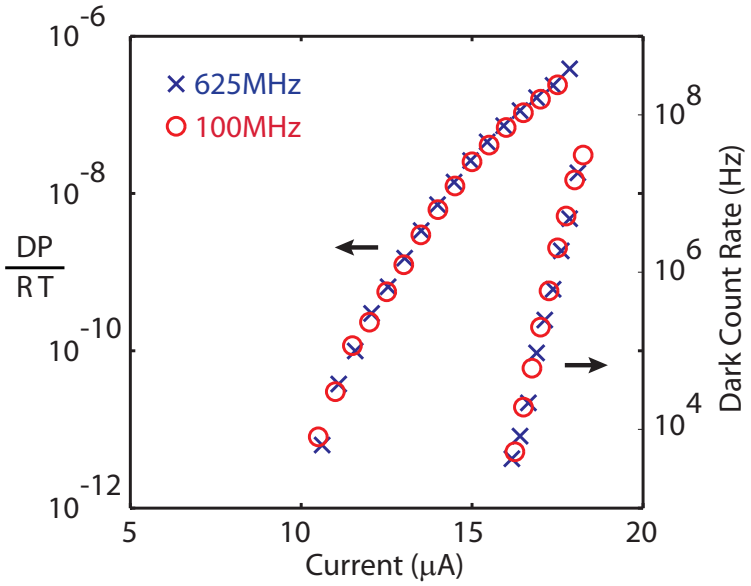

Figure 4.5: Average quantum efficiency and dark count rate measurements of a GM-SNSPD at 100MHz (∘) and 625MHz (×). In this plot, the current for 625MHz operation is manually reduced by 3.5% with respect to what we actually adjusted during the experiment. This is just to show both of the curves of efficiency and dark counts agree at two distant frequencies. We attribute 3.5% to the error of our methods for adjusting high frequency current (see methods section 4.4.5).

simplify the math for $DCP \ll 1$. Under this condition and assuming $\alpha I_{AC} \gg 1$ (which is the case for our SNSPD), Eq. (4.13) approximates to

$$DCR_{GM} = \frac{DCP}{T} \approx \frac{DCR_{FM}(I_{DC} + I_{AC})}{\sqrt{2\pi\alpha I_{AC}}}. \tag{4.14}$$

This indicates in gated mode dark count probability per gate is inversely proportional to gating frequency and thus dark count rate is independent of biasing frequency. Indeed, we measured DCR_{GM} of a GM-SNSPD at 100MHz and 625MHz. The result is shown in Fig. 4.5 which experimentally proves the correctness of Eq. (4.14).

We couldn't synchronize our laser to the bias current at higher frequencies to measure quantum efficiency with the same method as Fig. 4.4. However, following the same method

that lead to Eq. (4.13) and using the same functionality of quantum efficiency with biasing current that was suggested by Eq. (4.7) and experimentally proved to be correct by Fig. 4.3 (b), we can write down

$$DP = 1 - exp\left(-\int_0^T SQE\Big(I_{DC} - I_{AC}\ cos(\frac{2\pi t}{T})\Big)\ R\ dt\right), \tag{4.15}$$

where DP is detection probability be gate, R is the rate of incident photons and T is the gating period. For small enough laser intensities where $DP < 0.1$, Eq. (4.15) approximates to

$$\frac{DP}{R\ T} \approx \int_0^1 SQE\Big(I_{DC} + I_{AC}\ sin(2\pi x)\Big)dx, \tag{4.16}$$

where we have replaced $t \rightarrow Tx$. The message of Eq. (4.17) is clear: for a CW laser exited GM-SNSPD, the average quantum efficiency, i.e. detection probability per gate divided by the average number of incident photons per gate period, should be independent of the gating frequency. Indeed, the experimental result shown in Fig. 4.5 confirms this.

Therefore, with all the calculations and experiments of this subsection we showed: our GM-SNSPD works with the same efficiency of FM-SNSPD, dark count probability per gate is inversely proportional to gating frequency and the dark count rate is much smaller than FM-SNSPD.

4.3 The Ultimate Limits and Simulations

We have experimentally explored different features of gated mode operation of SNSPDs in the last section. The main advantage is increased maximum count rate and reduced dark count rate. A natural question that rises is that of the ultimate limits of GM operation. In this section we try to exploit physical modeling and numerical simulations to find the answer. Following the same convention of this chapter up to now, we postpone some rather independent tasks to the methods section.

The simulations we are looking for are *Electro-Thermal*. Electric part accounts for the dynamics of voltages and currents in the circuit built around the superconducting nanowire, namely the circuit of Fig. 4.2 (b). The thermal part on the other hand, captures the thermal process that goes on within the nanowires. Therefore we need two models for simulating the system: a thermal one and an electrical one.

To date, the electrical model shown in Fig. 4.2 (a) has been the basis for doing electro-thermal simulations on the SNSPDs [65, 64, 90]. However, the high frequency content of the driving signal that we use in GM-SNSPDs together with increased R_B, makes this model not appropriate for for our case. So we developed a more suitable electrical model of our SNSPD as shown in Fig. 4.6 (a) (see methods section 4.4.1 for details). We could do our simulations based on this rather accurate model. But, large number of components would make interpretation of the results difficult. Instead, we approximate this model into a simplified version shown in Fig. 4.6 (b) (see methods section 4.4.2 for details). This will be used in all our simulations. Although, compared to the previous model shown in Fig. 4.2 (a), the change is a single component, C_P, but this will be proved to be the most restricting factor for the maximum count rate of our GM-SNSPD.

The thermal model for our simulation is the same as the one reported by Yang et.al. [65]. It is basically a 1D heat transfer equation for describing the dynamics of a hotspot on the superconducting nanowire. The equation has the form

$$\rho J^2 + k\frac{\partial^2 T}{\partial x^2} - \frac{\alpha}{d}(T - T_{sub}) = \frac{\partial cT}{\partial t}, \tag{4.17}$$

where x, $T(x,t)$, $J(t)$, $\rho(T(x,t))$, $k(T(x,t))$, $\alpha(T(x,t))$, d and $c(T(x,t))$ are coordinate, temperature, current density, electrical resistivity, thermal conductivity, thermal boundary conductivity, nanowire thickness and specific heat, respectively. We use the same nonlinear temperature and phase dependencies of the parameters as in [65]. The thermal model is coupled to the electrical model through the voltage and current on the hotspot shown in Fig. 4.6 (b). We assume the nanowire is long enough that the hotspot never reaches the two ends of it, and thus the two ends can always be assumed to be at the substrate temperature. Also we assume the hotspot has an initial length of about 10nm with a peak temperature slightly above superconducting transition temperature.

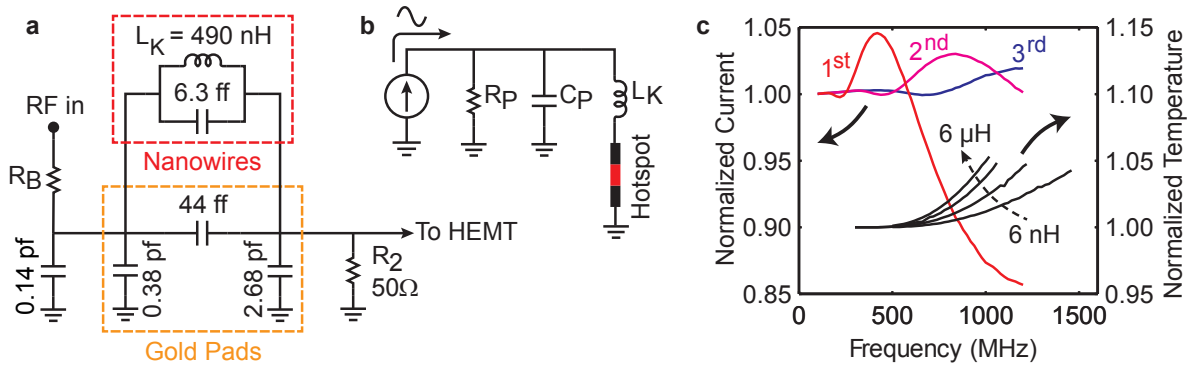

Figure 4.6: (a), Electrical circuit model for our GM-SNSPD (see methods section 4.4.1). (b), A simplified version that was used to do electro-thermal simulations (see methods section 4.4.2). (c), Simulated peaks of current in the gates following a photo-detection normalized to 95% of the critical current for $R_P = 725\Omega$ (equivalent to $R_B = 650\Omega$), $C_P = 0.57$pf and $L_K = 490$nH. Also shown is the maximum temperature on the surface of the Nanowire at the first gate following a photo-detection normalized to 4.2K for a critically damped circuit with $C_P = 0.01$pf and L_K equal to 6nH, 60nH, 600nH and 6000nH.

We simulate the peaks of current in the gates following a photo-detection in our GM-SNSPD, i.e. we put a hotspot on the nanowire at a peak of current to make it latch and then we look at the current through the nanowire after it was forced to reset by the current minima. The peaks of this current should ideally return to its original value for having the detection efficiency and dark counts intact in the succeeding gates. The simulation result is shown in Fig. 4.6 (c) for R_P equal to 725Ω (equivalent to $R_B = 650\Omega$). It shows our GM-SNSPD is far from the ideal case: only at gating frequencies less than about 300MHz or at about 600MHz the peaks don't change significantly. Indeed, this is how we have selected the gating frequencies in the experiments described. Therefore, the oscillatory response of an under-damped RLC circuit puts a purely electrical limitation on the gating frequency of our GM-SNSPD.

The physical origin of C_P as shown in Fig. 4.6 (a) suggests C_P can be reduced to about 0.01pf if R_B be integrated to the SNSPD chip. Therefore, with $C_P = 0.01$pf, we repeat the simulation for values of L_K ranging 6nH to 6μH. For each L_K, we choose R_B such that it

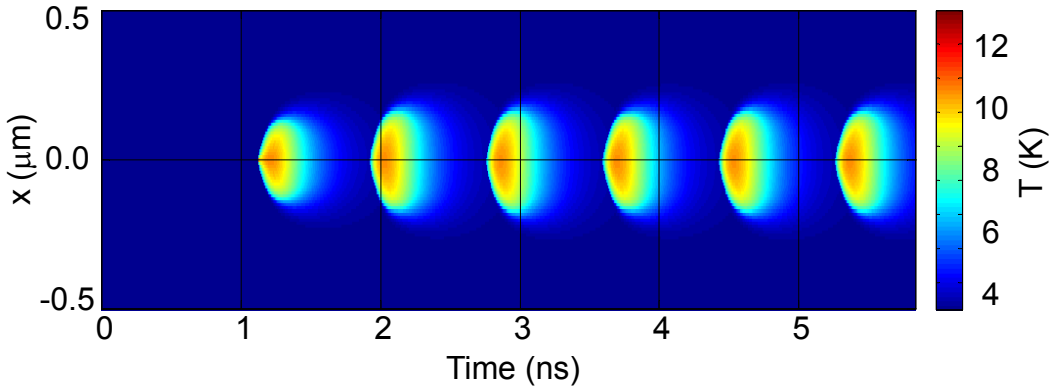

Figure 4.7: Re-latching effect in GM-SNSPDs. At a high gating frequency the nanowire doesn't have enough time to completely cool down to substrate temperature before the arrival of the next current peak. Therefore it latches again and a sequence of hotspots appears that stops the detector from correct operation.

makes a critically-damped RLC circuit both to avoid oscillatory behaviors and to have the circuit return to its steady state as fast as possible. With a procedure similar to the previous simulation, we simulate for the maximum temperature of the nanowire at the center of the gate following a detection gate. The results are shown in Fig. 4.6 (c). The curves are up to the frequency at which the detector re-latches in the next maxima of the current due to elevated nanowire temperature. We also checked that the currents of Fig. 4.6 (c) are horizontally flat for this case, confirming the fast enough electrical response. Figure. 4.7 illustrates the re-latching of the GM-SNSPD by showing the temperature distribution, $T(x,t)$, along the nanowire when it is driven with at a high gating frequency.

Therefore, we showed for GM-SNSPDs the maximum count rate can be purely limited by thermal response of the SNSPD. This is in contrast with FM operation that an electro-thermal process restricts higher count rates at a much lower rate. Another significant finding is that for GM-SNSPDs, increasing L_K over three orders of magnitude from 6nH to 6μH, decreases maximum gating frequency for just about 33%. So unlike FM operation in which for having higher speed, the L_K and as a result the active area of the detector should be reduced [9, 10], for GM operation both high speed and large active area can be

achieved simultaneously, a significant feature for making SPDs that are both high speed and highly efficient.

4.4 Methods

In the previous sections we presented the concept and implementation of GM-SNSPDs together with our major results showing the performance, limitations and advantages of GM operation. However, running a GM-SNSPD would have not been possible without the support of models that help quantitative understanding of different aspects of GM operation. In this section we presents the details of these supportive works that are frequently referred to throughout the chapter.

4.4.1 SNSPD Electrical Model

In this subsection we present the details for derivation of our SNSPD electrical model in Fig. 4.6 (a). We decomposed the device into Gold pads and NbN nanowires as shown in Fig. 4.8 (a) and (b), respectively. High frequency electromagnetic simulation software, SONNET, is then used to solve for the S-parameters of the two structures separately. Perfect conductor on top of a loss-less substrate with relative permittivity equal to 11.35 [91, 92] was assumed to simulate for the Gold pads. Surface inductance equal to 90pH (equivalent to London Penetration depth equal to 532nm [64] at thickness of 4nm) was used to simulate the superconducting meandering nanowires. In each case we simulated for the phase and amplitude of the S-parameters up to 5GHz. These results are then converted to the circuit model by using our intuition and the functions available in Agilent Advanced Design System (ADS). The 0.14pf capacitor in Fig. 4.6 (a) is obtained with the same methods for a small pad on a printed circuit board where the SNSPD was wire-bonded to.

To test the validity of the resulting model, we put the SNSPD chip in the circuit shown in Fig. 4.2 (b) with $R_1 = \infty$, $R_2 = R_B = 50\Omega$ and the HEMT amplifier disconnected. We measured the input reflection coefficient, Γ_{in}, using a vector network analyzer (VNA)

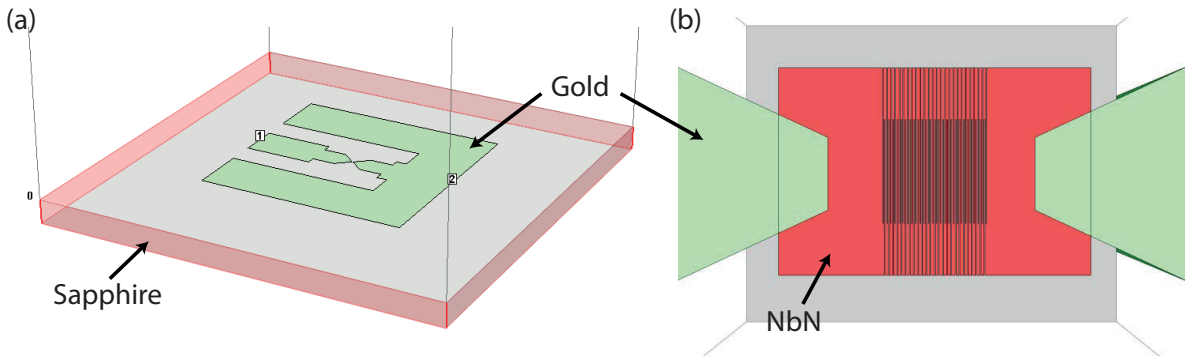

Figure 4.8: Drawing of the Gold pads and NbN nanowires of our SNSPD in SONNET. The S-parameters was simulated by SONNET and the results were converted to the circuit model of Fig. 4.6 (a) by ADS.

calibrated at the cryogenic end of the coax while the device was cooled down to 27K and 4.2K. We calculate the input impedance of our system seen from the end of the coax cable using the measured Γ_{in}. Alternatively, we used ADS to simulate for the input impedance using the model of Fig. 4.6 (a) [1]. Both of the results are shown in Fig. 4.9. The impedance is inductive up to a resonant peak and then the capacitive effect dominates. The agreement between the measurement and what we could simulate in ADS using the developed circuit model confirmed the model is fairly accurate at least up to 2GHz. The most significant deviation between the results is in the phase of input impedance from 2GHz to 5GHz. This might be due to our rather poor VNA calibration at higher frequencies.

[1] 27K is above the critical temperature of our superconducting nanowires ($T_C \approx 11$K). So for ADS simulation, we replaced L_K by a resistor equal to 2.3MΩ equivalent to our measured resistance of SNSPD at 27K. Also, as will be discussed in section 4.4.5, the measured high frequency model of our actual 50Ω resistors is an ideal 50Ω resistor in series with a 0.9nH inductor. We have considered this in these simulations.

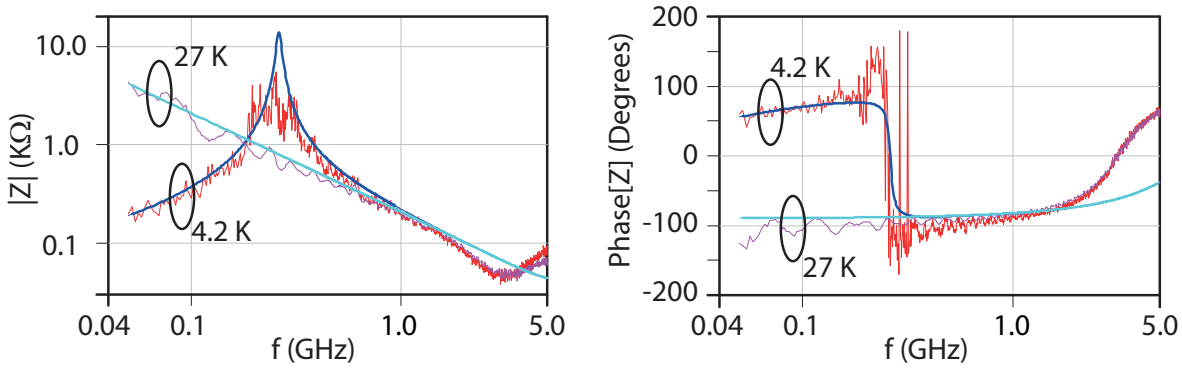

Figure 4.9: Comparing the input impedance of a test setup that our SNSPD sits in, and the simulation of the same circuit using the SNSPD model of Fig. 4.6 (a) at two superconducting (4.2K) and non-superconducting (27K) phases. The agreement proves the accuracy of the model up to about 2GHz.

4.4.2 Electrical Model Approximation

All the components of our electrical mode developed in the last subsection, have tight physical connections. However, we were looking for something simpler to make the interpretation of our electro-thermal simulations more straight forward. Therefore, looking at Fig. 4.6 (a), we followed the following steps to make an approximate version:

- Replace RF_{in} with a voltage source in series with a 25Ω output impedance.
- Write down the Norton equivalent of the voltage source and $R_B + 25\Omega$.
- Identify $Z_1 \equiv (R_B + 25) \parallel$ (0.14pf+0.38pf), $Z_2 \equiv L_K \parallel$ (6.3ff+44ff) and $Z_3 \equiv R_1 \parallel$ 2.68pf.
- Write down Thevenin equivalent of the "Norton current source" and Z_1.
- Note in a large frequency range (0.1GHz to 10GHz), $|Z_1 + Z_2| \gg |Z_3|$ and therefore Z_3 can be approximated by zero.

- $Z_3 \approx 0$ readily gives circuit of Fig. 4.6 (b) with: $C_P = 0.14\text{pf}+0.38\text{pf}+44\text{ff}+6.3\text{ff}$ and $R_P = R_B + 25$.
- We add $R_1 = 50\Omega$ to R_P for reducing the error of above approximation at DC. So $R_P = R_B + 25 + 50$.
- We note $Z_3 \approx 0$ works for R_B up to about 2KΩ.

This approximate version is shown in Fig. 4.6 (b). The message is that our SNSPD is a parallel RLC circuit rather than a Parallel RL circuit, and thus it is susceptible to unwanted oscillatory behaviors. To experimentally verify the presence of such oscillations, we used the setup of Fig. 4.2 (b) with $R_B = 5\text{K}\Omega$ to capture output signals. The result is shown in Fig. 4.10 with the same signal labels previously defined in Fig. 4.2 (b). A clear damped oscillation on the difference signal, V_d, can be observed. Shown on the same figure is the step response of the simplified model of Fig. 4.6 (b) with $R_P = 5.075\text{K}\Omega$ (An arbitrary step amplitude and delay was used). These observations prove the existence of the oscillations and also satisfactory description of it by our modeling approach.

4.4.3 Maximum speed in Free-running Mode

A crucial step in demonstration of the advantages of GM-SNSPDs is comparing GM maximum count rate with that of FM operation. As the model of Fig. 4.2 (a) suggests, the maximum FM count rate should be proportional to the load resistance seen by the SNSPD, i.e. R_L. Therefore, we experimentally measured the maximum allowable R_L while maintaining the quantum efficiency at its maximum by adapting the same method reported in [9].

For different R_L values, starting from a high bias current that results in a stable latched state, we measured the current at which the nanowire returns to superconducting state while sweeping the bias voltage downwards. The resulting IV curves are shown in Fig. 4.11. We observe the peak of the currents, i.e. the maximum currents that the SNSPD can be biased in, start to decrease for R_L greater than about 150Ω. This with $L_K = 490\text{nH}$ (see Fig. 4.6) (a) gives an electrical time constant $\tau_e = 3.3\text{ns}$. This is approximately consistent

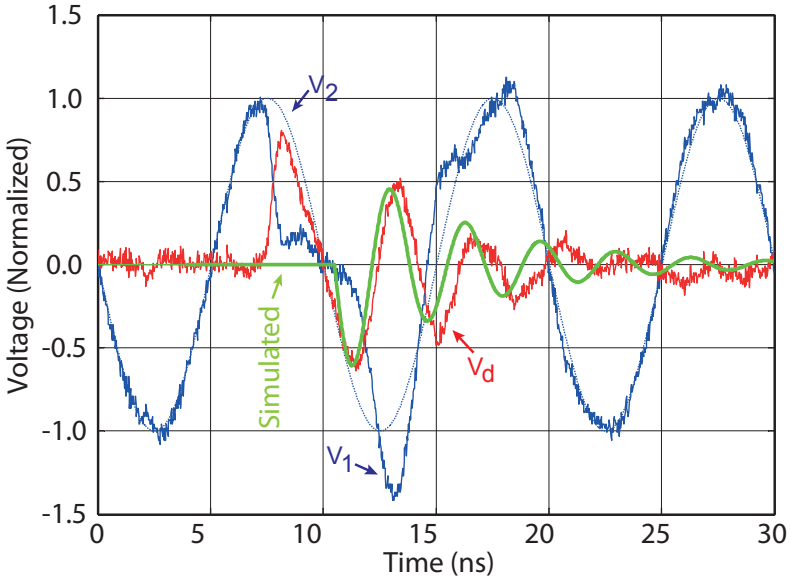

Figure 4.10: A typical set of waveforms for the circuit of Fig. 4.2 (b) with $R_B = 5\text{K}\Omega$. V_1 is coming from the SNSPD, V_2 is the reference sinusoidal, $V_d = V_2 - V_1$ and V_s is the simulated step response of the approximate model in Fig. 4.6 (b).

with the results reported in [9] and [10]. Note, we used $R_L = 100\Omega$ in the result of Fig. 4.2 (a) to further avoid latching at higher bias currents.

4.4.4 Selecting R_B and Gating Frequency

We had two unknowns for the operation of our GM-SNSPD, biasing resistor R_B and gating frequency. For determining the maximum frequency in which our SNSPD chip can operate, we did the same electro-thermal simulations as the previous section, but with $R_P = R_B + 25 + 50$ set to different values. The peak of alternating biasing current was set to 95% of the critical current and we simulate for the peak of current in the first gate following a photo-detection or dark count event. The result is shown in Fig. 4.12.

As can be seen, for a specific R_P the simulated current peak returns to its original value for a range of lower frequencies and also for a single higher frequency, f_H. Initial increase

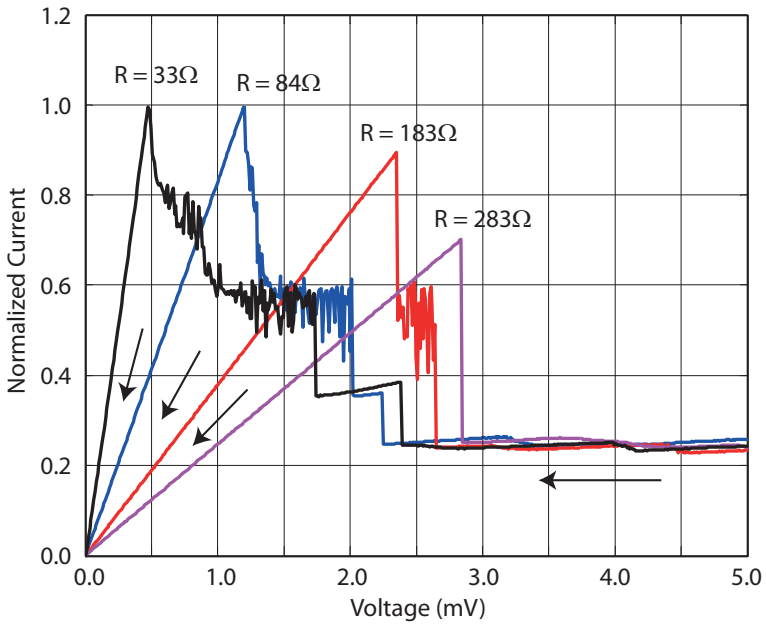

Figure 4.11: Backward Current-Voltage curves of our FM-SNSPD with different R_L values at 4.2K. The R_L values were determined from the slope of IV curve where the nanowires are superconducting.

of R_P from small values, increases f_H but further increase beyond about 750Ω degrades f_H from about 600MHz to lower values. This is how we set $R_B = 650\Omega$ for our 625MHz GM-SNSPD. Indeed, the simulation of the other peaks shown in Fig. 4.6 (c) suggests at this particular gating frequency all the currents would be about their original value during the gates succeeding a detection gate.

4.4.5 Adjusting the high frequency current

One of the difficulties of operation in gated mode is accurately applying a high frequency biasing current with a DC offset to a device operating at cryogenic temperature. Using a VNA, we characterized the components of our electrical setup including biasing coaxial cable and all individual electronic components used. The resulting information was con-

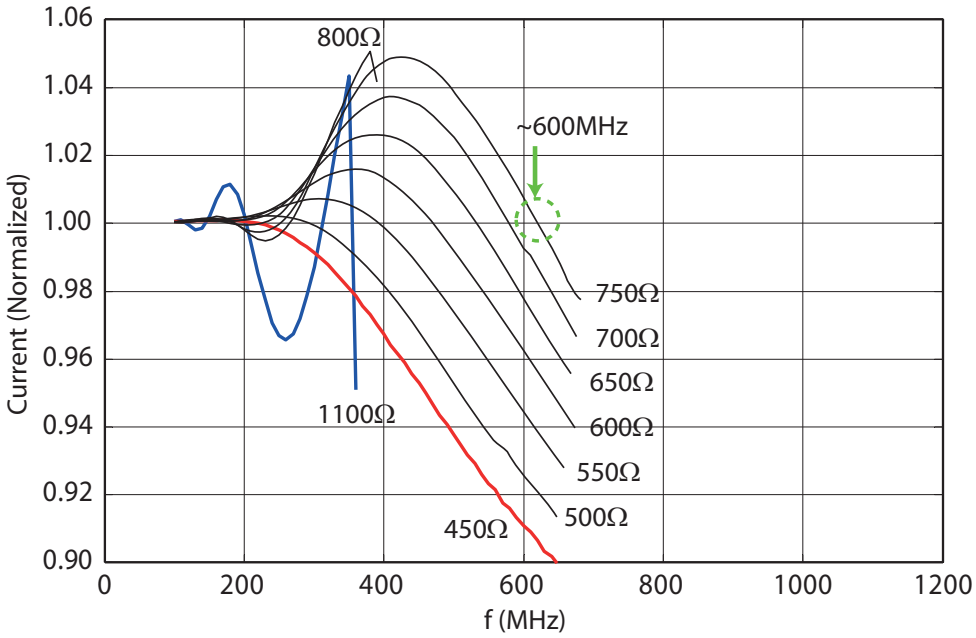

Figure 4.12: The normalized peak of the alternating bais current of our GM-SNSPD during the first gate after a detection event for different parallel resistor values, R_P.

verted to suitable electrical models be using Agilent ADS. This together with our previous SNSPD model shown in Fig. 4.6 (a), were put together to result in a circuit model that is shown in Fig. 4.13 (a).

We simulated for frequency dependence of Transconductance between the input voltage generated by the signal source and the current that flows in the Nanowires. The resulting curve is shown in Fig. 4.13 (b). This was used to adjust the minima and maxima of the biasing current throughout the experiments. It is better to set the minima of current to zero to ensure the Nanowire always returns to superconducting state following by a latching. We chose a slightly negative value (-2μA) for the minima to allow more room for the effect of noises and also errors in determining Transconductance.

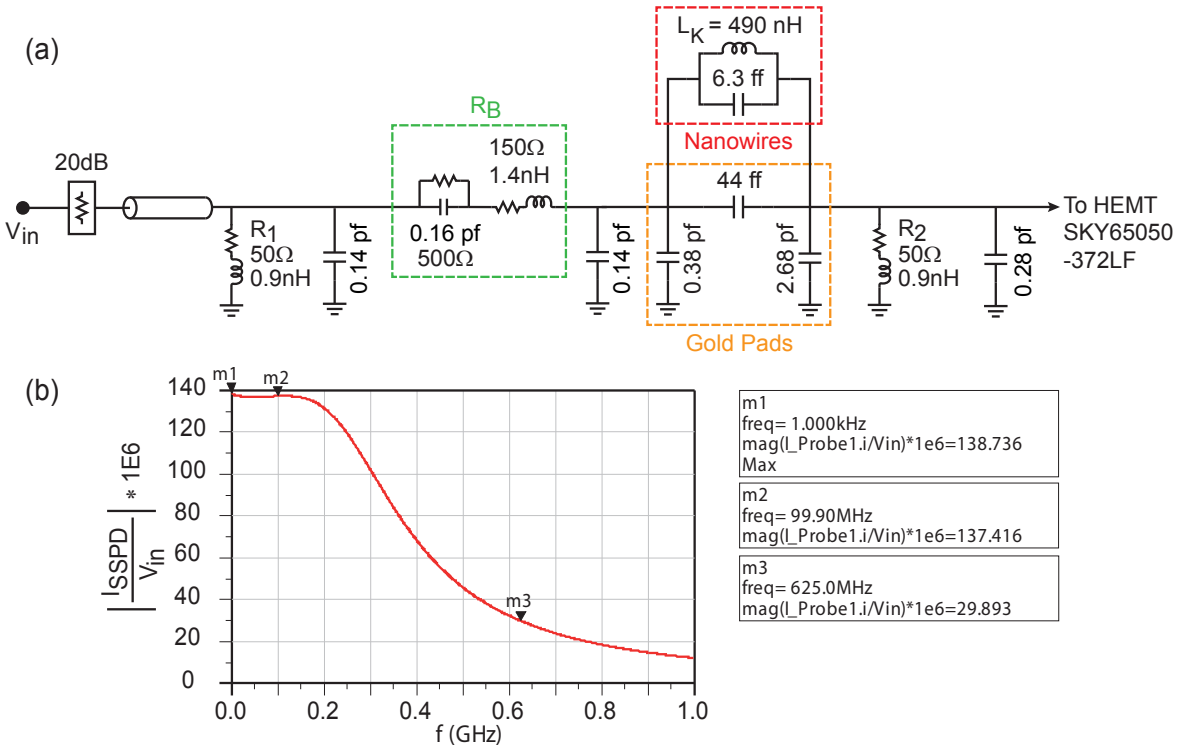

Figure 4.13: (a) Electrical circuit model for our GM-SNSPD setup. (b) Simulated transconductance between the current in the SNSPD and the input voltage, V_{in}. This was used to calculate the voltage needed to apply at room temperature V_{in} to make a specific current in the SNSPD held at a cryogenic temperature.

4.5 Conclusions

To conclude, SNSPDs can be operated in gated mode at the same quantum efficiency that they have in free-running mode, but with an enhanced maximum count rate and reduced dark counts. Using a differencing read out technique, we implemented a gated setup and characterized different features of it. We have shown how irrespective of the value of the kinetic inductance, the maximum gating frequency can be pushed to GHz range where a purely thermal limitation doesn't let faster operation. The work will add a degree of freedom for designing high speed SNSPDs for applications like quantum key distribution.

Chapter 5

Conclusions and Outlook

I have started from a general introduction to single photon detectors and a more in depth introduction about superconducting nanowire single photon detectors. Taking a semi-empirical approach a model for SNSPDs was developed, different features of it was investigated and finally it was tested with experiments in chapter 2. I have derived the quantum optical version of this model for a special case in chapter 3, and showed how the from of its POVM guided us to generalize the standard model for a SPD's POVM to a nonlinear model. I presented this nonlinear model, worked out different related problems and tested it by comparing it with detector tomography. The focus was then turned from modeling the present devices to developing new detectors. I introduced the concept of gated SNSPDs as an approach to speed up the detector in chapter 4. A sample was implemented and different features of it was explored both experimentally and theoretically. A list of my publications during the PhD years is:

- **Gated Mode Superconducting Nanowire Single Photon Detectors**

  M. K. Akhlaghi and A. H. Majedi

  arXiv: quant-ph: 1111.0588 (will appear in Optics Express)

- **Nonlinearity in Single Photon Detection: Modeling and Quantum Tomography**

M. K. Akhlaghi, A. H. Majedi and J. S. Lundeen

Optics Express, Vol. 19, Issue 22, pp. 21305-21312 (2011)

- **Controlling Superconducting Nanowire Single-Photon Detector Using Tailored Bright Illumination**

  L. Lydersen, M. K. Akhlaghi, A. H. Majedi, J. Skaar and V. Makarov

  New J. Phys. 13, 113042 (2011)

- **Semiempirical Modeling of Dark Count Rate and Quantum Efficiency of Superconducting Nanowire Single-Photon Detectors**

  M. K. Akhlaghi and A. H. Majedi

  IEEE Transaction on Applied Superconductivity, Vol. 19, Issue 3, pp. 361-366 (2009)

- **Optoelectronic Characterization of a Superconducting Quantum Detector**

  M. K. Akhlaghi and A. Hamed Majedi

  Proceeding of the 21st Annual Meeting of the IEEE LEOS, pp. 234-5 (2008)

- **Optoelectronic Characterization of a Fiber-Coupled NbN Superconducting Nanowire Single Photon Detector**

  Z. Yan, M. K. Akhlaghi, JL. Orgiazzi and A. H. Majedi

  Journal of Modern Optics, Vol. 56, Issue. 2-3, pp. 380-384 (2008)

While all of the results and discussions have their own importance, I believe there are two high impact results. Firstly, the nonlinear model for SPD's POVM is an important result because it can play the same general role of the standard model whenever needed. Published recently, the work has started showing its impact on diverse fields (e.g. see [93] on security proof of quantum key distribution, and [94] on development of nano-SPDs). Provided the existence of a trend for making SPDs from nano-structures, some of the future SPDs seem to be good candidates for observing nonlinear effects. The nonlinear model can serve as a tool for calibration purposes, as a gauge to compare the experimental results with, as a method for finding the POVM of SPDs in presence of nonlinearities, and

etc. For the nonlinear effects in SNSPDs, the life time of the nonlinear process, its relation with operation and excitation conditions and incorporation of the coherent effects into our nonlinear SPDs model are among the open questions. The results will pave the way of these effects for applications like photon number detection and correlation measurements.

Secondly, I believe the concept of gated SNSPDs is of particular importance. The SNSPDs have been intensively researched over the past decade, during which time variety of SNSPD designs have been developed. Throughout, SNSPDs have been *Mono-stable* systems: photon detection drives the system out of its equilibrium (signaling a detection event), and then the system returns to its only stable state by itself. However, for the first time, our gated SNSPD introduces the application of a *Bistable* superconducting nanowire system as a SPD. Such system integrates a memory effect (Bistability) with all good figures of present SNSPDs. A detector that exploits this phenomenon would not only detect the photons, but also would save the detection result and thus there would be lots of flexibility in detector design and readout.

I have used the Bistability to implement a gated SNSPD that operates much faster at a lower noise, significant advantages for many applications in different fields. I expect the gated operation will become a dual operation mode for all types of SNSPDs, be single element, multi-element, photon number resolving, or integrated with optical structures. However, the present gating scheme is a synchronous one, which is advantages for some applications because it eliminates the background photons that hit the detector out of the gates. But, it is also possible to design asynchronously gated SNSPDs as well. The result would be a free-running SPD that have the advantages of present SNSPDs but operates much faster.

In addition, the unique features of single photon triggered Bistability in superconducting nanowires allow a more flexible design, and therefore emergence of a new category of SPDs that work based on the same principle is expected. For instance, it can be exploited to make photon-number-resolving and imaging SPDs: many independent pixels detect the photons and store the results, the electronic probes then read the pixels and reset the device (This is reminiscent of the working of widely used CCD imaging sensors, however instead of charge, a thermal effect stores the information). High quantum efficiency, small dark counts, high timing accuracy and fast operation are expected because of the photon

detection features of SNSPDs. Also the large number of small pixels while keeping the readout scheme simple is expected because of the memory effect. We have started the fabrication of pixels in the form of short superconducting nanowires and have good initial characterization results. However, lots of fabrication and readout challenges have to be addressed before emergence of the first new SPDs.

References

[1] S. Miki, M. Fujiwara, M. Sasaki, and Z. Wang. Development of SNSPD system with Gifford-McMahon cryocooler. *IEEE Transactions on Applied Superconductivity*, 19(3):332–335, 2009.

[2] G. N. Gol'tsman, O. Okunev, G. Chulkova, A. Lipatov, A. Semenov, K. Smirnov, B. Voronov, A. Dzardanov, C. Williams, and R. Sobolewski. Picosecond superconducting single-photon optical detector. *Applied Physics Letters*, 79(6):705–707, 2001.

[3] K. M. Rosfjord, J. K. W. Yang, E. A. Dauler, A. J. Kerman, V. Anant, B. M. Voronov, G. N. Gol'tsman, and K. K. Berggren. Nanowire single-photon detector with an integrated optical cavity and anti-reflection coating. *Optics Express*, 14(2):527–534, 2006.

[4] G. N. Gol'tsman, A. Korneev, I. Rubtsova, I. Milostnaya, G. Chulkova, O. Minaeva, K. Smirnov, B. Voronov, W. Slysz, A. Pearlman, A. Verevkin, and R. Sobolewski. Ultrafast superconducting single-photon detectors for near-infrared-wavelength quantum communications. *Physica Status Solidi C: Conferences*, 2(5):1480–1488, 2005.

[5] E. A. Dauler, B. S. Robinson, A. J. Kerman, J. K. W. Yang, K. M. Rosfjord, V. Anant, B. Voronov, G. Gol'tsman, and K. K. Berggren. Multi-element superconducting nanowire single-photon detector. *IEEE Transactions on Applied Superconductivity*, 17(2):279–284, 2007.

[6] A. D. Semenov, G. N. Gol'tsman, and A. A. Korneev. Quantum detection by current carrying superconducting film. *Physica C: Superconductivity and its Applications*, 351(4):349–356, 2001.

[7] E. A. Dauler, A. J. Kerman, B. S. Robinson, J. K. W. Yang, B. Voronov, G. Goltsman, S. A. Hamilton, and K. K. Berggren. Photon-number-resolution with sub-30-ps timing using multi-element superconducting nanowire single photon detectors. *Journal of Modern Optics*, 56(2-3):364–373, 2009.

[8] A. Divochiy, F. Marsili, D. Bitauld, A. Gaggero, R. Leoni, F. Mattioli, A. Korneev, V. Seleznev, N. Kaurova, O. Minaeva, G. Gol'Tsman, K. G. Lagoudakis, M. Benkhaoul, F. Lvy, and A. Fiore. Superconducting nanowire photon-number-resolving detector at telecommunication wavelengths. *Nature Photonics*, 2(6):377, 2008.

[9] Andrew J. Kerman, Joel K. W. Yang, Richard J. Molnar, Eric A. Dauler, and Karl K. Berggren. Electrothermal feedback in superconducting nanowire single-photon detectors. *Phys. Rev. B*, 79(10), Mar 2009.

[10] A. J. Annunziata, O. Quaranta, D. F. Santavicca, A. Casaburi, L. Frunzio, M. Ejrnaes, M. J. Rooks, R. Cristiano, S. Pagano, A. Frydman, and D. E. Prober. Reset dynamics and latching in Niobium superconducting nanowire single-photon detectors. *Journal of Applied Physics*, 108(8), 2010.

[11] M. Varnava, D. E. Browne, and T. Rudolph. How good must single photon sources and detectors be for efficient linear optical quantum computation? *Physical Review Letters*, 100(6), 2008.

[12] K. K. Berggren and A. J. Kerman. Nanowires detect individual infrared photons. *Laser Focus World*, 42(9):87–89, 2006.

[13] P. LeCoupanec, W. K. Lo, and K. R. Wilsher. An ultra-low dark-count and jitter, superconducting, single-photon detector for emission timing analysis of integrated circuits. *Microelectronics Reliability*, 43(9-11):1621–1626, 2003.

[14] J. Zhang, N. Boiadjieva, G. Chulkova, H. Deslandes, G. N. Gol'tsman, A. Korneev, P. Kouminov, M. Leibowitz, W. Lo, R. Malinsky, O. Okunev, A. Pearlman, W. Slysz, K. Smirnov, C. Tsao, A. Verevkin, B. Voronov, K. Wilsher, and R. Sobolewski. Non-invasive CMOS circuit testing with NbN superconducting single-photon detectors. *Electronics Letters*, 39(14):1086–1088, 2003.

[15] M. J. Stevens, R. H. Hadfield, R. E. Schwall, S. W. Nam, and R. P. Mirin. Quantum dot single photon sources studied with superconducting single photon detectors. *IEEE Journal on Selected Topics in Quantum Electronics*, 12(6):1255–1267, 2006.

[16] A. Pauchard, G. Ribordy, A. Rochas, L. Widmer, R. Thew, and W. Becker. Single-photon detectors take quantum leaps. *Laser Focus World*, 42(5):79–84, 2006.

[17] Hamamatsu corporation web site. *http://sales.hamamatsu.com/en/products/electron-tube-division/detectors/photomultiplier-modules.php*.

[18] Scientific camera solutions catalog. *http://www.andor.com*.

[19] F. Zappa, A. Giudice, M. Ghioni, and S. Cova. Fully-integrated active-quenching circuit for single-photon detection. *ESSCIRC*, pages 355–8, 2002.

[20] ID Quantique corporation web site. *http://www.idquantique.com/products/id100-20.htm*.

[21] J. A. Seamons and M. S. Carroll. High bit rate Germanium single photon detectors for 1310 nm. *Proceedings of SPIE - The International Society for Optical Engineering*, 6976, 2008.

[22] M. S. Carroll, K. Childs, R. Jarecki, T. Bauer, and K. Saiz. Ge-Si separate absorption and multiplication avalanche photodiode for Geiger mode single photon detection. *Applied Physics Letters*, 93(18), 2008.

[23] Sun W. Hu C. Holmes A. Campbell J.C. Kang Y. Liu H.-D. Lu, Z. Ge on Si and InP/InGaAs single photon avalanche diodes. *Proceedings of SPIE - The International Society for Optical Engineering*, 8155(81551E), 2011.

[24] P. Yuan, J. Boisvert, R. Sudharsanan, T. Isshiki, P. McDonald, M. Salisbury, M. Liu, and J. C. Campbell. High efficiency 1.55μm Geiger-mode single photon counting avalanche photodiodes operating near 0°C. *Proceedings of SPIE - The International Society for Optical Engineering*, 6900, 2008.

[25] W. Zhengjun, W. Jindong, L. Kaizhen, Z. Peng, L. Changjun, G. Jianping, and L. Songhao. The study of single photon detector for quantum key distribution. *Proceedings of SPIE - The International Society for Optical Engineering*, 6827, 2008.

[26] D. C. Chapman, C. J. Vineis, D. C. Oakley, A. Napoleone, G. M. Smith, E. K. Duerr, K. E. Jensen, J. P. Donnelly, K. A. McIntosh, and S. Verghese. Growth and characterization of GaInAsP/InP-based Geiger-mode avalanche photodiodes. *Journal of Crystal Growth*, 310(7-9):2365–2369, 2008.

[27] N. Faramarzpour, M. J. Deen, S. Shirani, and Q. Fang. Fully integrated single photon avalanche diode detector in standard CMOS 0.18μm technology. *IEEE Transactions on Electron Devices*, 55(3):760–767, 2008.

[28] S. Verghese, K. A. McIntosh, Z. L. Liau, C. Sataline, J. D. Shelton, J. P. Donnelly, J. E. Funk, R. D. Younger, L. J. Mahoney, G. M. Smith, J. M. Mahan, D. C. Chapman, D. C. Oakley, and M. Brattain. Arrays of 1287×32 InP-based Geiger-mode avalanche photodiodes. *Proceedings of SPIE - The International Society for Optical Engineering*, 7320(73200M), 2009.

[29] L. Aina, A. Fathimulla, H. Hier, M. Lecates, R. Dwarkin, D. Johnson, S. Babu, and J. Foshee. Linear-mode single photon counting APD arrays with subnanosecond, afterpulse-free performance for ladar, spectroscopy and QKD applications. *Proceedings of SPIE - The International Society for Optical Engineering*, 6572, 2007.

[30] A. S. Huntington, M. A. Compton, and G. M. Williams. Linear-mode single-photon APD detectors. *Proceedings of SPIE - The International Society for Optical Engineering*, 6771, 2007.

[31] N. Namekata and S. Inoue. Afterpulsing-free 80MHz single-photon detection at 1550nm using an InGaAs/InP avalanche photodiode operated with sinusoidal gating. *Conference on Lasers and Electro-Optics Europe - Technical Digest*, 2007.

[32] A. R. Dixon, J. F. Dynes, Z. L. Yuan, A. W. Sharpe, A. J. Bennett, and A. J. Shields. Ultrashort dead time of photon-counting InGaAs avalanche photodiodes. *Applied Physics Letters*, 94(23), 2009.

[33] Z. L. Yuan, B. E. Kardynal, A. W. Sharpe, and A. J. Shields. High speed single photon detection in the near infrared. *Applied Physics Letters*, 91(4), 2007.

[34] Z. L. Yuan, A. W. Sharpe, J. F. Dynes, A. R. Dixon, and A. J. Shields. Multi-gigahertz operation of photon counting InGaAs avalanche photodiodes. *Applied Physics Letters*, 96(7), 2010.

[35] A. J. Miller, S. W. Nam, J. M. Martinis, and A. V. Sergienko. Demonstration of a low-noise near-infrared photon counter with multiphoton discrimination. *Applied Physics Letters*, 83(4):791–793, 2003.

[36] D. Rosenberg, A. E. Lita, A. J. Miller, S. Nam, and R. E. Schwall. Performance of photon-number resolving transition-edge sensors with integrated 1550nm resonant cavities. *IEEE Transactions on Applied Superconductivity*, 15(2 PART I):575–578, 2005.

[37] D. Rosenberg, S. W. Nam, P. A. Hiskett, C. G. Peterson, R. J. Hughes, J. E. Nordholt, A. E. Lita, and A. J. Miller. Quantum key distribution at telecom wavelengths with noise-free detectors. *Applied Physics Letters*, 88(2):1–3, 2006.

[38] D. Fukuda, R. M. T. Damayanthi, A. Yoshizawa, N. Zen, H. Takahashi, K. Amemiya, and M. Ohkubo. Titanium based transition edge microcalorimeters for optical photon measurements. *IEEE Transactions on Applied Superconductivity*, 17(2):259–262, 2007.

[39] D. Fukuda. Fast response and high quantum efficiency Ti-based TES optical detector and its application to quantum information. volume 1185, pages 771–772, 2009.

[40] A. Peacock, P. Verhoeve, N. Rando, A. Van Dordrecht, B. G. Taylor, C. Erd, M. A. C. Perryman, R. Venn, J. Howlett, D. J. Goldie, J. Lumley, and M. Wallis. Single optical photon detection with a superconducting tunnel junction. *Nature*, 381(6578):135–137, 1996.

[41] D. D. E. Martin, P. Verhoeve, A. Peacock, A. van Dordrecht, J. Verveer, and R. Hijmering. A 12×10 pixels superconducting tunnel junction array based spectrophotometer for optical astronomy. *Nuclear Instruments and Methods in Physics Research, Section A (Accelerators, Spectrometers, Detectors and Associated Equipment)*, 520(1-3):512–5, 2004.

[42] I. Milostnaya, A. Korneev, O. Minaeva, I. Rubtsova, S. Slepneva, V. Seleznev, G. Chulkova, O. Okunev, K. Smirnov, B. Voronov, G. Gol'tsman, W. Slysz, J. Kitaygorsky, A. Cross, A. Pearlman, and R. Sobolewski. Superconducting nanostructured detectors capable of single photon counting of mid-infrared optical radiation. *Proceedings of SPIE - The International Society for Optical Engineering*, 5957:1–9, 2005.

[43] M. Bell, A. Antipov, B. Karasik, A. Sergeev, V. Mitin, and A. Verevkin. Photon number-resolved detection with sequentially connected nanowires. *IEEE Transactions on Applied Superconductivity*, 17(2):289–292, 2007.

[44] A. D. Semenov, P. Haas, B. Gnther, H. W Hbers, K. Il'in, and M. Siegel. Energy resolution of a superconducting nanowire single-photon detector. *Journal of Low Temperature Physics*, 151(1-2 PART 1):564–569, 2008.

[45] E. Reiger, S. Dorenbos, V. Zwiller, A. Korneev, G. Chulkova, I. Milostnaya, O. Minaeva, G. Gol'tsman, J. Kitaygorsky, D. Pan, W. Slysz, A. Jukna, and R. Sobolewski. Spectroscopy with nanostructured superconducting single photon detectors. *IEEE Journal on Selected Topics in Quantum Electronics*, 13(4):934–942, 2007.

[46] R. H. Hadfield. Single photon detectors for optical quantum information applications. *Nature Photonics*, 3(12):696–705, 2009.

[47] M. D. Eisaman, J. Fan, A. Migdall, and S. V. Polyakov. Invited review article: Single-photon sources and detectors. *Review of Scientific Instruments*, 82(7), 2011.

[48] Z. Yan, A. H. Majedi, and S. Safavi-Naeini. Physical modeling of hot-electron superconducting single-photon detectors. *IEEE Transactions on Applied Superconductivity*, 17(3):3789–3794, 2007.

[49] V. Anant, A. J. Kerman, E. A. Dauler, J. K. W. Yang, K. M. Rosfjord, and K. K. Berggren. Optical properties of superconducting nanowire single-photon detectors. *Optics Express*, 16(14):10750–10761, 2008.

[50] X. Hu, E. A. Dauler, R. J. Molnar, and K. K. Berggren. Superconducting nanowire single-photon detectors integrated with optical nano-antennae. *Optics Express*, 19(1):17–31, 2011.

[51] A. Gaggero, J. P. Sprengers, D. Sahin, S. J. Nejad, D. Bitauld, J.-Lermer M. Beetz, M. Kamp, S. Hfling, F. Mattioli, R. Leoni, and A. Fiore. Waveguide single-photon detectors for integrated quantum photonics. *2011 Conference on Lasers and Electro-Optics: Laser Science to Photonic Applications, CLEO 2011*, (5951266), 2011.

[52] Constancias C. Feautrier P. Maingault L. Morand A. Villgier J.-C. Cavalier, P. SWIFTS waveguide micro-spectrometer integrated on top of a 1D-NbN SNSPD array. *IEEE Transactions on Applied Superconductivity*, 21(3 PART 1):327–331, 2011.

[53] A. D. Semenov, G. N. Gol'tsman, and R. Sobolewski. Hot-electron effect in superconductors and its applications for radiation sensors. *Superconductor Science and Technology*, 15(4):R1–R16, 2002.

[54] G. Gol'Tsman, O. Okunev, G. Chulkova, A. Lipatov, A. Dzardanov, K. Smirnov, A. Semenov, B. Voronov, C. Williams, and R. Sobolewski. Fabrication and properties of an ultrafast NbN hot-electron single-photon detector. *IEEE Transactions on Applied Superconductivity*, 11(1 I):574–577, 2001.

[55] M. K. Akhlaghi and A. H. Majedi. Optoelectronic characterization of a superconducting quantum detector. *Conference Proceedings - Lasers and Electro-Optics Society Annual Meeting-LEOS,*, pages 234–235, 2008.

[56] G. Gol'tsman, O. Minaeva, A. Korneev, M. Tarkhov, I. Rubtsova, A. Divochiy, I. Milostnaya, G. Chulkova, N. Kaurova, B. Voronov, D. Pan, J. Kitaygorsky, A. Cross, A. Pearlman, I. Komissarov, W. Slysz, M. Wegrzecki, P. Grabiec, and R. Sobolewski. Middle-infrared to visible-light ultrafast superconducting single-photon detectors. *IEEE Transactions on Applied Superconductivity*, 17(2):246–251, 2007.

[57] A. Semenov, A. Engel, H. W Hbers, K. Il'in, and M. Siegel. Spectral response of an infrared superconducting quantum detector. *Proceedings of SPIE - The International Society for Optical Engineering*, 5459:237–245, 2004.

[58] R. Sobolewski, A. Verevkin, G. N. Gol'tsman, A. Lipatov, and K. Wilsher. Ultrafast superconducting single-photon optical detectors and their applications. *IEEE Transactions on Applied Superconductivity*, 13(2 I):1151–1157, 2003.

[59] G. N. Gol'tsman, K. Smirnov, P. Kouminov, B. Voronov, N. Kaurova, V. Drakinsky, J. Zhang, A. Verevkin, and R. Sobolewski. Fabrication of nanostructured superconducting single-photon detectors. *IEEE Transactions on Applied Superconductivity*, 13(2 I):192–195, 2003.

[60] G. Goltsman, A. Korneev, O. Minaeva, I. Rubtsova, G. Chulkova, I. Milostnaya, K. Smirnov, B. Voronov, A. Lipatov, A. Pearlman, A. Cross, W. Slysz, A. Verevkin, and R. Sobolewski. Advanced nanostructured optical NbN single-photon detector operated at 2.0K. *Progress in Biomedical Optics and Imaging - Proceedings of SPIE*, 5732:520–529, 2005.

[61] G. Chulkova, I. Milostnaya, A. Korneev, O. Minaeva, I. Rubtsova, B. Voronov, O. Okunev, K. Smirnov, G. Gol'tsman, J. Kitaygorsky, A. Cross, A. Pearlman, R. Sobolewski, and W. Slysz. Superconducting nanostructures for counting of single photons in the infrared range. *Proceedings of CAOL 2005: 2nd International Conference on Advanced Optoelectronics and Lasers*, 2:100–103, 2005.

[62] P. Haas, A. Semenov, H. W Hbers, J. Beyer, A. Kirste, T. Schurig, K. Il'in, M. Siegel, A. Engel, and A. Smirnov. Spectral sensitivity and spectral resolution of superconducting single-photon detectors. *IEEE Transactions on Applied Superconductivity*, 17(2):298–301, 2007.

[63] A. Korneev, P. Kouminov, V. Matvienko, G. Chulkova, K. Smirnov, B. Voronov, G. N. Gol'tsman, M. Currie, W. Lo, K. Wilsher, J. Zhang, W. Sllysz, A. Pearlman, A. Verevkin, and R. Sobolewski. Sensitivity and gigahertz counting performance of NbN superconducting single-photon detectors. *Applied Physics Letters*, 84(26):5338–5340, 2004.

[64] A. J. Kerman, E. A. Dauler, W. E. Keicher, J. K. W. Yang, K. K. Berggren, G. Gol'tsman, and B. Voronov. Kinetic-inductance-limited reset time of superconducting nanowire photon counters. *Applied Physics Letters*, 88(11), 2006.

[65] J. K. W. Yang, A. J. Kerman, E. A. Dauler, V. Anant, K. M. Rosfjord, and K. K. Berggren. Modeling the electrical and thermal response of superconducting nanowire single-photon detectors. *IEEE Transactions on Applied Superconductivity*, 17(2):581–585, 2007.

[66] Z. Yan, M. K. Akhlaghi, J. L. Orgiazzi, and A. Hamed Majedi. Optoelectronic characterization of a fiber-coupled NbN superconducting nanowire single photon detector. *Journal of Modern Optics*, 56(2-3):380–384, 2009.

[67] M. K. Akhlaghi and A. H. Majedi. Semiempirical modeling of dark count rate and quantum efficiency of superconducting nanowire single-photon detectors. *IEEE Transactions on Applied Superconductivity*, 19(3):361–366, 2009.

[68] J. Zhang, W. Slysz, A. Pearlman, A. Verevkin, R. Sobolewski, O. Okunev, G. Chulkova, and G. N. Gol'tsman. Time delay of resistive-state formation in superconducting stripes excited by single optical photons. *Physical Review B - Condensed Matter and Materials Physics*, 67(13):1325081–1325084, 2003.

[69] M. K. Akhlaghi, A. Hamed Majedi, and J. S. Lundeen. Nonlinearity in single photon detection: Modeling and quantum tomography. (arXiv:1108.3815), 2011.

[70] Mohsen K. Akhlaghi, A. Hamed Majedi, and Jeff S. Lundeen. Nonlinearity in single photon detection: modeling and quantum tomography. *Opt. Express*, 19(22):21305–21312, Oct 2011.

[71] M. O. Scully, W. Martienssen, and S. Prasad. A quantum description of the beam splitter. *Optics Communications*, 62(3):139–145, 1987.

[72] K. J. Resch, J. S. Lundeen, and A. M. Steinberg. Experimental observation of non-classical effects on single-photon detection rates. *Phys. Rev. A*, 63(2):020102, 2001.

[73] S. Boyd and L. Vandenberghe. *Convex Optimization*. Cambridge University Press, 2004.

[74] J. S. Lundeen, A. Feito, H. Coldenstrodt-Ronge, K. L. Pregnell, C. Silberhorn, T. C. Ralph, J. Eisert, M. B. Plenio, and I. A. Walmsley. Tomography of quantum detectors. *Nature Physics*, 5(1):27–30, 2009.

[75] H. B. Coldenstrodt-Ronge, J. S. Lundeen, K. L. Pregnell, A. Feito, B. J. Smith, W. Mauerer, C. Silberhorn, J. Eisert, M. B. Plenio, and I. A. Walmsley. A proposed testbed for detector tomography. *Journal of Modern Optics*, 56(2-3):432–441, 2009.

[76] A. Feito, J. S. Lundeen, H. Coldenstrodt-Ronge, J. Eisert, M. B. Plenio, and I. A. Walmsley. Measuring measurement: Theory and practice. *New Journal of Physics*, 11, 2009.

[77] J. L F. X Orgiazzi and A. H. Majedi. Robust packaging technique and characterization of fiber-pigtailed superconducting NbN nano wire single photon detectors. *IEEE Transactions on Applied Superconductivity*, 19(3):341–345, 2009.

[78] M. J. Stevens, R. H. Hadfield, R. E. Schwall, S. W. Nam, R. P. Mirin, and J. A. Gupta. Fast lifetime measurements of infrared emitters using a low-jitter superconducting single-photon detector. *Applied Physics Letters*, 89(3), 2006.

[79] H. Takesue, S. W. Nam, Q. Zhang, R. H. Hadfield, T. Honjo, K. Tamaki, and Y. Yamamoto. Quantum key distribution over a 40-dB channel loss using superconducting single-photon detectors. *Nature Photonics*, 1(6):343–348, 2007.

[80] R. H. Hadfield. Single photon detectors for optical quantum information applications. *Nature Photonics*, 3(12):696–705, 2009.

[81] Mohsen K. Akhlaghi and A. Hamed Majedi. Gated mode superconducting nanowire single photon detectors. (*arXiv: quant-ph: 1111.0588*), 2011.

[82] H. Shibata, H. Takesue, T. Honjo, T. Akazaki, and Y. Tokura. Single-photon detection using magnesium diboride superconducting nanowires. *Applied Physics Letters*, 97(21), 2010.

[83] A. Korneev, O. Minaeva, A. Divochiy, A. Antipov, N. Kaurova, V. Seleznev, B. Voronov, G. Gol'tsman, D. Pan, J. Kitaygorsky, W. Slysz, and R. Sobolewski. Ultrafast and high quantum efficiency large-area superconducting single-photon detectors. *Proceedings of SPIE - The International Society for Optical Engineering*, 6583, 2007.

[84] S. Miki, M. Takeda, M. Fujiwara, M. Sasaki, A. Otomo, and Z. Wang. Superconducting NbTiN nanowire single photon detectors with low kinetic inductance. *Applied Physics Express*, 2(7), 2009.

[85] A. J. Annunziata, D. F. Santavicca, J. D. Chudow, L. Frunzio, M. J. Rooks, A. Frydman, and D. E. Prober. Niobium superconducting nanowire single-photon detectors. *IEEE Transactions on Applied Superconductivity*, 19(3):327, june 2009.

[86] M. Ejrnaes, A. Casaburi, R. Cristiano, O. Quaranta, S. Marchetti, and S. Pagano. Maximum count rate of large area superconducting single photon detectors. *Journal of Modern Optics*, 56(2-3):390–394, 2009.

[87] Y. Korneeva, I. Florya, A. Semenov, A. Korneev, and G. Goltsman. New generation of nanowire NbN superconducting single-photon detector for mid-infrared. *IEEE Transactions on Applied Superconductivity*, 21(3 PART 1):323–326, 2011.

[88] M. Tarkhov, J. Claudon, J. Ph Poizat, A. Korneev, A. Divochiy, O. Minaeva, V. Seleznev, N. Kaurova, B. Voronov, A. V. Semenov, and G. Gol'Tsman. Ultrafast reset time of superconducting single photon detectors. *Applied Physics Letters*, 92(24), 2008.

[89] Francesco Marsili, Faraz Najafi, Eric Dauler, Francesco Bellei, Xiaolong Hu, Maria Csete, Richard J. Molnar, and Karl K. Berggren. Single-photon detectors based on ultranarrow superconducting nanowires. *Nano Letters*, 11(5):2048–2053, 2011.

[90] F. Marsili, F. Najafi, C. Herder, and K. K. Berggren. Electrothermal simulation of superconducting nanowire avalanche photodetectors. *Applied Physics Letters*, 98(9), 2011.

[91] C. A. Flory and R. C. Taber. Microwave oscillators incorporating cryogenic sapphire dielectric resonators. *Proceedings of the Annual Frequency Control Symposium*, pages 763–773, 1993.

[92] V. B. Braginsky, V. S. Ilchenko, and Kh S. Bagdassarov. Experimental observation of fundamental microwave absorption in high-quality dielectric crystals. *Physics Letters A*, 120(6):300–305, 1987.

[93] Lars Lydersen, Nitin Jain, Christoffer Wittmann, ystein Mary, Johannes Skaar, Christoph Marquardt, Vadim Makarov, and Gerd Leuchs. Superlinear threshold detectors in quantum cryptography. (*arXiv: quant-ph: 1106.2119*), 2011.

[94] J. J. Renema, G. Frucci, Z. Zhou, F. Mattioli, A. Gaggero, R. Leoni, M. J. A. de Dood, A. Fiore, and M. P. van Exter. Complete experimental characterization of a superconducting multiphoton nanodetector. (*arXiv: quant-ph: 1110.5442*), 2011.